ELECTROCHEMICAL N-TYPE DOPING IN METAL OXIDES AND

ITS APPLICATION IN PHOTOVOLTAICS

by

XIAOFEI HAN

Presented to the Faculty of the Graduate School of

The University of Texas at Arlington in Partial Fulfillment

of the Requirements

for the Degree of

DOCTOR OF PHILOSOPHY

THE UNIVERSITY OF TEXAS AT ARLINGTON

May 2011

ACKNOWLEDGEMENTS

I would like to offer my great gratitude and thanks to Dr. Meng Tao for his guidance, instruction, and supporting on my research work. I am deeply grateful of his help in the completion of this dissertation and financial support of my degree achieving. I also present my acknowledgement for offering me the opportunity to work under him. I would also like to thank Prof. Michael Vasilyev, Prof. Weidong Zhou, Prof. Michael Jin, and Prof. Fuqiang Liu for agreeing to be committee members and helpful discussion on my research work. I would also like to acknowledge Eduardo Maldonado and Dennis Bueno for their efforts to help me using the facilities in the clean room.

I would also like to deeply thank all other previous and current group members including Dr. Guanghua Song, Dr. Yusuf Ali, Dr. Kunhee Han, Mr. Armit Banik, Dr. Ying Yang, Mr. Bin Zhou, Dr. Withana Siripala, Ms. Yi Li, Ms. Munteha Aydin and Dr. Feng Kang for their friendship and assistance in my research. I'd also like to thank all my friends and my relatives for their kindly encouragement and support in my life.

Most importantly, none of this would have been possible without the love and patience of my family. My wife, Huili Xu, who has always been beside me, offered her love, sacrifice and support with great patience. She helped me a lot on the discussion of my research and revision of paper work. I also want to thank my parents and my parents-in-law. With patience and understanding, they have always taken care of and believed in me.

March 10, 2011

ABSTRACT

ELECTROCHEMICAL N-TYPE DOPING IN METAL OXIDES AND

ITS APPLICATION IN PHOTOVOLTAICS

Xiaofei Han, PhD

The University of Texas at Arlington, 2011

Supervising Professor: Meng Tao

Electrodeposition has the advantages of low-cost, high-throughput and large-area processing which is particularly suitable for solar cells fabrication. Two common metal oxides prepared by electrodeposition are discussed here, ZnO and Cu_2O. ZnO is largely used in the solar cells as the window and transparent contact material. Cu_2O is potential absorption material for next generation solar cell. n-type doping of these metal oxides was revealed during electrochemical deposition. For naturally n-type ZnO, n-type doping is achieved by substituting the cation (Zn) with a group III element (Al, Ga and Y) and for naturally p-type Cu_2O, n-type doping is realized by substituting the anion (O) with a halogen (Cl). In both cases, the doping mechanism is believed to be co-precipitation of either ZnO with group III metal oxide (Al_2O_3, Ga_2O_3 and Y_2O_3) or Cu_2O with Cu halide (CuCl).

Cl doped Cu_2O films were electrodeposited on Cu coated glass substrate. Photocurrent measurement determined its n-type conductivity. The resistivity of Cl doped Cu_2O was

calculated through IV relationship and the lowest resistivity of Cl-doped n-type Cu_2O is around 7 Ω-cm which is suitable for solar cell application. Photocurrent measurement confirms the conductivity of this Cl-doped Cu_2O is n-type. XRD shows the Cl-doped Cu_2O is pure Cu_2O and SEM shows the grain of Cu_2O is small, about 100 nm. Once p-type Cu_2O is realized, a p-n homojuction Cu_2O cell with reasonable high efficiency can be achieved.

Al, Ga and Y doped ZnO deposited by electrodeposition shows high transmittance, low absorbance and low resistivity. The minimum sheet resistance is 1.5 $\Omega/\square$ with Y doped ZnO and the co-responding resistivity is 6.3×10^{-5} Ω-cm calculated by a parallel circuit model from stack sheet resistance. Different annealing conditions were used for lowest resistivity of ZnO realization. A UV-vis spectrum was used for transmittance and absorbance observation. XRD profiles show the ZnO doesn't mix with ITO after annealing and the SEM images show Y doped ZnO is hexagonal shape with sub-micro grain size. Thermal stability test shows this Y doped ZnO can still maintain low resistivity and high reflectance after 500 °C annealing in N_2 ambient. This low resistance and high transmittance ZnO can be used as either top transparent contact or back reflector in the thin film solar cell.

TABLE OF CONTENTS

LIST OF ILLUSTRATIONS

x

xi

xii

LIST OF TABLES

CHAPTER 1

INTRODUCTION

1.1 World Energy

The increasing energy consumption becomes one of the serious problems in the world due to the rapidly growth of world population. The energy consumption is expected to be twice as that reported in 2006, which was 15.8 TW [1]. World Energy is existed as chemical energy like gasoline, food, wood; electrical energy, such as electricity from grid, battery; thermal energy such as hot water, hot stream, hot air and optical energy like sunlight. Figure 1.1 shows the fuel shares of world total primary energy supply [2]. Fossil energy, the main energy source on the earth including gas, oil and coal, shares 85% of the total energy consumption, but it can only be used for limited years. Nuclear is a new type energy which is generated by fission or fusion of atoms, and constitutes 6.5% of total energy in the world. Renewable energy occupies just 13.1% of the total energy consumption. The renewable energy can be classified into these groups: hydro, combustible renewable, renewable waste and others like wind, solar and geothermal etc. In fact, all kinds of energy come from sun by converting solar energy into chemical energy or kinetic energy, and consequently converted to heat and electricity for daily application. However, the solar energy is the one that can directly convert solar into heat and electricity.

Figure 1.2 shows the four largest energy consumption areas in the world [1]. Most of the energy is used as electricity converted from chemical energy embedding in the coal and oil which occupies 40% of the total energy consumption. The second largest energy consumption area is transportation vehicles, which consume fossil fuel like gasoline and diesel as the power source. Furthermore, Industry also consumes a lot of energy, around 21%.

1
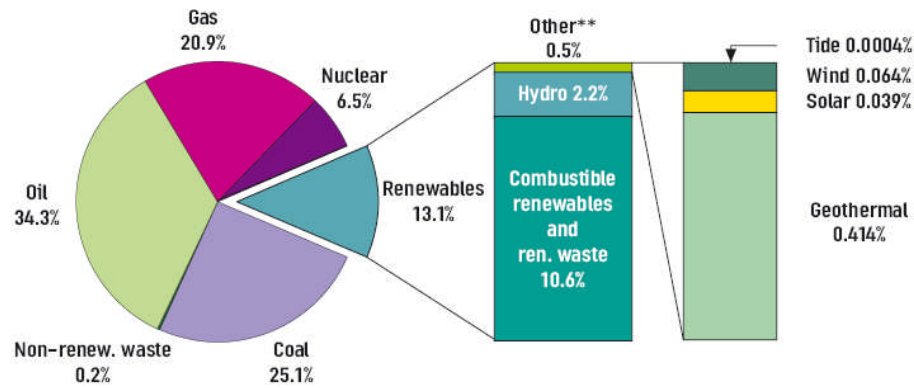
Figure 1.1. Fuel shares of world total primary energy supply
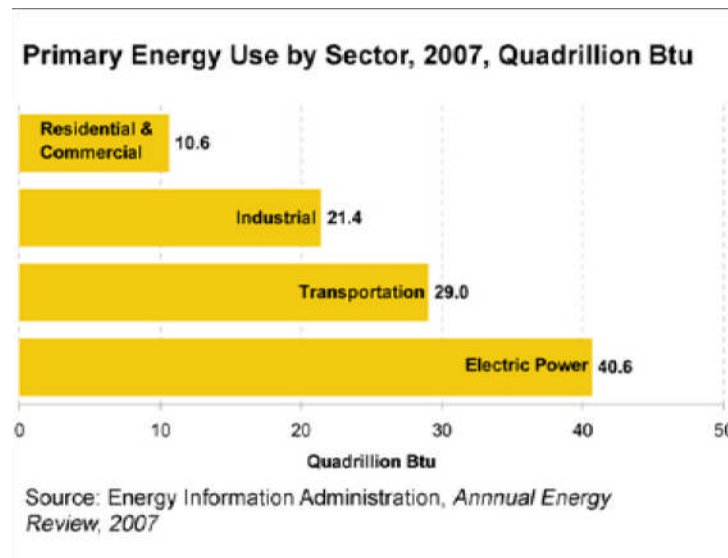
Figure 1.2. The main areas of energy consumption

The future global energy demand depends on several issues, like population growth, economy development, energy usage efficiency and carbon oxide generation of energy source. Figure 1.3 shows how these factors impact on the total energy consumption. If each person consumes the same energy in the world, the total energy consumption is determined by the number of people who is using energy [3]. Figure 1.3(a) shows the total energy consumption is increasing with the increasing of world population. Since industry consumes 21% of the total

energy, the economy growth which usually defined by GDP (gross domestic product) will largely affects the energy consumption as seen in Figure 1.3(b). The energy consumption increases with the economy growth.
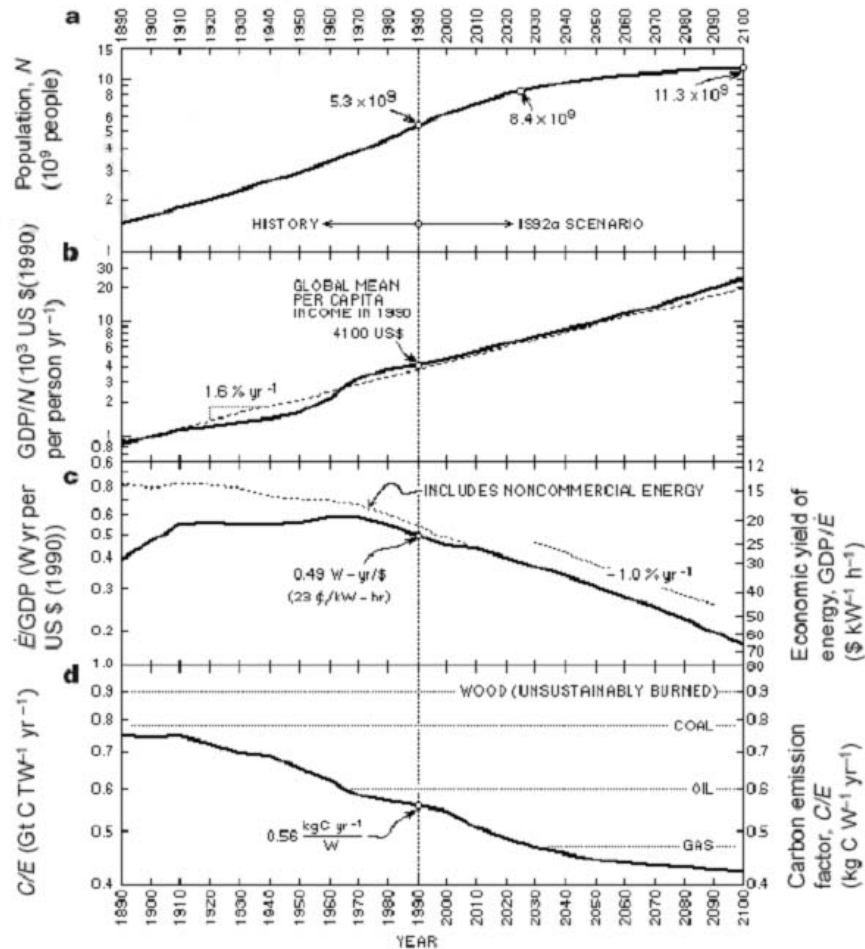
Figure 1.3. Evolution of factors governing the rate of global fossil-fuel carbon emissions in the world identity: Mc=N(GDP/N)(E/GDP)(C/E). Historical curves (1890–1990) are from archival data; future projections (1990–2100) are computed for the IPCC IS92a scenario. GDP is inflation-corrected to 1990 US dollars. a, Global population; b, Per capita GDP; c, Primary energy intensity (E/GDP: left hand scale) and economic productivity of energy (GDP/E: right hand scale); d, Carbon intensity of the energy mix; the horizontal lines are emission factors of individual carbonaceous fuels.

3

E/GDP, the primary energy intensity, increases with developing economy until sometime it reaches the peak as the infrastructure investment peak. Subsequently, the primary energy intensity starts decreasing due to the economy shifting to less-energy-incentive activities. This result is shown in Figure 1.3(c). Figure 1.3(d) shows the carbon emission intensity as a function of year. However, with the development of economy, less carbon or non-carbon energy is being discovered and largely used.

1.2 Energy Market

Since solar cells can directly convert solar radiation energy to electricity, potentially it can beat any other types of energy. The reason why solar cell is not largely used in the world is due to the high cost compared to any other types of energy, which can be clearly seen from Figure 1.4 showing the unit price of various energies [4].
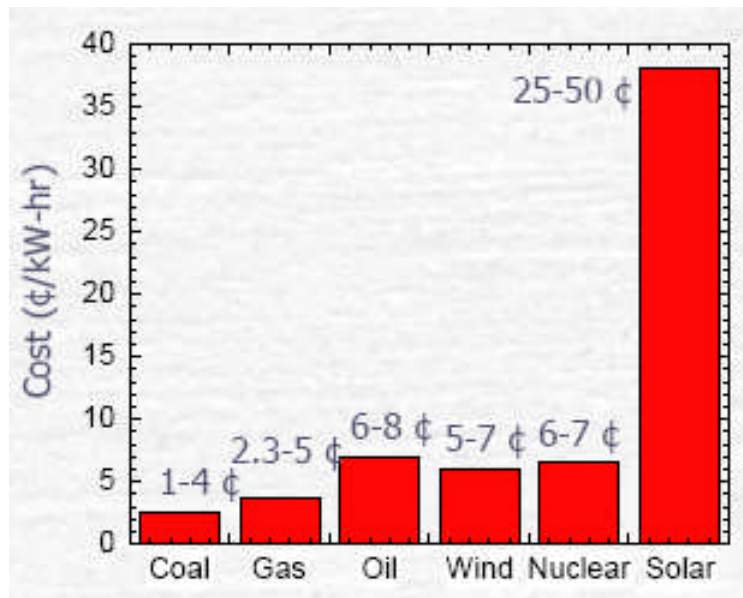
Figure 1.4 the unit price of the common type energy

Coal as one of the main energy types is widely used in the world because of several reasons. First, the large reservation can support the earth up to 1000 years. Second, the low cost due to the simple way of converting coal to electricity. The energy with highest unit price is

solar which is 13 times higher than coal and 6 times higher than oil, due to the high cost of the device which can convert solar radiation to electricity. Among energy types listed in Figure 1.4, only wind and solar energy are renewable. Based on the reservation, oil can be used for ~100 years, coal can be used for ~1000 years and natural gas can be used for ~400 years. Nuclear is non-renewable and can be obtained by either fusion or fission. Since U^{235} is a common precursor for fission with limited quantity on the earth, it can not last long time or substitute fossil fuel. Fusion using two types of hydrogen, deuterium and tritium as the precursor which are abundant in the world needs high temperature, over 5000 Cereus degree, to combine these two types of hydrogen nuclear, resulting in lack of such high temperature resistive material. Unless this technical problem is solved, it will not be new type of energy source under control. However wind and solar energy is renewable and may last forever. Wind is created by temperature gradient of different location which is the result of solar radiation on different latitude. Compared with solar energy, wind has a big problem of electricity generation discontinuity, but the device converting wind energy to electricity is much cheaper than solar cell resulting in the unit electricity price of wind much cheaper than oil. Anyway, cost is not the only issue blocking the development of renewable energy. In past 100 years oil and gas price is continually going up and at the same time, solar cell price is keeping reducing year by year. Although currently utilization of solar energy is expensive due to high cost of the device, solar energy still can be the future energy source potentially.

<u>1.3 Environment Impact</u>

Fossil energy is not clean, as it is made of carbon, hydrogen and other minor elements. During fossil fuel burning, large amount of carbon dioxide will be generated, absorbing inferred radiation, heating up like a thermal insulator and wrapping the earth. In this case, the globe warming problem results from the gradual increasing of carbon dioxide concentration in air.

Figure 1.5 shows the departure globe temperature as the function of year [4]. It is clearly seen that the temperature has positive increasing after 1980, especially in recent years.

This continues temperature increasing will cause various problems, like melting of ice in North Pole and South Pole, resulting in sea level increasing as well as disappearing some countries and islands. The increasing of carbon dioxide coming from combustion of coal, gasoline and other fossil fuel in the air is the main reason of temperature increasing. To avoid or reduce the carbon oxide generation, renewable energy or carbon free power such as solar energy is being developed.
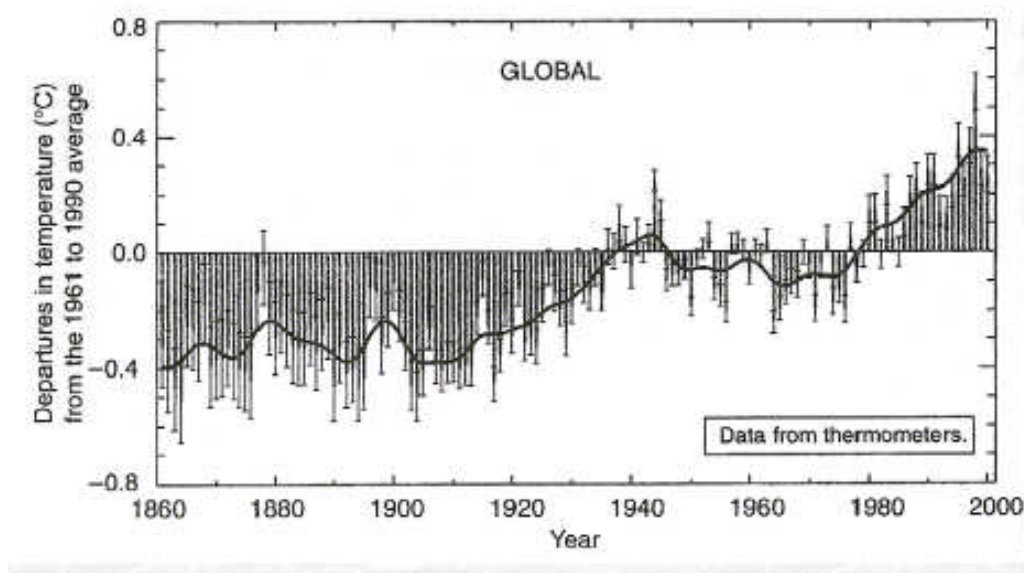
Figure 1.5 Departures in temperature with different year

1.4 Solar Cell History

In 1839, French scientist Edmond Becquerel firstly discovered the photovoltaic effect while experimenting with an electrolytic cell made up of two metal electrodes placed in a conducting solution when exposed to light. At the same time, he found out that this device could continuous generate very small power output under light radiation. Since that, people were interested in making such kind of electricity generator which can directly convert solar radiation to electrical power and is called solar cell or photovoltaic cell. In 1883, Charles Fritts, an American inventor, described the first solar cell made from selenium wafer. In 1954, photovoltaic technology was born in the United States when Daryl Chapin, Calvin Fuller, and

6

Gerald Pearson developed the silicon photovoltaic cell at Bell Labs-the first solar cell capable of converting enough sun energy into power to run everyday electrical equipment. Bell Telephone Laboratories produced a silicon solar cell with 4% efficiency and later achieved 11% efficiency. Later on the silicon solar cells was largely produced by solar cell manufactures. The theoretical efficiency of the silicon solar cell is 35.4% calculated from the bandgap of silicon [5], but up to now the highest efficiency of crystalline silicon wafer solar cell is 25% reported by University of New South Wales' ARC Photovoltaic Centre of Excellence [6]. At the same time, people realized the cost of crystal silicon based solar cell was too high due to the complex refining process of ultra pure silicon. In order to reduce the cost, thin film solar cell was being develop start that time. In 1986, ARCO Solar released the G-4000, the world's first commercial thin-film power module. Since then more and more attention were paid to the thin film solar cell. Currently, Si and CdTe thin film solar cell have been commercially produced, while CIGS, dye-sensitized and concentrated photovoltaic are still under study. However, all the thin film solar cells mentioned above still have problems like high cost, toxic, scarce etc. so that new thin film solar cell needs to be invented.

<u>1.5 Solar Cell Market</u>

In 2005, the photovoltaic industry grew almost 50% reaching a world-wide production volume of 1,759 MWp of photovoltaic modules and has become a $7 billion business. The current crystal silicon solar cell technologies are well-established and provide reliable products with sufficient efficiency and lifetime for at least 20 years. The reliability of solar cell, the increasing potential of electricity interruption due to grid overload and the rise of electricity prices from conventional energy sources, make Photovoltaic systems more attractive. Figure 1.6 shows the world solar cell module market from 1992 to 2001. From 1996 to 2001, the total solar cell module installation increased dramatically from 88.6 MW to 381.3 MW, 4 times larger. Based on this trend, it can be expected that a GW solar module market will be realized in the near future.
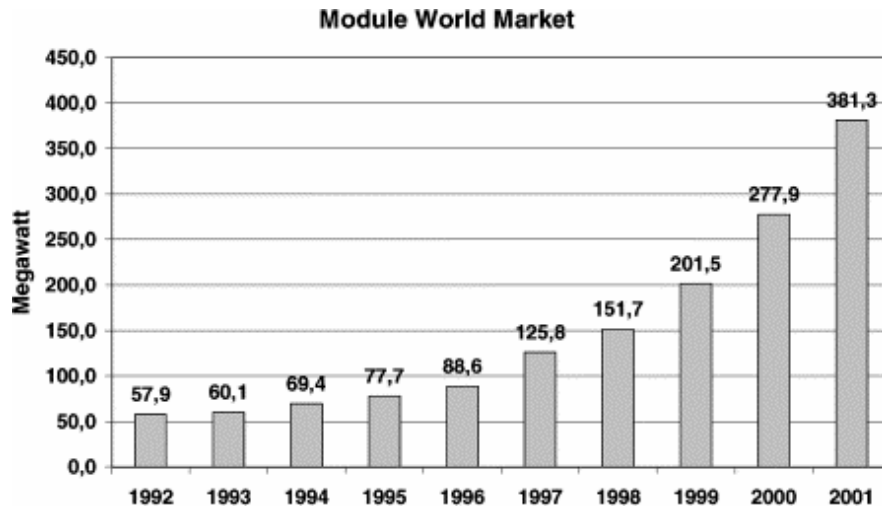
Figure 1.6 World solar cell module market

Figure 1.7 shows the module price and annual module production in the recent years. Nearly 30 years' development, the photovoltaic technique experiences a significant change, broadening mass production and increasing converting efficiency which results in decreasing solar cell module price. In 1976, the cost of the solar cell module was 78$/Wp, but at the end of 2006, the market price of the solar cell module decreased to 3.84$/Wp and annual production increased to 2.6 GWps/year. The annual production of single crystal silicon also increased from 1-5 MWps in 80's to 5-30 MWps in 90's, and it is being able to reach 25-500 MWps in the future. The large mass production of raw material, increased efficiency and decreased cost result in large scale industrialization of the solar cell.

About 90% of the current production uses wafer-based crystalline silicon technology. The first advantage of this technology is that complete production lines can be bought, and installed within a relatively short time. This predictable production start-up scenario constitutes a low-risk placement with high expectation for return on investments.
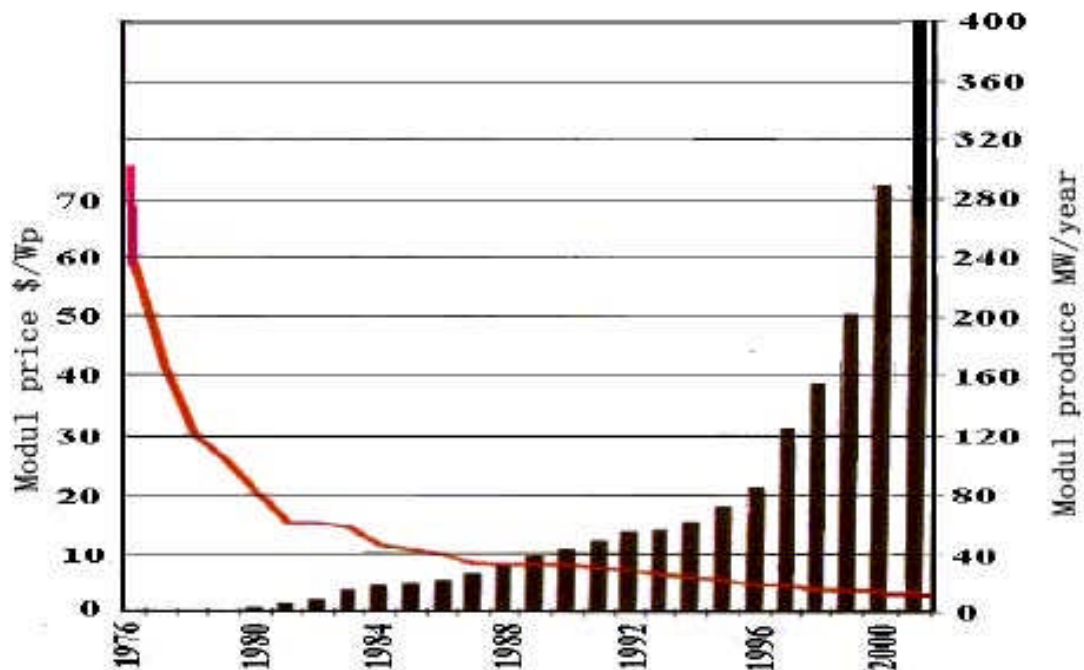
Figure 1.7 World solar cell module price and annual production

Figure 1.8 shows the market share of solar cell technology in the world in 2007. Crystal silicon solar cell including single crystal silicon and poly crystal silicon occupies around 86% of the photovoltaic market because of the mature fabrication technique which has been developed for tens of years and also their high efficiency close to the theoretical efficiency of the crystal silicon solar cell. The other solar cell techniques are thin film solar cell and ribbon silicon solar cell. Ribbon silicon solar cell needs high purity silicon raw material which blocks the large application in solar industry. In principle, since thin film solar cell consumes less material than crystal silicon solar cell, it should be cheaper than crystal silicon solar cell and is considered to be the next generation solar cell.
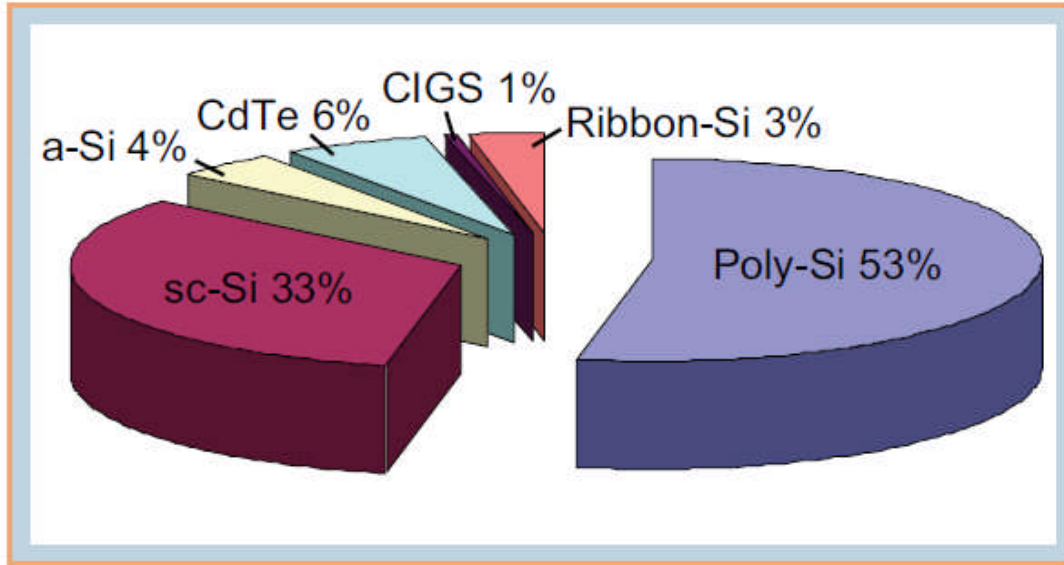
Figure 1.8 2007 World solar cell market by technology

Generally, solar cell has been classified into three generations. Figure 1.9 shows the efficiency and cost of three generation solar cells [4]. The first generation solar cell is crystal silicon solar cell which has the advantage of high efficiency, though the cost is high. The second generation solar cell is the thin film solar cell such as CdTe, CIGS and organic solar cell which reduce the cost but has their own disadvantages. Organic solar cell efficiency is relatively too low to be industrialized, the CIGS solar cell has the uniformity issue during process and CdTe the base material of CdTe thin film solar cell is a toxic material which may be harmful to environment. The third generation solar cell is tandem solar cell with high efficiency and low cost which is ideal for commercial using.
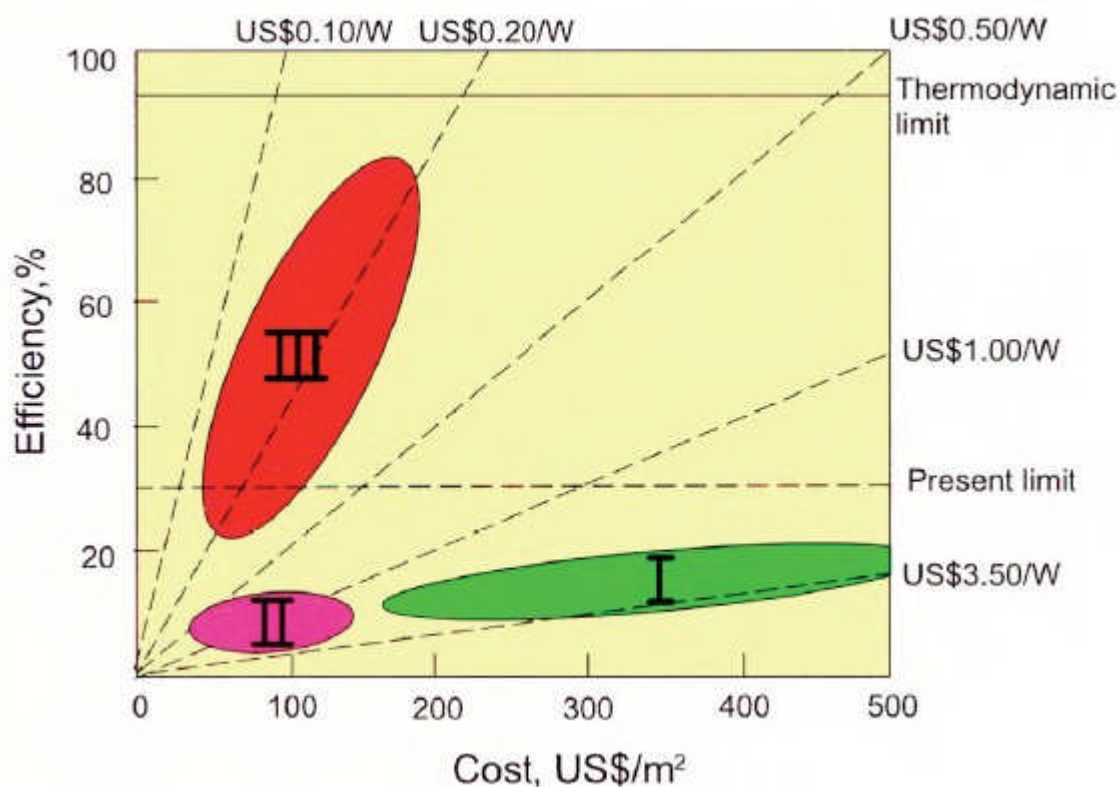
Figure 1.9 Cost/Efficiency of three generations

1.6 Research Objectives

In current stage, crystalline silicon solar cells with high efficiency and high product through-put dominate the solar cell market. However, due to complex and high requirement silicon refining procedures, the cost of crystalline silicon solar cells is high which limits in the wide application. People do want to get low cost materials to replace the high cost materials in the solar cells. Cuprous oxide (Cu_2O) is an intrinsic p-type low cost semiconductive material and it can be changed to n-type by changing the intrinsic point defects. The band gap of Cu_2O is 2.0 eV and the theoretical efficiency of Cu_2O solar cell is 19%. The problem with Cu_2O homojuction solar cell resulting in low efficiency is extremely high resistivity of both p-type and n-type Cu_2O. Another low cost material is ZnO, which is usually used as transparent conductive oxide (TCO). In order to work as a TCO layer in solar cell, the ZnO must be highly transparent and highly doped to very low resistivity. The objectives of research are listed as follows:

11

1. Find out the proper n-type dopants for both Cu_2O and ZnO

2. Use electrochemical co-deposition preparing the n-type doped Cu_2O and ZnO thin films

3. Characterize the morphology and crystal structure of Cu_2O and ZnO thin films

4. Characterize the electrical properties and optical properties of the Cu_2O and ZnO thin films

CHAPTER 2

BACKGROUND

2.1 Solar Cell Structure

The basic structure of solar cell is a diode, p-n junction, which is shown in Figure 2.1 [7]. The cell itself contains six layers which are front contact, antireflection coating, emitter layer, base layer, back surface field and back contact. The front contact is made of silver and back contact is aluminum coating and both are high conductive. The base layer and emitter layer contact with each other to form the main working part, p-n junction, while in silicon solar cell both of them are crystal silicon. Antireflection layer is designed for optical performance purpose which can inject more light into the junction to realize higher efficiency.
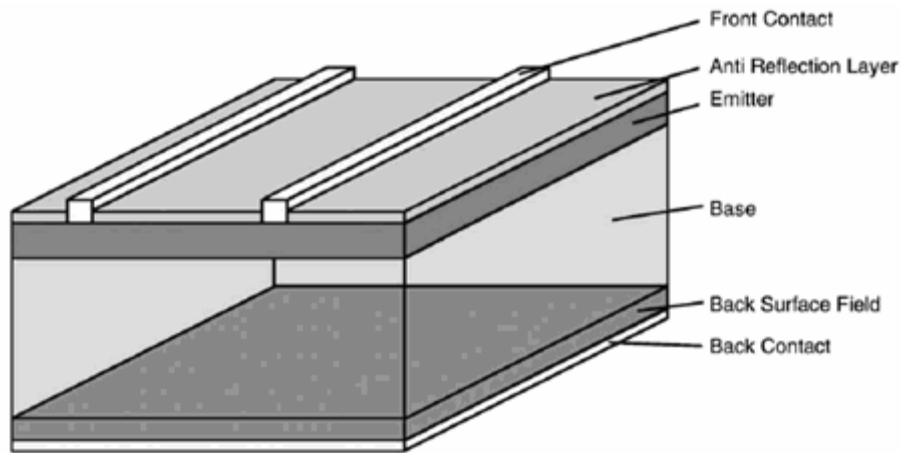
Figure 2.1 Typical structure of a solar cell

The mechanism of solar cell generating electricity is described in Figure 2.2. When the p-type semiconductor contacts with the n-type semiconductor, the Femi level of both p-type and n-type semiconductor will turn into same and a depletion region will be created in the contact area. Once the electron in the valence band of the depletion region absorbs light, it will be

13

excited and jump to the conduction band, and then electron-hole pair is generated. In the internal electrical field, the electron-hole pair will be separated under the internal electrical force and holes will go into valance band while electrons will go into conduction band. Once electrons and holes accumulate on the electrode, electricity is generated with an external load. The p-n junction in crystal silicon is made of p-type silicon and n-type silicon by thermal diffusion process, so called homo-junction. The main advantage of homo-junction is no crystal misfit between the p layer and the n layer.
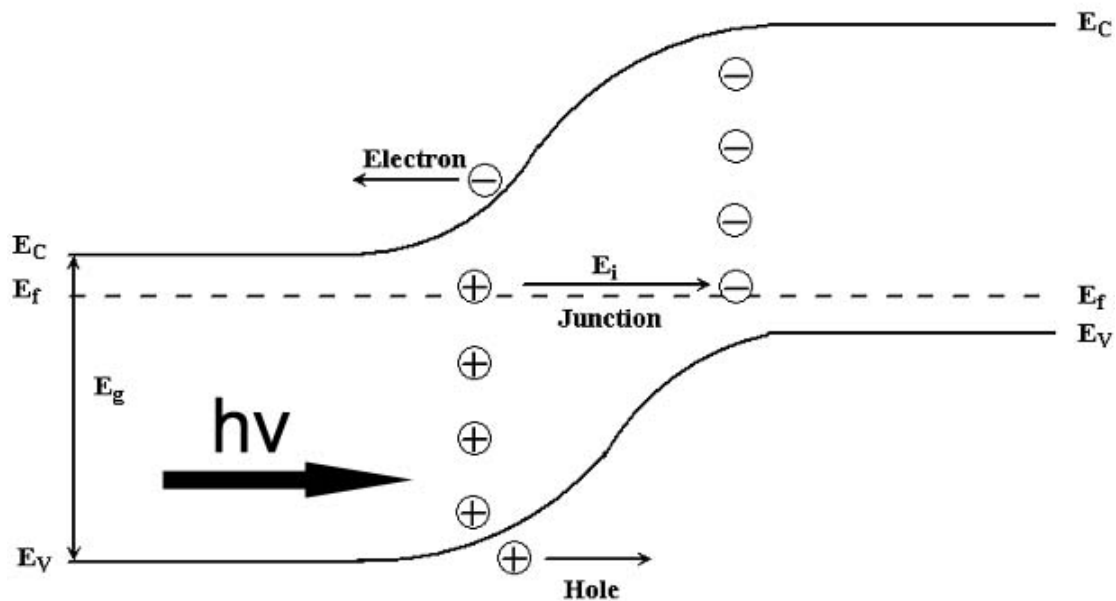
Figure 2.2 Schematic of solar cell working mechanism

Generally in crystal silicon solar cell, the p-type silicon layer is much thicker than the n-type silicon layer where most light (around 90%) can be absorbed. The back contact is aluminum which can also work as a mirror, and thus the total length of light passing through the cell is twice as the thickness of the wafer. Beside the back contact, to increase the light incidence intensity, surface texturing and anti-reflection coating are also used in the crystal

14

silicon solar cell. Surface texturing is a specific process making the cell top surface rough while in crystal silicon solar cell it is arrays of small pyramids made by directly etching silicon wafer. Another light enhance layer, anti-reflection coating, is made of Si_3N_4 or TiO_2. These two materials have light reflect index between that of glass and silicon. Once the light goes into this anti-reflection coating layer, the reflected light is minimized and the transmitted light is maximized.

<center>2.2 Solar Cell Materials</center>

Silicon is the most used semiconductive material in both semiconductor and solar cell industry. But it is not the optimum absorption material for solar cell because of indirect bandgap. People discovered amorphous Si is a direct bandgap material and H passivation can remove dangling bond defects. Currently, people achieved large progress on high efficiency amorphous Si solar cell. But the degradation of H bond is still major issue of amorphous silicon thin film solar cell which results in efficiency decaying over time and short lifetime under sun light exposure. Beside silicon, most III-V group compounds such as GaAs, InGaAs etc. are direct band gap semiconductor and can achieve higher efficiency thin film solar cell. The problem with III-V group compounds is that most group III and V elements are scarce in the world, so the semiconductors made by these elements can not support large scale solar cell fabrication. But these kinds of solar cell have wide application in the spacecrafts attributed to high efficiency.

Recently, II-VI group compounds are popular because most metal chalcogenides are abundant in the world and most of those materials are non-toxic. Two metal oxides are discussed in this dissertation, cuprous oxide and zinc oxide.

2.2.1 Cuprous Oxide

Cuprous oxide is known as p-type direct bandgap material which can be used in thin film solar cells. Copper is one of the most abundant metals as well as oxygen is one of the most abundant elements on the earth. Both pure copper and oxygen have large annual production with low unit price. The copper oxide has two phases: one is cuprous oxide and the other is

<center>15</center>

cupric oxide. Figure 2.3 shows the crystal structure of cuprous oxide (ICSD #26963). Cu is +1 charge valance and O is -2 charge valance in cuprous oxide structure. The cuprous oxide is FCC structure and Pn-3mS group space with lattice parameter a=4.261 Å.
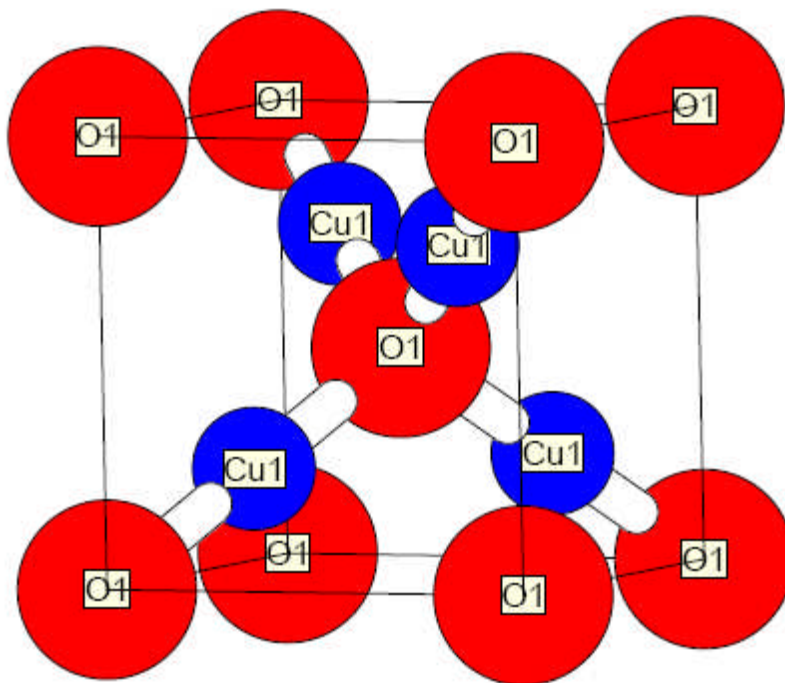
Figure 2.3 The crystal structure of cuprous oxide.

Cu_2O films can be prepared from solution including electrochemical deposition [8,9] and sol-gel-like dip coating [10] and thermal oxidation of copper film [11], promising low-cost fabrication of Cu_2O solar cells. Cu_2O solar cell has been reported with various cell structures like n-CdO/p-Cu_2O [12], n-ZnO/p-Cu_2O [13] and n-ITO/p-Cu_2O [14]. Although the theoretical efficiency of Cu_2O solar cells is ~19% [15], the best-reported efficiency is only ~2% [16]. The low efficiency was attributed to the naturally p-type conduction in Cu_2O, formed a copper-rich region at the metallurgical interfacial region of Cu_2O and other semiconductor or metal layer, which prevented a p-n junction in Cu_2O, the basic device structure in most inorganic solar cells [17]. In this case, a homo-junction of Cu_2O is needed to achieve high efficiency Cu_2O solar cell.

16

Both p-type and n-type Cu_2O thin films prepared by electrodeposition have been reported by W. Siripala and L. Wang et al and the conductive type was changed by controlling the pH of the deposition solutions [18, 19]. They also demonstrated a p-n homo-junction of Cu_2O prepared by two step electrochemical deposition with different solution pH [19].

(a)

Photo I-V

J_{sc}: 1.228 (mA/cm^2)
V_{oc}: 0.321 (V)
FF: 35.33 %
η: 0.15 %
Area: 0.01 cm^2
AM 1.0
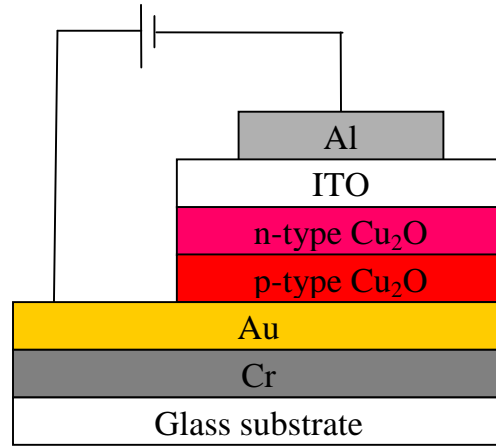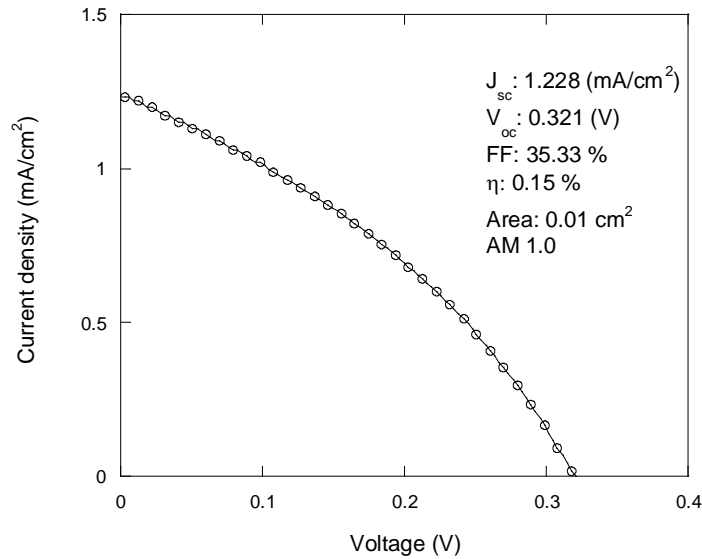
(b)

Figure 2.4 (a) Cu_2O p-n homojuction structure and (b) its photo I-V

A more detailed study of the Cu_2O p-n junction revealed highly-resistive n-type Cu_2O by electrochemical deposition in the range of 2.5×10^7 and 8.0×10^8 Ω-cm, leading to a low efficiency of ~0.1% for a solar cell built on the Cu_2O p-n junction [20]. Figure 2.4 shows the structure of Cu_2O p-n homojuction and the related photo I-V reported by K. Han etc [20]. The current is very low due to high resistivity of both p-type and n-type semiconductor. The area of the cell was designed to only 0.01 cm^2 for avoiding the uniformity problem.

2.2.2 Zinc Oxide

ZnO is a well-known transparent semiconductor with wide direct bandgap 3.3 eV. It is of interest to optical and electronic industries, especially to solar cell industry. ZnO thin film can be used in optical electronics [21], TFT displayers [22], chemical sensors [23] and photovoltaics [24]. However, currently Indium tin oxide (ITO) is widely used as transparent conductive oxide (TCO) layer in solar cells attribute to low resistivity and high transparent. But In is scarce in the world plus high cost of using a vacuum process such as sputtering to deposit ITO [25]. Compared to ITO, ZnO has advantages of low cost and abundant. It is hexagonal structure and P63mc group space with parameter is a=3.25 Å, c=5.21 Å. Zn is +2 charge valance and O is -2 charge valance. Figure 2.5 shows the crystal structure of ZnO (ICSD #26170).

Figure 2.6 shows the structure of commercial solar cell [26]. The thin oxide layer is made of ZnO with quarter wavelength thick and low resistivity. On one hand, low resistivity promotes more electrons collection; on the other hand, quarter wavelength thickness of ZnO can also work as an anti-reflection coating injecting more light into the cell. There are several ways to prepare this ZnO layer, such as radio frequency magnetron sputtering [27], chemical vapor deposition [24, 28], molecular beam epitaxy [29,30], electrodeposition [35] etc. But the undoped ZnO with high sheet resistance can not be directly used in solar cell or other electronics for electron collection purpose. Group IIIA elements like Al, Ga and In can work as n-type dopant in ZnO structure. The lowest resistivity reported for Al-doped ZnO is in the mid to high 10^{-5} Ω-cm range by magnetron sputtering at room temperature [31] or pulsed laser

deposition below 300 °C,[32] while the majority of the resistivity results by vacuum-based deposition is around 2×10^{-4} Ω-cm [33].
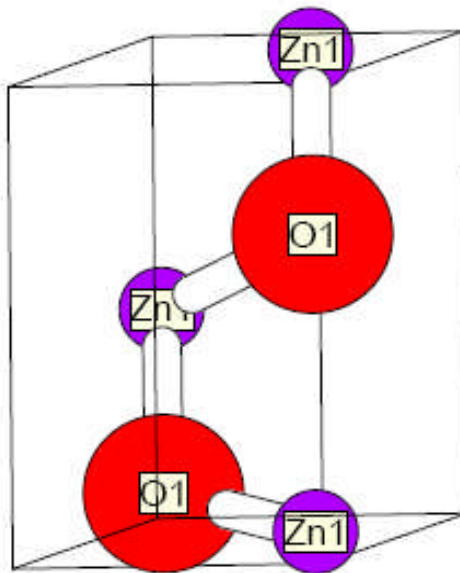
Figure 2.5 The crystal unit cell of cuprous oxide.
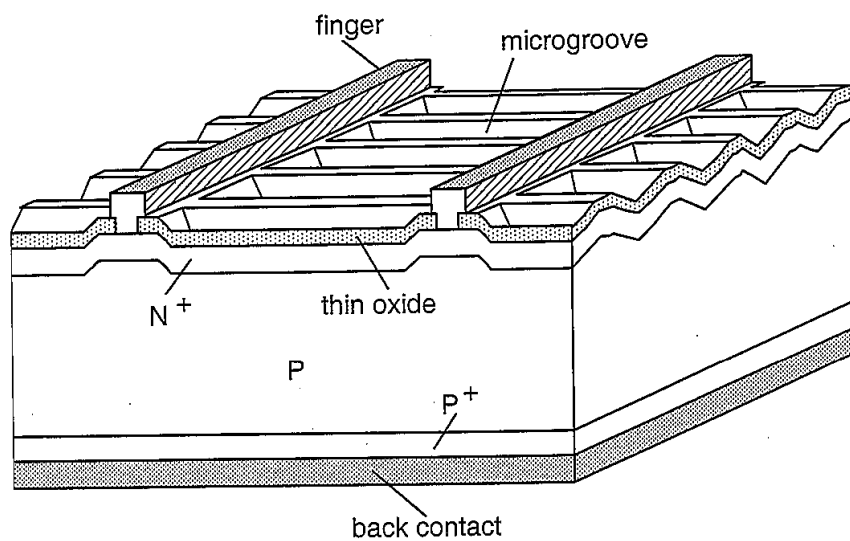
Figure 2.6 Passivated emitter solar cell (PESC)

<u>2.3 Deposition Methods</u>

2.3.1 Vacuum Deposition

     Vacuum process, including CVD, sputtering and e-beam evaporating etc., can deposit different kinds of metal and metal oxide thin film. It is an atom by atom or molecular by molecular deposition process at a sub-atmospheric pressure on a solid state substrate. This process is usually performed at a low pressure so it requires a large chamber to hold the substrates. Since it is achieved in a closed ambient, it can not use roll to roll technique which blocks its large scale application. In other hand, this physical process can get more uniform and higher quality film than solution-based methods, so a lot of manufactories still use vacuum deposition for preparing transparent conductive oxide layer and other solar cell materials. PVD and CVD are two kinds of vacuum deposition mostly used.

     PVD is the abbreviation of Physical Vapor Deposition, which means under the vacuum condition, using physic method like high voltage, high current or high energy electron beam to evaporate the source materials and deposit the material onto the substrates.

     The chemical vapor deposition (brief name CVD) is a kind of chemical technique for producing high purity and quality solid materials. In semi-conductor industry, it is used to grow thin solid films. The typical CVD process is first exposing a wafer (base) under various different forerunner things and then chemical reaction happens on the substrate surface where the film is depositing. This process usually accompanies with some hard to get rid of by-products which may erode the side of the camber. These by-product will stick on the camber wall and become thicker and thicker, and then at a certain time it will fall on the substrate and contaminate the sample.

2.3.2 Solution-Based Deposition

     Beside vacuum deposition, solution based deposition is also largely used for metal oxides thin film synthesis. Compared to vacuum deposition, the advantages of solution-based

20

are low temperature, atmosphere ambient, low cost and large scale capability. Recently several solution based deposition methods of metal oxide thin film deposition have been studied, like successful atomic ion layer deposition (SAILD) [34], electrodeposition (ED) [35], chemical bath deposition (CBD) [36] and spray pyrolysis deposition (SPD) [37].

Solution-based deposition usually starts with a clear solution or a colloidal solution. Reaction happens in the solution with additional energy source such as heat, light, pH, pressure etc. The reaction creates the metal oxide or metal hydroxide films which can stick on the substrate. If metal hydroxide film is deposited, additional process is required to convert it to oxide.

2.4 Doping in Metal Oxides

Doping is a prerequisite for high performance in almost all semiconductor devices. It controls the conduction type (n- or p- type) and resistivity of the semiconductor. In the conventional semiconductor technology, doping is accomplished by one of the following methods:

1) Diffusion of a dopant into semiconductor at high temperatures;

2) Ion implantation of a dopant into semiconductor by its energetic ions; or

3) Co-deposition of a dopant with semiconductor during vapor deposition.

All these methods require high temperatures around ~1,000 °C and vacuum systems to prevent the unwanted effects of the air on the process. Therefore, these methods are inherently energy-intensive, low-throughput and high-cost. One approach to reduce the cost of next-generation solar cells is to employ as many solution-based processes as possible to replace conventional vacuum-based processes for cell fabrication. Solution-based processes are particularly suitable for low-cost solar cells, since they are energy-efficient, low-cost, high-throughput and capable of large-area processing.
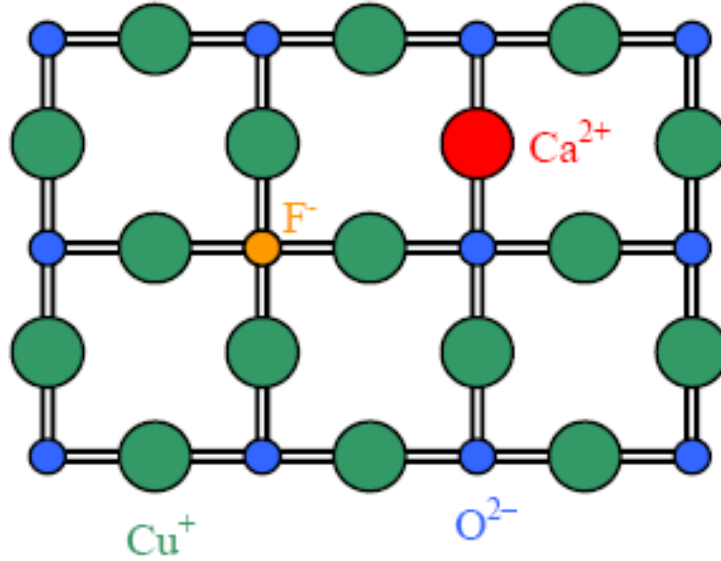
Figure 2.7 Schematic illustrating potential n-type dopants for Cu and O sites in Cu_2O.

Without doping, both intrinsic ZnO and Cu_2O have such high resistivity that they can not be used in solar cell. In order to reduce the resistivity of ZnO and Cu_2O, doping technique has been discussed here. First of all, n-type dopants need to be identified for ZnO and Cu_2O. Take Si as an example. Since it is a group IV element, a Group V element, such as As, constitutes an n-type dopant for it provides an extra electron to the Si lattice. On the other hand, a group III element such as Al becomes a p-type dopant, since it has one fewer valence electron than Si. Substitutional n-type doping in chalcogenides can go into either the cation or anion site, so the valence argument is more complicated.

In ZnO, Zn has two valence electrons and O has six valence electrons. If the dopant atom occupies a Zn site in ZnO, group III elements, such as Al and Ga, become possibilities for n-type doping. However, if the dopant atom occupies an O site in ZnO, group VII elements, such as Cl and B, ought to be looked at for n-type doping. In Cu_2O, Cu has one valence electron and O has six. Similarly, if the dopant atom occupies a Cu site in Cu_2O, group II elements, such as Mg and Ca, are possible n-type dopants (Figure 2.7). For the O site in Cu_2O,

group VII elements are again potential n-type dopants. Table 2.1 lists n-type dopant candidates for ZnO and Cu_2O based on this valence argument. Halogen substitution of chalcogen is particularly attractive as a universal n-type doping technique for all chalcogenides, while cation substitution has to be worked out for different chalcogenides on a case-by-case basis depending on the valence of the metal.

Table 2.1 Potential n-Type Dopants for ZnO and Cu_2O.

ZnO		Cu_2O	
Zn site	O site	Cu site	O site
Al, Ga	Cl, Br	Mg, Ca	Cl, Br

It is also interesting to look into p-type doping in ZnO and Cu_2O. For the O site, group V elements, such as P and N, are possible p-type dopants for both ZnO and Cu_2O. For the Zn site in ZnO, group I elements, such as Na and K, may serve as p-type dopants. However, for the Cu site in Cu_2O, p-type doping requires in principle a group VIII element which provides no electron to the Cu_2O lattice. This is because Cu has one valence electron in Cu_2O. It is practically difficult to incorporate a group VIII element into Cu_2O since it does not form any chemical bond in the lattice.

2.5 Electrodeposition of Metal Oxides

Electrochemical deposition, a solution-based method, is used to deposit uniform thin films or variation structures [35]. Electrodeposition by passing a current through an electrochemical cell from an external power source has chemicals reacting on the electrodes. Three electrodes electrochemical cell is usually used for electrodeposition containing working electrode, counter electrode and reference electrode. The counter electrode can vary depending on the experiment purpose. Usually, Pt as the inertest metal in the world is used as the count electrode. Other materials such like graphite, class carbon also can be used as the

counter electrode in some cases. The reference electrode has stable and well-known potential. People defined standard hydrogen reduction potential as 0 V. Table 2.2 shows the potential of common reference electrodes. The saturated calomel electrode (SCE) and silver chloride electrode are normally used in the lab because of cheap price and easy manipulating. The working electrode can be metal, semiconductor or other conductive material. The conductivity of the working electrode will affect the reaction rate. The substrate as working electrode must have good adhesion to metal oxides. The electrodeposition rate can be controlled by the potential applied on the working electrode, the conductivity of solution and solution temperature etc. Figure 2.8 shows the typical three electrodes electrochemical cell for Cu_2O deposition. The reason using three electrodes is to precisely control the potential applied on the working electrode which refers to the reference electrode. In this case, the reference electrode should be closed to the working electrode. The counter electrode is designed for conducting current and the reactions are usually controllable on the counter electrode.

The advantages of electrodeposition compared to other techniques are low process temperature, low cost and the capability of controlling morphology and orientation of the deposited films. By controlling the amount of total charge passing through the cell, the thickness of deposited film can be precisely controlled, revealed by Faraday first rule, the relationship between charge and mole amount of chemical reaction product. The following equation shows the Faraday fist rule:

$$\Delta m = kq = kIt'$$

Δm is the amount of chemical reaction product; k is the ratio factor and q is the total charge. k is determined by the valence charge difference between the raw material and the final product. The average thickness of the film can be calculated from the following equation:

$$t = \Delta m \bullet m_a / (\rho A N_a)$$

24

t is the thickness of the film; ma is the atomic mass of the material; ρ is the density of the material; A is the area of the film and Na is the Avogadro constant.
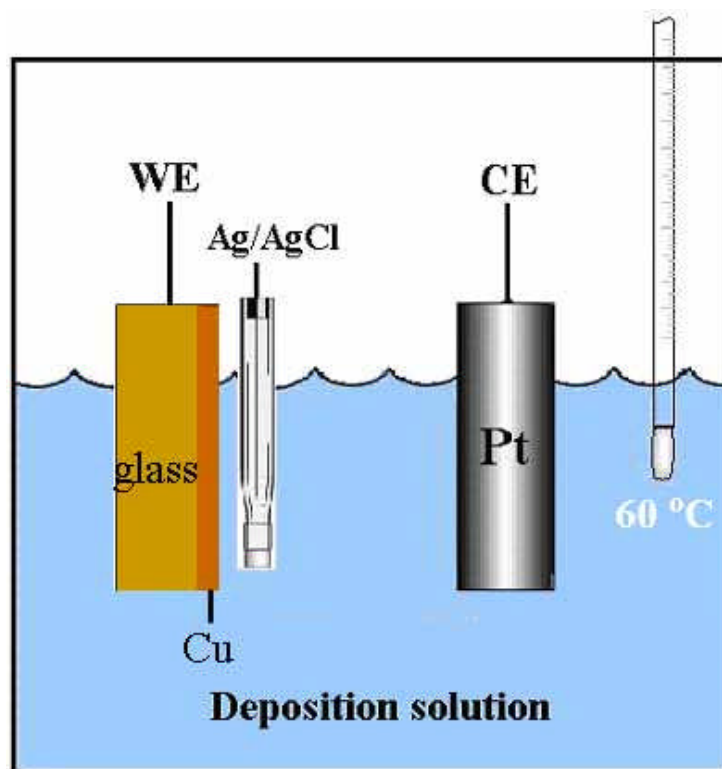
Figure 2.8 Three electrodes electrochemical cell

Table 2.2 The Potential of Different Types of Reference Electrodes

Reference electrode type	Potential (V)
Standard hydrogen electrode (SHE)	0
Normal hydrogen electrode (NHE)	≈ 0
Reversible hydrogen electrode (RHE)	$0 - 0.0591 \times pH$
Saturated calomel electrode (SCE)	0.242
Copper-copper(II) sulfate electrode	0.314
Silver chloride electrode	0.197

Based on the current direction, electrodeposition can be classified into two catalogs, cathodic electrodeposition and anodic electrodeposition. Cathodic electrodeposition is mostly used to deposit absorption thin film layer in solar cell, with advantages of high through put and easy control.

Generally, the cathodic electrodeposition is described as following equation:

$$P(M)_{solution} + P(O)_{solution/gas} + e^-{}_{substrate} = MO_{product}$$
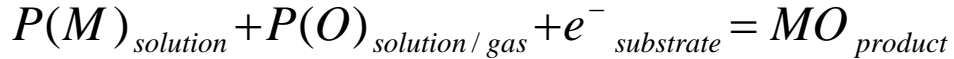
Metal oxide can be obtained from the decomposition of metal hydroxide with thermal treatment produced by metal and oxygen precursor during the deposition. Hydroxyl ions are used as the oxygen precursor and can be obtained by two methods. One is directly changing the solution pH value by adding alkali. But this method usually requires complex agent to stabilize the metal ion in high pH value solution. Once the metal ion get electrons from substrate, the valence of the metal ion will be changed, and then the metal ion becomes unstable with the complex agent and comes out to react with hydroxyl ions to form metal hydroxide. The other method is using water or other oxygen compounds, O_2 [38], H_2O_2 [39] or NO_3^- [40], to generate hydroxyl ions by getting electrons. The local pH will increase and metal ions become metal hydroxide precipitated on the substrate electrode.

$$NO_3^- + H_2O + 2e^- \rightarrow NO_2^- + 2OH^- \tag{1}$$

$$H_2O_2 + 2e^- \rightarrow 2OH^- \tag{2}$$

$$O_2 + 2H_2O + 4e^- \rightarrow 4OH^- \tag{3}$$
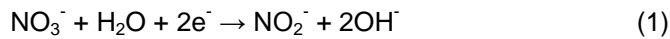
Cathodic electrodeposition of p-type Cu_2O was firstly discovered in 1983 [41]. W. Siripala etc. discovered the Cu_2O film electrodeposited at low pH shown n-type conductivity type due to oxygen vacancy [18]. L. Wang etc. fabricated Cu_2O p-n homojuction structure by electrodeposition [19]. Peulon etc.[42],[43] described the cathodic electrodeposition of ZnO from an oxygenated aqueous zinc salt solution and Izaki etc. reported on the cathodic electrodeposition of ZnO from aqueous zinc nitrate solutions [44-46]. The first successful

attempt to use electrodeposited ZnO as window layers for $Cu(In,Ga)Se_2$ (CIGS) cells has been reported with cell efficiency approaching 10% [47].

Electrochemical deposition of mixed metal oxide was reported and several metal oxide alloys were successfully prepared such as $La_{1-x}Ca_xCrO_3$ [48], $LaFeO_3$ [49], $La_{1-x}Ca_xMnO_{3+\delta}$ [50] and $Cd_xZn_{1-x}O$ [51] etc. If keep the additional cation or anion as the dopant at low quantity, they can be cooperated into the metal oxide structure and result in significant change of the electrical properties of the metal oxide.

<u>2.6 Previous Works on Doping in Metal Oxides</u>

2.6.1 Doping in cuprous oxide

Group VII elements can be the n-type dopant for Cu_2O by substituting Cu atoms. A.O. Musa etc. firstly tried Cl doped Cu_2O by using Cl vapor as the dopant precursor. In their report, the Cu_2O thin film was prepared by thermal oxidation with resistivity of 3.7×10^3 Ω-cm, while with Cl doping the resistivity of the Cu_2O film was reduced to 2.4×10^2 Ω-cm [52]. They also claimed the Cl was distributed throughout Cu_2O grains uniformly as a p-type dapont. L.C. Olsen has suggested that Cl may have two possibilities in conductivity type. First that, chlorine might lead to an acceptor level, if it enters the lattice as a neutral atom at an interstitial site. The second is that chlorine may replace oxygen substitutionally, thus resulting in a donor level, which in turn could cause copper vacancy production due to charge compensation effects [53].

Any metal element with charge valence more than +1 in ionic state can be n-type dopant by substituting Cu atoms in Cu_2O structure. S. N. Kale etc. reported Al, V and Zn doped Cu_2O thin film on the MgO substrate prepared by pulsed laser deposition with Al, V and Zn presented in the target. The resistivity of the undoped Cu_2O prepared by their method was 225 Ω-cm and the resistivity of Zn doped Cu_2O was reduced to 45 Ω-cm. However, with Al and Co dopant the resistivity of the Cu_2O thin films increased [54].

All group V elements can be used as n-type dopant in Cu_2O structure. N doped Cu_2O thin films deposited by reactive radio-frequency magnetron sputtering were reported by S. Ishizuka

etc. The lowest resistivity of the Cu_2O thin film was 15.2 Ω-cm with 400 °C deposition temperature and N_2 flowing rate of 20 ml/min [55].

2.3.1 Doping in zinc oxide

N type doping in zinc oxide has been already well studied. Normally all group III elements can work as n-type dopant substituting Zn atoms in ZnO structure. Al doping in ZnO thin film can be realized by pulsed laser deposition [56], radio frequency magnetron sputtering [57], and sol–gel process [58] etc. are reported. The lowest resistivity of Al doped ZnO film is achieved by vacuum based deposition which is 2×10^4 Ω-cm. In that paper, it is also reported that the lowest resistivity is in the range of 1.4 to 2×10^4 Ω-cm regardless of deposition method and below 1×10^4 Ω-cm resistivity is hard to achieve due to a general limitation by ionized impurity scattering [59]. Other dopants like Ga, In etc. are also studied, but due to low world reservation or anneal production they are not used in solar cell industry [60,61]. Group VII can substitute O atoms in ZnO structure and also behave as n-type dopant. The lowest resistivity of F doped ZnO is 6.5×10^4 Ω-cm while the fluorine concentration in the film is 0.5% by atmospheric pressure chemical vapor deposition reported by J. Hu etc [62]. E. Chikoidze etc. has reported with chlorine doping the lowest resistivity of ZnO can be brought to 3.6×10^3 Ω-cm by metal-organic chemical vapor deposition which is much higher than the lowest resistivity of fluorine doped ZnO [62].

P type doped ZnO is of interest in optoelectronic device industry. Typically, group I elements can be the p-type dopant in ZnO structure by substituting Zn atoms and group V elements can also be the p-type dopant in ZnO structure by substituting O atoms. Several mechanisms leading to p-type doping difficulty are known: low solubility, compensation by low-energy native defects, deep impurity level, and structural bistability known as AX and DX centers [63].

CHAPTER 3
CHARACTERIZATION OF Cl-DDOPED N-TYPE Cu$_2$O PREPARED BY

ELECTRODEPOSITION

3.1 Introduction

Cu$_2$O, with its 2.0 eV direct band gap, non-toxicity, and abundance of source materials, is of interest to photovoltaic companies [64, 65]. Although the theoretical efficiency of Cu$_2$O solar cells is 19%, the best-reported efficiency is only 2% [13]. Cu$_2$O is naturally p-type. The dominant native point defect, Cu vacancies, creates an acceptor level of 0.4 eV above the valence band [66]. n-type Cu$_2$O by electrodeposition have been reported, and O vacancies are suggested to be the origin of n-type conductivity in Cu$_2$O [15]. A more detailed study reveals highly-resistive n-type Cu$_2$O by electrodeposition in the range of 2.5×10^7 and 8.0×10^8 Ω-cm, leading to a low efficiency of 0.15% for solar cells built on Cu$_2$O homogeneous p-n junctions [17]. Group V elements with five valence electrons can substitute the O sites as p-type dopant. N doped Cu$_2$O has been achieved by sputtering with N$_2$ gas [67,68]. But no n-type doping of Cu$_2$O has been reported yet.

In this chapter, a novel n type doping method of Cu$_2$O is discussed. In principle, all group VII elements can substitute O in Cu$_2$O and behave as n-type dopant and all group III elements can substitute Cu in Cu$_2$O and also behave as n-type dopant. Here Cl was chosen as the n-type dopant because the CuCl is insoluble in the aqueous solution. In addition, Cl is reasonably size-matched to O based on the difference of the ionic radius of Cl and O (Cl: 1.81Å; O: 1.4 Å). Cl doped Cu$_2$O was achieved through an electrochemical co-deposition process and a detailed study is presented here on the effects of doping conditions on the resistivity of Cl-doped Cu$_2$O, including Cu and Cl concentrations, different Cu and Cl precursors, complex agent concentration, solution pH, and deposition temperature. The lowest resistivity achieved so far by

Cl doping is 7 Ω-cm, which is suitable for solar cell applications. The solution-based doping method is particularly suitable for low-cost, large-area, and high-throughput fabrication of solar cells.

<div align="center">3.2 Experiment</div>

3.2.1 *Sample Preparation*

Electrodeposition was carried out using a Princeton Applied Research VERSTAT II potentiostat. The three-electrode electrochemical cell included a Pt counter electrode, a Ag/AgCl/saturated NaCl reference electrode, and a rectangular Cu-coated glass substrate and Au coated glass substrate as the working electrode with a typical size of 1×4 cm^2. The thickness of the Cu film was 400 nm and that of the Au film 150 nm, which were deposited in a NRC thermal evaporator. Prior to electrodeposition, the Cu- and Au-coated glass substrates were rinsed with acetone and then sonicated in distilled water for 15 minutes. The deposition solution contained $CuSO_4$ and $NaC_3H_5O_3$ (Na Lactate, 60% w/w aqueous solution), with different solution pH adjusted by adding 4 M NaOH [12]. $CuSO_4$ was first dissolved in de-ionized water to the desired concentration. $NaC_3H_5O_3$ was then added to the solution to 4 M. The lactate served as the complexing agent to prevent Cu precipitation when NaOH was added to the solution. For deposition of undoped n-type Cu_2O, solution pH was adjusted to below 9 [16]. $CuCl_2$ and NaCl were used as the Cl precursor with different mole concentrations to control the doping level in Cu_2O. The deposition temperature was controlled by a Precision 280 water bath. The deposition time was 1 hour and the film thickness was 300±30 nm. All the chemicals used were reagent grade.

3.2.2 *Sample Properties Characterization Process*

The thickness of the Cu_2O films was measured with a KLA-Tencor Alpha-Step IQ profilometer. The morphology of the Cu_2O films was analyzed with a ZEISS Supra 55 VP scanning electron microscope (SEM) with a nominal electron beam voltage of 5 kV. XRD patterns of the films were obtained with a Siemens D-500 powder diffractometer using $Cu_{K\alpha}$

radiation. The XRD data were collected at scan step of 0.02°, scan speed of 2.4°/min, 40 kV, and 30 mA. Photocurrent characterization was carried out in a three-electrode electrochemical cell with a broad-spectrum 90-W white lamp shining onto the working electrode, with the light chopped on and off by a rotating disk. A Pt foil, an Ag/AgCl/saturated NaCl reference electrode, and the Cu_2O film were used as the counter, reference, and working electrode, respectively. For photocurrent measurements, the solution contained 0.5 M Na_2SO_4.

To measure the resistivity of Cl-doped Cu_2O, circular dots of Cu were deposited as the top electrode by thermal evaporation through a custom-made shadow mask onto the Cu_2O films. The area of the dot electrodes was 3.6×10^{-4} cm^2. Current-voltage (I-V) characterization was performed between the top electrodes and the Cu film on the substrate with a HP 4155C semiconductor parameter analyzer. Figure 3.1 illustrates the structure for I-V measurements. From the slope of the I-V relation, which behaved linear, the resistance of the Cu_2O film was determined. With the thickness measured by a profilometer, the resistivity of the Cu_2O film was calculated according to:

$$\rho = \frac{V \times A}{L \times I}$$

where ρ is the resistivity of the Cu_2O film, A is the area of the Cu dot, L is the thickness of the Cu_2O film, V is the applied voltage, and I is the measured current.
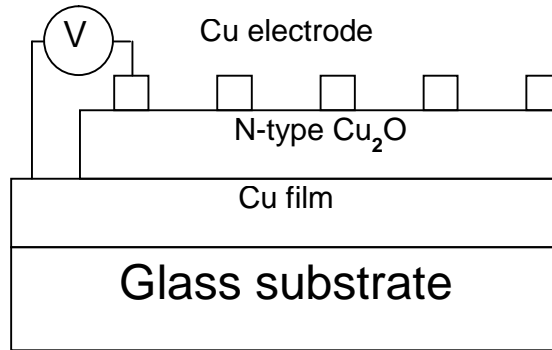
Figure 3.1 Schematic of the Cu/Cl-doped Cu_2O/Cu/glass structure for current-voltage characterization.

3.2.3 Doping Mechanism
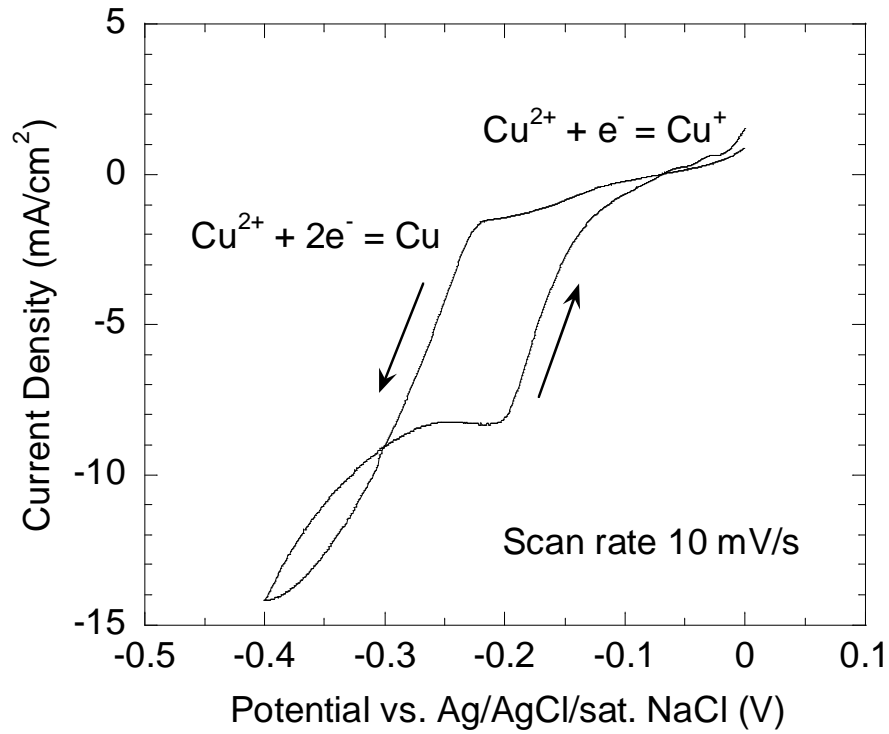
Figure 3.2 Cyclic voltammetry of a deposition solution containing 0.3 M CuSO$_4$, 4 M NaC$_3$H$_5$O$_3$ and 0.1 M CuCl$_2$. The solution temperature is 60°C and solution pH 7.5. There are two reduction reactions for Cu^{2+} ions, which lead to (1) Cu$^+$ ions and (2) metallic Cu. The reduction potential for Cu$^+$ ions is between –0.05 and –0.15 V.

Electrodeposition of Cu$_2$O is achieved by applying a constant potential between a Cu-coated glass substrate (working electrode) and a Pt foil (counter electrode). Before deposition, cyclic voltammetry is performed in a deposition solution containing 0.1 M CuCl$_2$ at 60 °C. As shown in Figure 3.2, cyclic voltammetry reveals two reduction reactions for Cu^{2+} ions: one leads to Cu$^+$ ions and the other to metallic Cu

$$Cu^{2+} + e^- \rightarrow Cu^+ \qquad\qquad (R1)$$

$$Cu^{2+} + 2e^- \rightarrow Cu \qquad\qquad (R2)$$
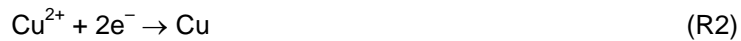
The potential for reaction R1 is between –0.05 and –0.15 V vs. the Ag/AgCl/saturated NaCl reference electrode. Compare to the previous report [19], the R1 reaction range shift a little bit

to the positive range. Usually, Cl ion will change the copper transaction point in electrodepositing copper, so here Cl ion also changed the cuprous ion transaction point. In this study, −0.1 V was chosen as the deposition potential applied to the working electrode. The produced Cu^+ ions react with OH^- ions in the solution to form Cu_2O [103].

$$2Cu^+ + 2OH^- \rightarrow Cu_2O\downarrow + H_2O \qquad\qquad (R3)$$

With the presence of Cl^- ions in the solution, Cu^+ ions also react with Cl^- ions to form CuCl, which incorporates Cl into Cu_2O and thus dope the Cu_2O film

$$Cu^+ + Cl^- \rightarrow CuCl\downarrow \qquad\qquad (R4)$$

The solubility product constant of CuCl, i.e. the product of $[Cu^+]$ and $[Cl^-]$, is 1.72×10^{-7} at 25°C [71]. This means that even small amounts of Cu^+ and Cl^- in the solution will react with each other and form solid CuCl.

3.3 Electrical Properties of Cl-Doped Cu_2O

3.3.1 *Conductivity Type Measurement of Cu_2O*

Several samples have been prepared with different $CuCl_2$ concentrations in the deposition solution at 60 °C. All the samples appear polycrystalline with a gain size of ~100 nm. The thickness of the films is controlled to between 300 and 400 nm, measured with a profilometer. After deposition, photocurrent measurements are performed to determine the conduction type of the Cl-doped Cu_2O samples. Figure 3.3 show the schematic of the set of photocurrent measurement. There is light shining into the electrochemical cell on the working electrode which is coated by the cuprous oxide. A light chopper is used to control the light on and off depending on the time. The electrochemical cell contains the cuprous oxide sample working electrode, Ag/AgCl reference electrode and platinum counter electrode. The electrolyte in the electrochemical cell is 0.5 M Na_2SO_4 solution. This measurement was carried out under room temperature.
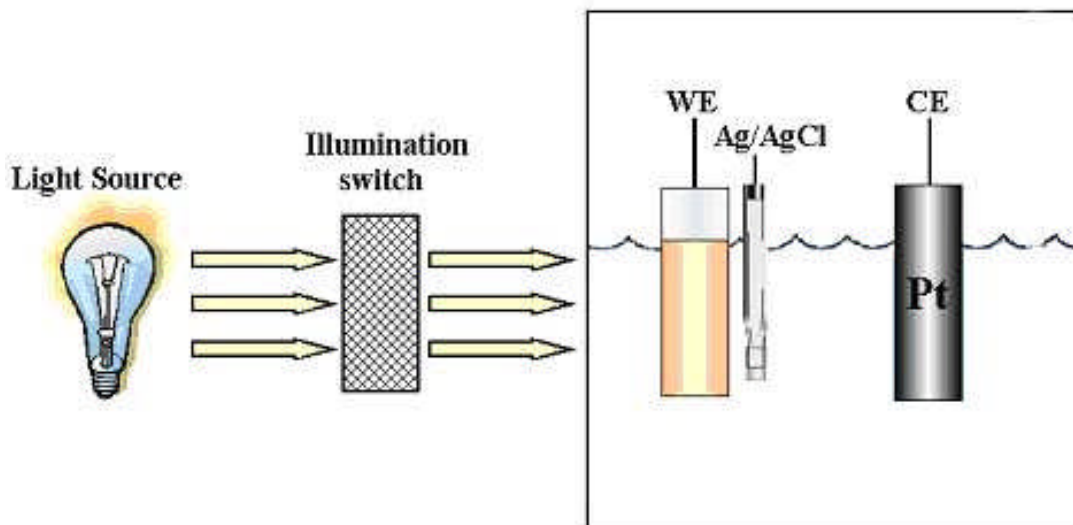
Figure 3.3 The set of photocurrent measurement.

The mechanism of this photocurrent measurement can be described in Figure 3.4. If the working electrode is an n-type semiconductor, before it contacts with the solution which has lower redox potential than the Femi level of the semiconductor, the band diagram shows in Figure 3.4(a). After the semiconductor contacts with the solution, the electrons in semiconductor will move into solution and a depletion region will form on the interface of the semiconductor. Once the light illuminate on this depletion region, the electrons will jump to the conduction band and move towards electrode side and hole will move into the solution which shows in Figure 3.4(c). Therefore, a positive photocurrent will be generated. When a p-type semiconductor contacts with high redox potential solution, the band diagram will be like Figure 3.4(d)(e). Figure 3.4(d) shows the band diagram before the p-type semiconductor contacts with the solution and Figure 3.4(e) shows the band diagram after the p-type semiconductor contacts with the solution. In Figure 3.4(e), the electrons in the solution will move into the semiconductor and a depletion region forms on the interface of the semiconductor. When the light shines onto the p-type

semiconductor, the electrons will jump to the conduction band and move into the solution and

holes will move to the opposite direction, and then a negative current will be generated.
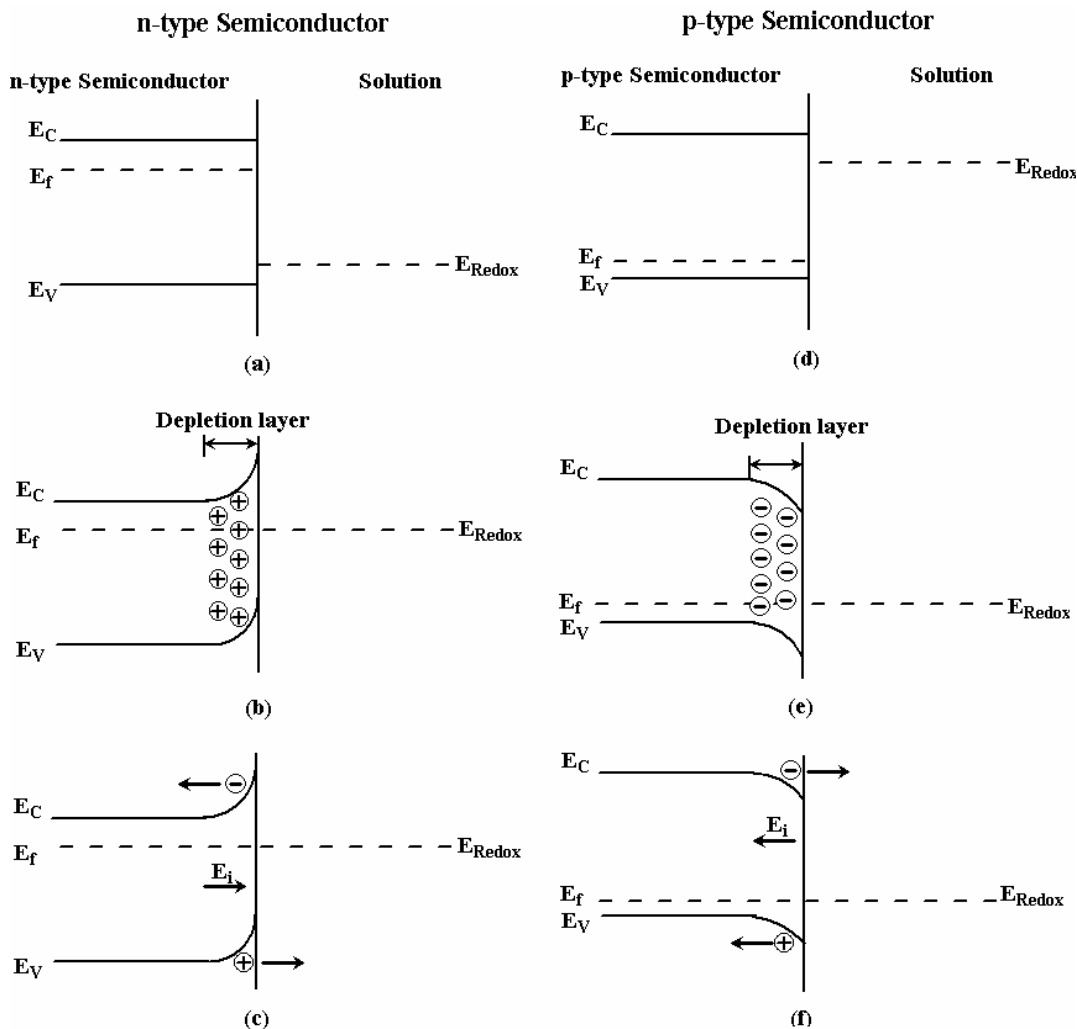
Figure 3.4 Schematic of the mechanism of the photocurrent measurement.(a)(b)(c) n-type semiconductor contacts with solution, (d)(e)(f) p-type semiconductor contacts with solution;(a)(d) before contact, (b)(e) after contact, (c)(f) under light irradiation

Photocurrent from a Cl-doped Cu_2O sample deposited with 0.1 M $CuCl_2$ is shown in

Figure 3.5 and the photocurrent from a Cl-doped Cu_2O sample deposited with 0.3 M $CuCl_2$ is

shown in Figure 3.6. The anodic current indicates an n-type semiconductor [18]. During the

measurement, the applied potential is 0 V vs. the Ag/AgCl reference electrode in Figure 3.5.

35

The solution contains 0.5 M Na_2SO_4. A 90-W white lamp is used as the light source, with the light chopped on and off by a rotating disk. To further confirm the n-type conduction of the Cl-doped Cu_2O samples, the photocurrent-potential characterization is performed between -0.6 and 0.1 V (Figure 3.6). At about -0.3 V, there is a direction change in photocurrent from negative (cathodic) to positive (anodic). Figure 3.7 shows the photocurrent-potential characterization from p-type Cu_2O between -0.6 and 0.1 V. The photocurrent is always negative (cathodic) [70]. The other conditions of n-type Cl doped samples' preparation were temperature 60 °C, 4M $NaC_3H_5O_3$ and pH 7.5. The conditions of p-type sample were temperature 60 °C, 0.3M $CuSO_4$, 4M $NaC_3H_5O_3$ and pH 11.
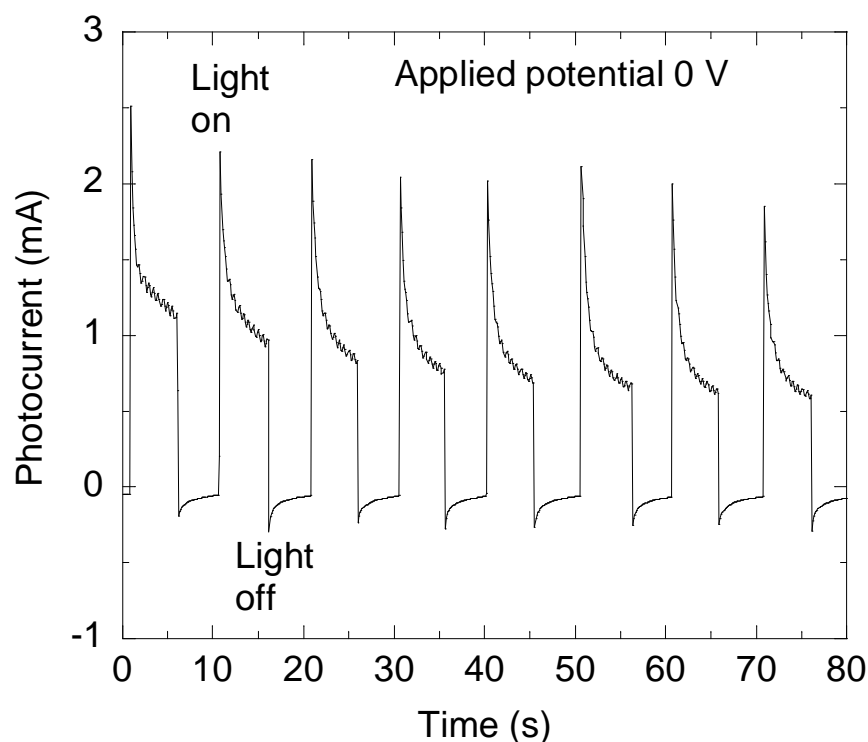
Figure 3.5 Photocurrent vs. time at fixed potential measurements from Cl-doped Cu_2O. Sample was deposited in 0.1 M $CuCl_2$ and 4 M $NaC_3H_5O_3$ solution at 60 °C with pH 7.5.
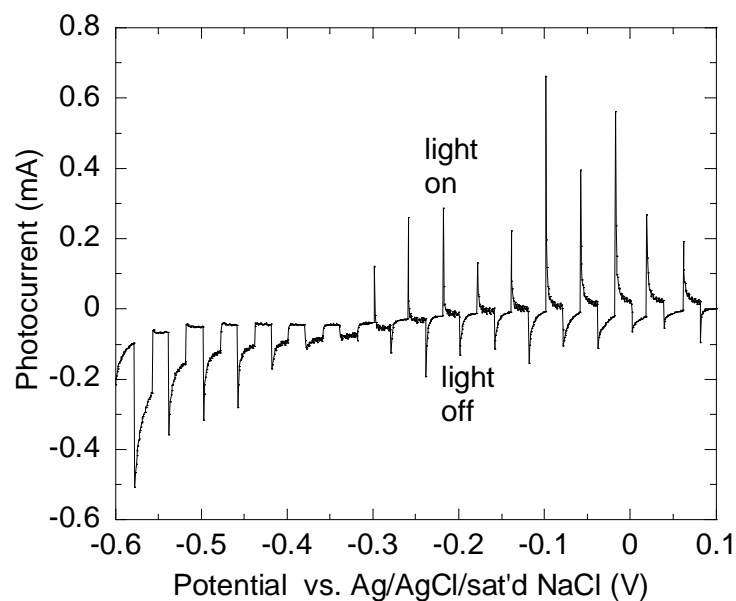
Figure 3.6 Photocurrent vs. potential measurements from Cl-doped Cu_2O. Sample was deposited in 0.3 M $CuCl_2$ and 4 M $NaC_3H_5O_3$ solution at 60 °C with pH 7.5. The anodic current above -0.3 V indicates an n-type semiconductor.
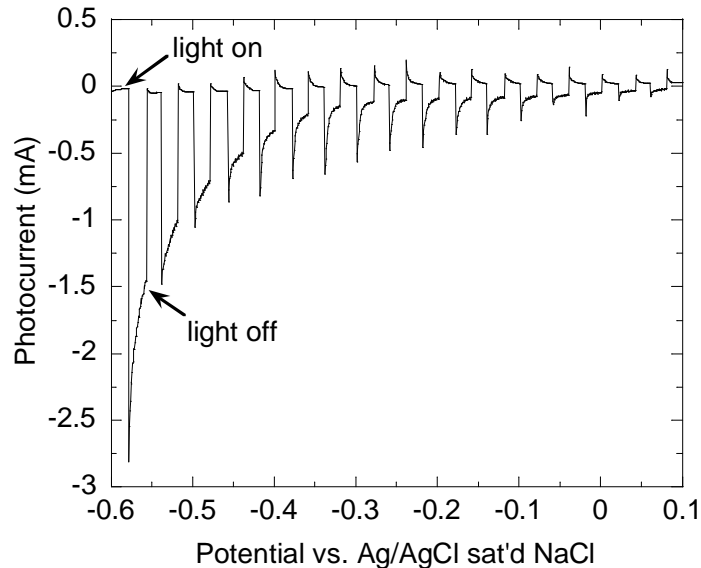
Figure 3.7 Photocurrent vs. potential measurements undoped Cu_2O. The undoped p-type Cu_2O was deposited in 0.3 M $CuSO_4$ and 4 M $NaC_3H_5O_3$ solution at 60 °C with pH 11. The cathodic current in the entire voltage range indicates a p-type semiconductor.

37
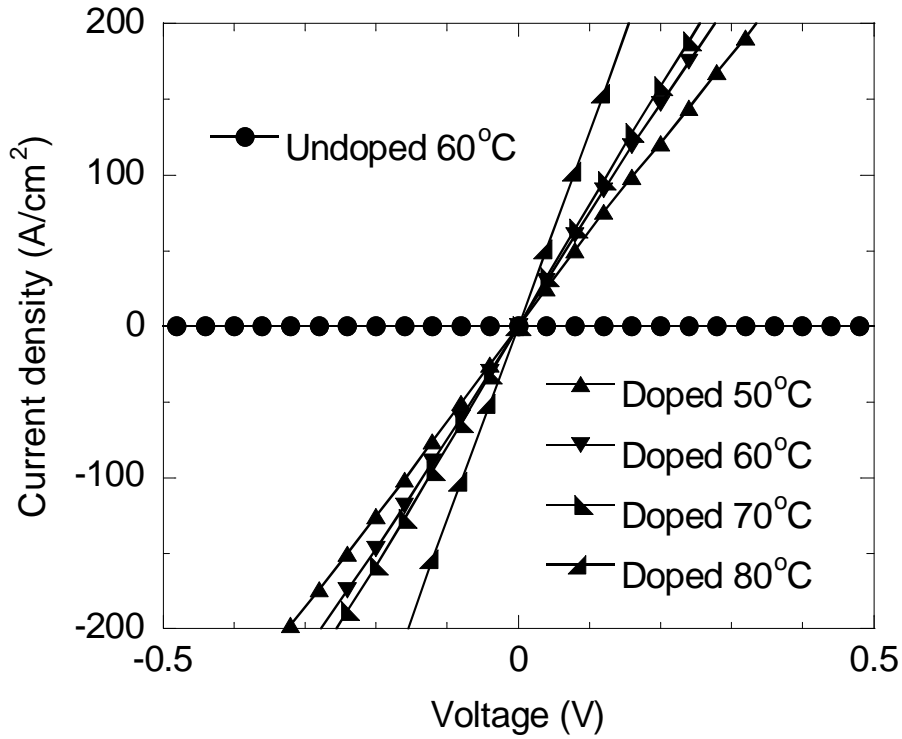
Figure 3.8 Current-voltage relations of undoped and Cl-doped Cu$_2$O deposited at solution temperatures of 50, 60, 70, and 80 °C. The Cl-doped Cu$_2$O deposition solution contains 0.1 M CuCl$_2$, 0.3 M CuSO$_4$, 4 M NaC$_3$H$_5$O$_3$ and solution pH is 7.5. The undoped Cu$_2$O samples were deposited in 0.3 M CuSO$_4$ and 4 M NaC$_3$H$_5$O$_3$ with solution pH 7.5 at 60 °C.

Figure 3.8 compares the I-V relations of Cl-doped Cu$_2$O with that of undoped Cu$_2$O. The deposition solution contains 0.1 M CuCl$_2$ and the solution pH is 7.5. The undoped sample is deposited at 60 °C, while the Cl-doped samples are deposited at 50, 60, 70, and 80 °C. Since these samples have similar thickness, it is obvious from the slopes of the I-V relations that the resistivity of Cl-doped Cu$_2$O is much lower than that of undoped Cu$_2$O. The I-V relations are linear, so their resistances can be extracted. With increasing temperature, the slope of the I-V relations becomes steeper. This indicates that the resistivity of Cl-doped Cu$_2$O decreases with temperature.

The resistivity of undoped and Cl-doped Cu_2O samples as a function of $CuCl_2$ concentration in the solution is shown in Figure 3.9. Without doping, the resistivity of electrochemically-deposited Cu_2O is ~40 MΩ-cm, which is too high to produce an efficient solar cell. However, with 0.1 M $CuCl_2$ in the solution, the resistivity of the Cu_2O sample is significantly reduced to ~75 Ω-cm, an over five-orders-of-magnitude reduction in Cu_2O resistivity.
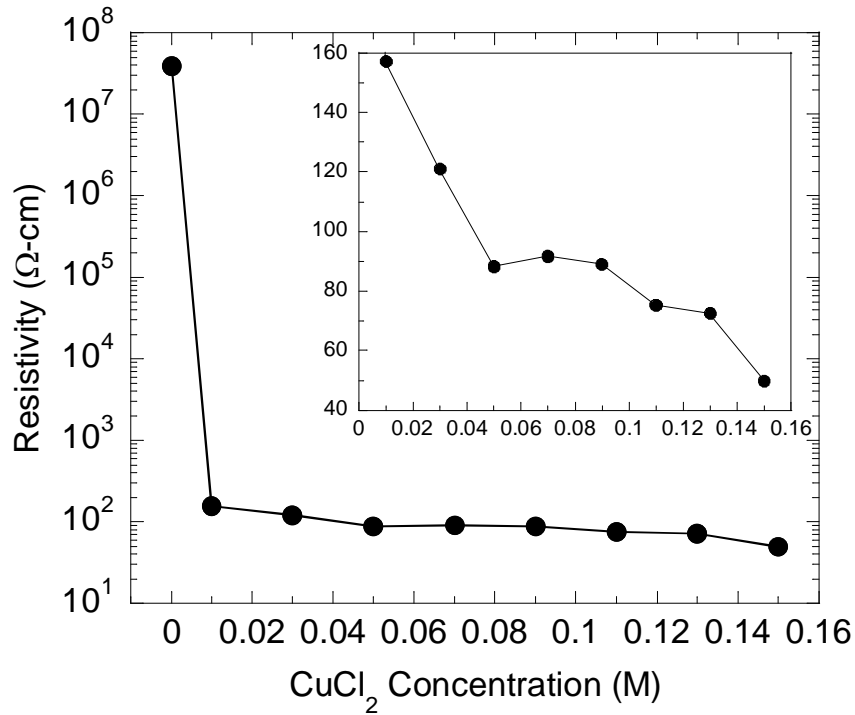
Figure 3.9 Resistivity of undoped and Cl-doped Cu_2O as a function of $CuCl_2$ concentration in the solution. This is a logarithmic plot and the insert is a linear plot. Without doping, the resistivity of Cu_2O is ~40 MΩ-cm, while that of Cl-doped Cu_2O is reduced to between 157 Ω-cm and 48 Ω-cm. The solution temperature is 60 °C and $CuCl_2$ concentration 0.1 M.

The most important parameter to control the resistivity of Cl-doped Cu_2O is the concentration of $CuCl_2$ in the solution: the higher the concentration, the more Cl incorporated into Cu_2O and the lower the resistivity of the sample. In other words, by adjusting the Cl concentration in the solution, the resistivity of the Cu_2O film can be controlled. The insert in Figure 3.9 shows the resistivity of Cl-doped Cu_2O samples as a function of $CuCl_2$ concentration

in the solution. As expected, a higher Cl concentration reduces the resistivity of Cu_2O. Between 0.01 and 0.15 M of $CuCl_2$, the resistivity of Cu_2O is reduced from ~157 Ω-cm to ~48 Ω-cm.
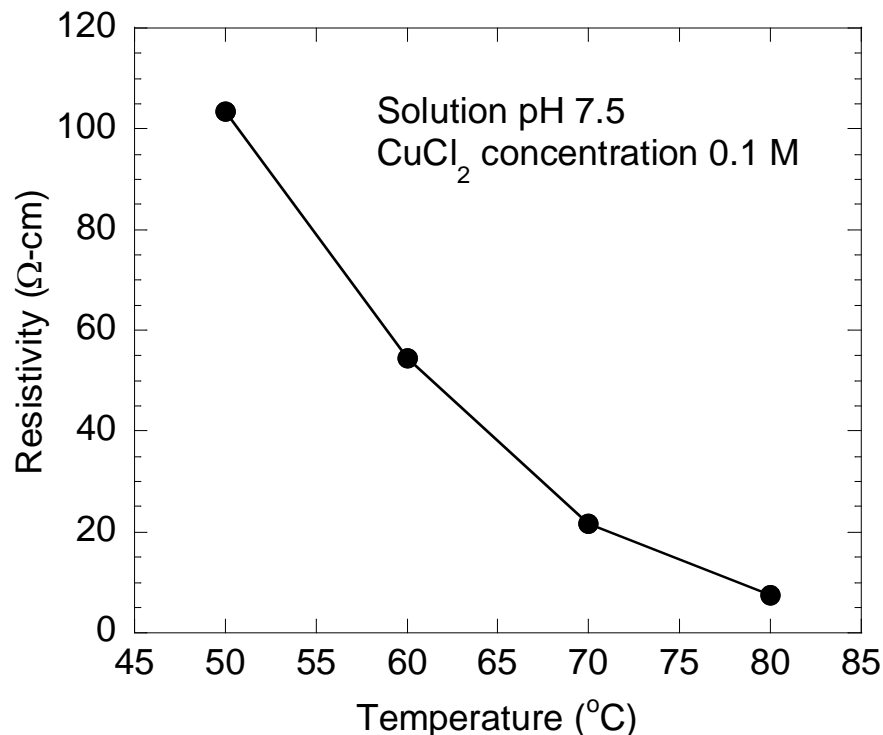
Figure 3.10 Resistivity of Cl-doped Cu_2O as a function of solution temperature. Between 50 and 80 °C, the resistivity of Cl-doped Cu_2O is reduced from 103 Ω-cm to 7 Ω-cm. The $CuCl_2$ concentration 0.1 M.

Solution temperature affects primarily the growth rate and grain size of the polycrystalline Cu_2O film. As the temperature increases, the growth rate and grain size increase. Large grains can improve the electrical properties of the Cu_2O film, such as carrier mobility and minority carrier lifetime. In an aqueous solution, evaporation occurs when the temperature is close to 100 °C, which changes the solution concentration and pH. The effect of solution temperature on Cu_2O resistivity was investigated with a fixed $CuCl_2$ concentration of 0.1 M. Figure 3.10 shows the resistivity of Cl-doped Cu_2O as a function of solution temperature. Between 50 and 80 °C, the resistivity is reduced from ~103 Ω-cm to ~7 Ω-cm. The latter is very

close to the optimum resistivity for an efficient solar cell, ~1 Ω-cm. Efforts are underway to bring down the resistivity of Cl-doped Cu_2O to below 1 Ω-cm.

The decrease in resistivity with temperature may be attributed to increased Cl incorporation into Cu_2O at higher temperatures. It is speculated that Cl incorporation creates a concentration gradient for Cl^- ions in the deposition solution. However, the diffusion coefficient of typical ions in a solution increases by 2–3%/°C around 25 °C [71], which reduces the concentration gradient for Cl^- ions and increases Cl incorporation into Cu_2O. Temperature has effects on the resistivity of Cu_2O, but it is not the main reason. In principle, Cl is the n-type dopant and only it will largely affect the resistivity of Cu_2O

Figure 3.11 shows the resistivity of Cl-doped Cu_2O as a function of $CuSO_4$ concentration in the solution, which serves as the Cu precursor. The solution temperature is 60 °C, solution pH 7.5, and $CuCl_2$ and $NaC_3H_5O_3$ concentrations 0.15 M and 4 M, respectively. During deposition, -0.1 V is applied on the cathode as deposition potential.
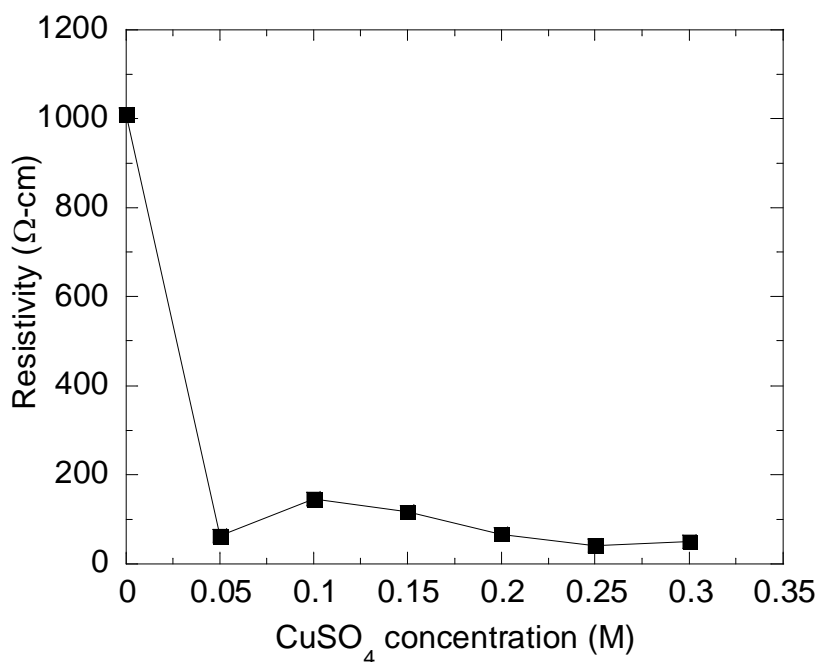
Figure 3.11 Resistivity of Cl-doped Cu_2O films prepared at 60 °C and with 0.15 M $CuCl_2$ as a function of $CuSO_4$ concentration.

As shown in the Figure 3.11, the resistivity of the film is 1 kΩ-cm without $CuSO_4$. In this case, $CuCl_2$ serves as both the Cu and Cl precursor. With 0.3 M $CuSO_4$ in the solution, the resistivity of the film is reduced to 54 Ω-cm. It seems that more Cu leads to lower resistivity, but Cu is not a dopant. When $CuSO_4$ concentration is above 0.05 M, the resistivity of the films does not change much.
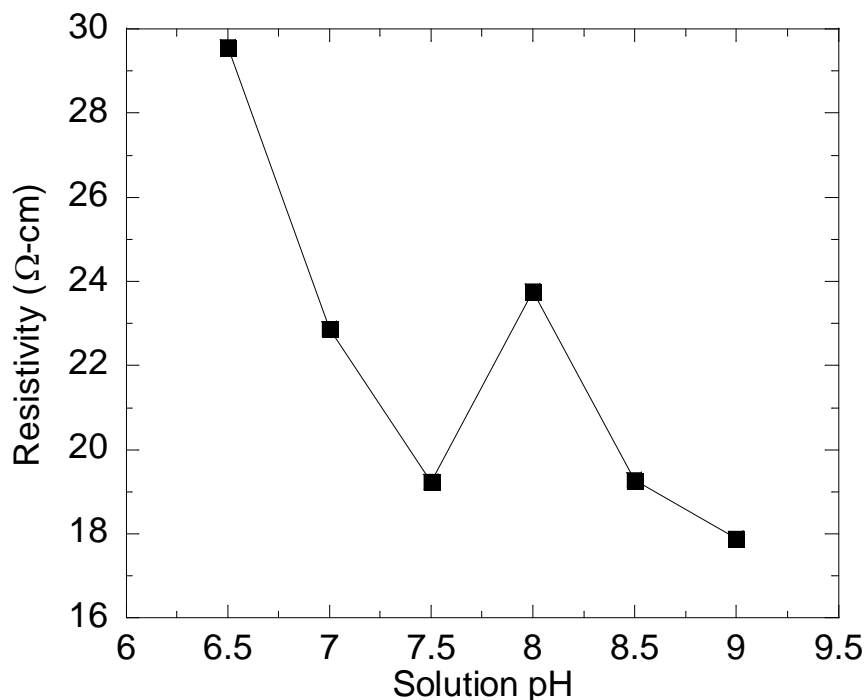
Figure 3.12 Resistivity of Cl-doped Cu_2O films prepared at 60 °C and with 0.15 M $CuCl_2$ as a function of pH.

Figure 3.12 shows the resistivity of Cl-doped Cu_2O as a function of solution pH. The deposition conditions are: 0.15 M $CuCl_2$, 4 M $NaC_3H_5O_3$, 0.3 M $CuSO_4$, -0.1 V depositing potential, and 60 °C deposition temperature. Between pH 6.5 and 9.0, the resistivity decreases only slightly, from 29.6 Ω-cm to 17.8 Ω-cm. The data point at pH 8 seems out of trend. This could be due to experimental errors such as fluctuations in film thickness or surface roughness. When solution pH is above 9.5, the Cu_2O film becomes p-type by photocurrent characterization.
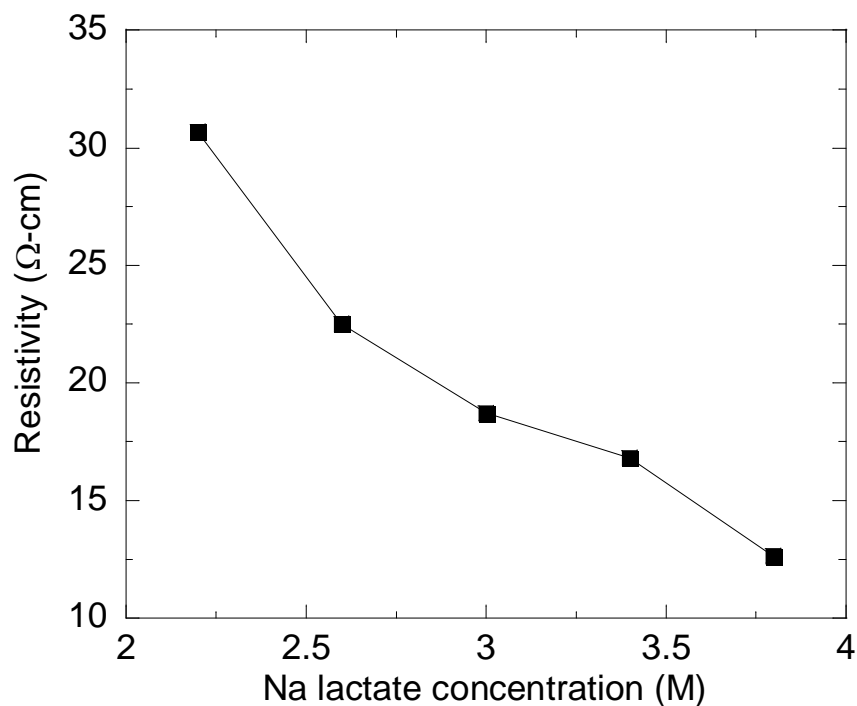
Figure 3.13 Resistivity of Cl-doped Cu_2O films prepared at 60 °C and with 0.15 M $CuCl_2$ as a function of $NaC_3H_5O_3$ concentration.

The concentration of complex agent also has some effect on the resistivity. Figure 3.13 shows the resistivity of Cl-doped Cu_2O as a function of $NaC_3H_5O_3$ concentration. In the deposition solution, the $CuCl_2$ concentration is 0.15 M, $CuSO_4$ concentration 0.3 M, solution pH 7.5, solution temperature 60 °C, and deposition potential -0.1 V. The figure reveals that the resistivity of the film decreases slightly with increasing $NaC_3H_5O_3$ concentration between 2.2 M and 3.8 M, from 30.7 Ω-cm to 12.6 Ω-cm. This may be attributed to more stable Cu^{2+} ions with more $NaC_3H_5O_3$.

$CuCl_2$ can serve as both the Cu precursor and the Cl precursor, as demonstrated in Figure 3.11 with zero $CuSO_4$ concentration. For this reason, the effect of $CuCl_2$ concentration on the resistivity of Cu_2O was investigated, without $CuSO_4$. The downside of this approach is that there is no independent control of Cl concentration in the solution to control the Cl doping

level in the film. Figure 3.14 shows the resistivity of Cl-doped Cu_2O as a function of $CuCl_2$ concentration in the solution. The solution pH is 7.5, solution temperature 60 °C, and deposition potential on the cathode -0.1 V. It is noticed that the resistivity decreases while the $CuCl_2$ concentration increases. Different $CuCl_2$ concentrations result in different Cl concentrations in the solution. It is clear that a higher Cl concentration leads to a lower resistivity. With 0.4 M $CuCl_2$, the resistivity of the film is 16.3 Ω-cm.
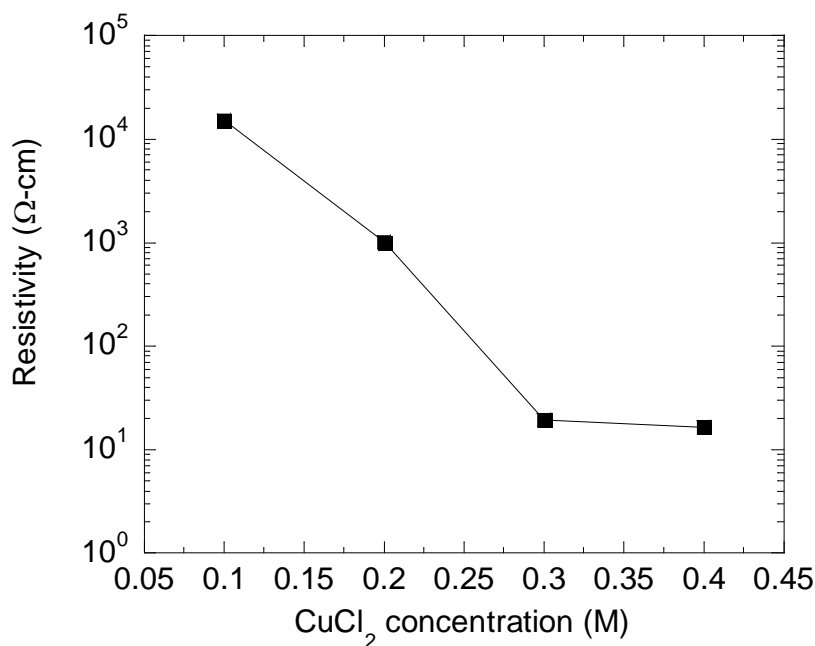
Figure 3.14 Resistivity of Cl-doped Cu_2O as a function of $CuCl_2$ concentration. Here $CuCl_2$ serves as both the Cu and Cl precursor, without $CuSO_4$. The solution pH is 7.5 and solution temperature is 60 °C.

In order to achieve lower resistivity, a higher Cl concentration is obviously necessary. With $CuCl_2$ as the only precursor, the Cl/Cu ratio is fixed. In addition, it is found that high $CuCl_2$ concentrations require more complex agent for stabilization of Cu^{2+} ions. For these reasons, NaCl was added into the $CuCl_2$ solution to adjust the Cl/Cu ratio and thus the Cl concentration independently. The problem is that the Cu film coated on the substrate dissolves in the high Cl concentration solution.

3.4 Structure Properties of Cl-Doped Cu$_2$O

3.4.1 *XRD Measurement of Cu$_2$O*

(a)

(b)
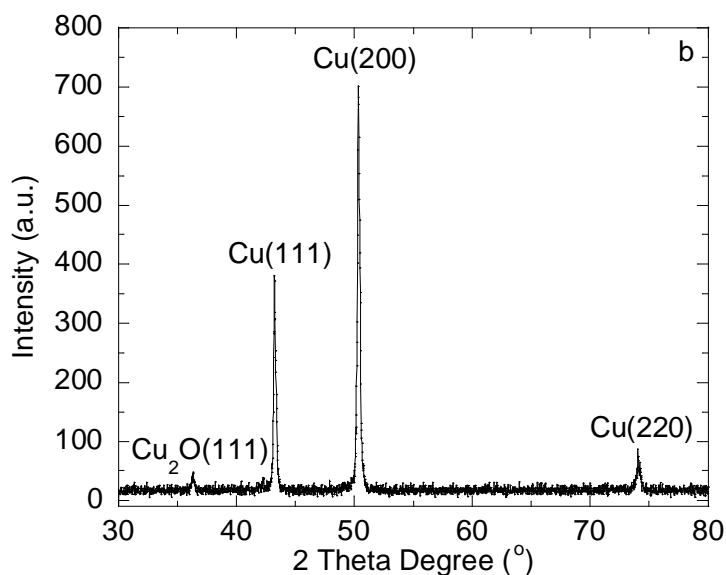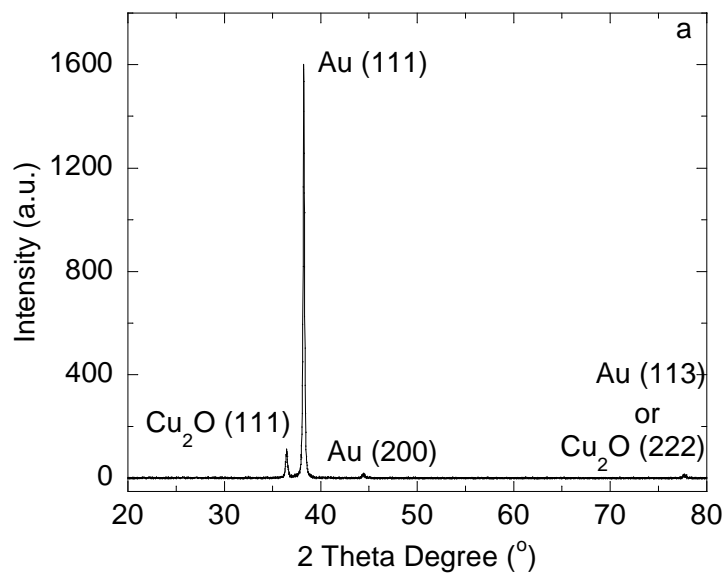
Figure 3.15 XRD patterns of Cl-doped Cu$_2$O on (a) Au-coated glass substrate and (b) Cu-coated glass substrate. The deposition solution contains 0.1 M CuCl$_2$, 0.3 M CuSO$_4$, and 4 M NaC$_3$H$_5$O$_3$. The solution pH is 7.5 and deposition temperature is 60°C. Only Cu$_2$O is observed on the Au-coated glass substrate.

Figure 3.15(a) shows the XRD pattern of Cl-doped Cu_2O on a Au-coated glass substrate. The sample was deposited with 0.1 M $CuCl_2$, 0.3 M $CuSO_4$, and 4 M $NaC_3H_5O_3$ at 60 °C. The thickness of this film is ~700 nm, twice as thick as other samples reported in this paper. Although the (111) peak from Cu_2O is still weak as compared to the Au(111) peak, it is clear from XRD that Cu_2O is the only phase present in the film. A peak at 77.8° may due to the Au (113) or Cu_2O (222). Figure 3.15(b) shows the XRD pattern of Cl-doped Cu_2O on a Cu-coated glass substrate. XRD reveals only one weak Cu_2O peak, (111) at 36.2° and the rest are Cu peaks. The weak Cu_2O peak is attributed to the thin Cu_2O film, ~300 nm. Since the 77.8° peak is not very clear in Figure 3.15(b), probably the 77.8° peak is Au (113) not Cu_2O (222) in Figure 3.15(a). The XRD results were compared with standard XRD database (JCPDF: #04-0836, 65-2870 and 65-3288).

3.4.2 *Surface Morphology of Cu_2O*
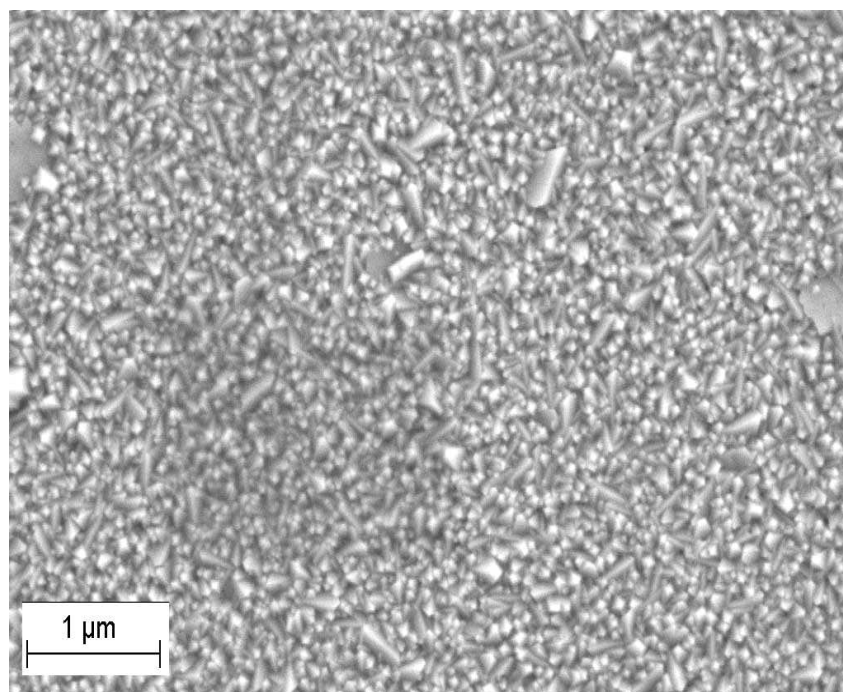
Figure 3.16 Scanning electron microscopy image of Cl-doped Cu_2O deposited with 0.1 M $CuCl_2$, 0.3 M $CuSO_4$, 4 M $NaC_3H_5O_3$, solution pH 7.5, and solution temperature 60 °C.

Figure 3.16 shows a SEM image of Cl-doped n-type Cu_2O electrodeposited with 0.1 M $CuCl_2$, 0.3 M $CuSO_4$, 4 M $NaC_3H_5O_3$, solution pH 7.5, deposition potential -0.1 V, and deposition temperature 60 °C. It reveals a continuous film with a grain size of ~100 nm. This grain size is smaller than the typical grain size of electrodeposited Cu_2O, which is on the order of μm [72]. Therefore, one direction for future research is to improve the grain size of Cl-doped n-type Cu_2O.

3.5 Summary

A study on the effects of doping conditions on electrical properties of Cl-doped Cu_2O by electrodeposition is presented. The resistivity of Cl-doped Cu_2O is affected by doping conditions, including Cu and Cl concentrations, different Cu and Cl precursors, complex agent concentration, solution pH, and deposition temperature. The lowest resistivity obtained so far is 7 Ω-cm, suitable for solar cell applications. Photocurrent-potential measurements verify the n-type conductivity of Cl-doped Cu_2O. SEM indicates a small grain size of ~100 nm in Cl-doped Cu_2O. XRD confirms the films as pure Cu_2O. This n-type doping method enables much more efficient Cu_2O solar cells and is particularly suitable for low-cost, large-area, and high-throughput fabrication of solar cells.

CHAPTER 4

ELECTRODEPOSITION AND CHARACTERIZATION OF GROUP IIIA DOPED ZnO

4.1 Introduction

A transparent conductive oxide (TCO) film with a large band gap and low resistance is used in thin-film solar cells to serve as the window and electrode [73-75]. Indium tin oxide (ITO), with less than 10% Sn, is the best TCO in terms of resistivity. However, In is rare in the nature and using a vacuum process such as sputtering to deposit ITO is relatively costly [76]. Another TCO, zinc oxide is of great interest because of several advantages. First, compared to ITO, ZnO is much cheaper because Zn is abundant in the nature. Second, ZnO is n-type and has a hexagonal wurtzite structure with a wide direct band gap of 3.3 eV [77]. The large band gap of ZnO perfectly matches the requirement for TCOs as a window in solar cells. In addition, ZnO can be eletrodeposited with low cost and at low temperatures compared to vacuum deposition [78]. However, the resistivity of undoped ZnO is usually up to the kΩ-cm range by several preparation methods, which is too high to be used as a TCO in photovoltaic devices [79]. In order to reduce the resistivity of ZnO into the range of low 10^{-4} Ω-cm as achieved in ITO, doping is required. Substitutional n-type doping in ZnO can go into either Zn or O sites. Since Zn is a group II element and O is a group VI element, group III elements can be n-type dopants for Zn sites and group VII elements can be n-type dopants for O sites. Out of all the group VII halogens, fluorine is best size-matched to O, so F has been reported as a successful n-type dopant in ZnO [62].

Aluminum and gallium are group IIIA elements which are commonly-used n-type cation dopants in ZnO. Recently, Al-doped ZnO by electrodeposition was demonstrated, but the resistivity of Al-doped ZnO was still in the kΩ-cm range which is too high to be used as a TCO [80]. In this chapter, Al and Ga doping in ZnO during electrodeposition of ZnO thin films is

48

discussed. The minimum resistivity achieved so far is 3.8×10^{-4} Ω-cm. By reducing the resistivity of ZnO into the low 10^{-4} Ω-cm range with a solution-based method, the major roadblocks for ZnO to be a low-cost low-resistance TCO for its applications in solar cells is removed.

4.2 Experiment

4.2.1 *Sample Preparation*

Electrochemical experiments were carried out using a Princeton Applied Research VERSTAT II potentiostat and performed in a three-electrode cell with a platinum counter electrode, a silver/silver chloride/saturated sodium chloride reference electrode, and an ITO-coated glass substrate as the working electrode. The ITO film had a typical sheet resistance of 30~40 Ω/square with a typical dimension of 1×4 cm^2. ITO film was deposited on glass substrate by AJA ATC ORION Series UHV Sputtering System. During deposition, vacuum was maintained at 7 mTorr, the RF power was 100 W and the deposition time was 40 minutes. The thickness of the ITO film was ~150 nm. Prior to electrodeposition, the ITO substrate was rinsed with acetone and then sonicated in distilled water for ~15 minutes. The deposition solution contained 0.1 M zinc nitrate ($Zn(NO_3)_2$). The Al or Ga precursor was $Al(NO_3)_3$ or $Ga(NO_3)_3$ with various mole concentrations. The as-prepared solution had a pH between 4 and 6. The deposition temperature was controlled by a Precision 280 water bath to 70 ºC. All the chemicals used were reagent grade.

4.2.2 *Sample Characterization*

The thickness of the Al or Ga-doped ZnO films was measured with a KLA-Tencor Alpha-Step IQ profilometer. The sheet resistance of the Al or Ga-doped ZnO films on ITO substrate was determined by Jandel Four-point Probe System with RM3 Test Unit, and the resistivity of Al or Ga-doped ZnO was calculated assuming the ZnO/ITO stack as a parallel circuit. JASCO V-570 UV-vis spectrophotometer was used to measure the total transmittance and reflectance of the Al or Ga-doped ZnO films. The absorbance of the Al or Ga-doped ZnO films was calculated from the transmittance and reflectance with the following relation: A = 1 - R

- T. Energy dispersion spectrum (EDS) measurements were performed to determine the Al or Ga atomic concentrations in the ZnO films. The structural properties of the Al or Ga-doped ZnO films were determined by Simens D-500 x-ray diffraction (XRD) using the copper Kα line.

4.2.3 *Doping Mechanism*
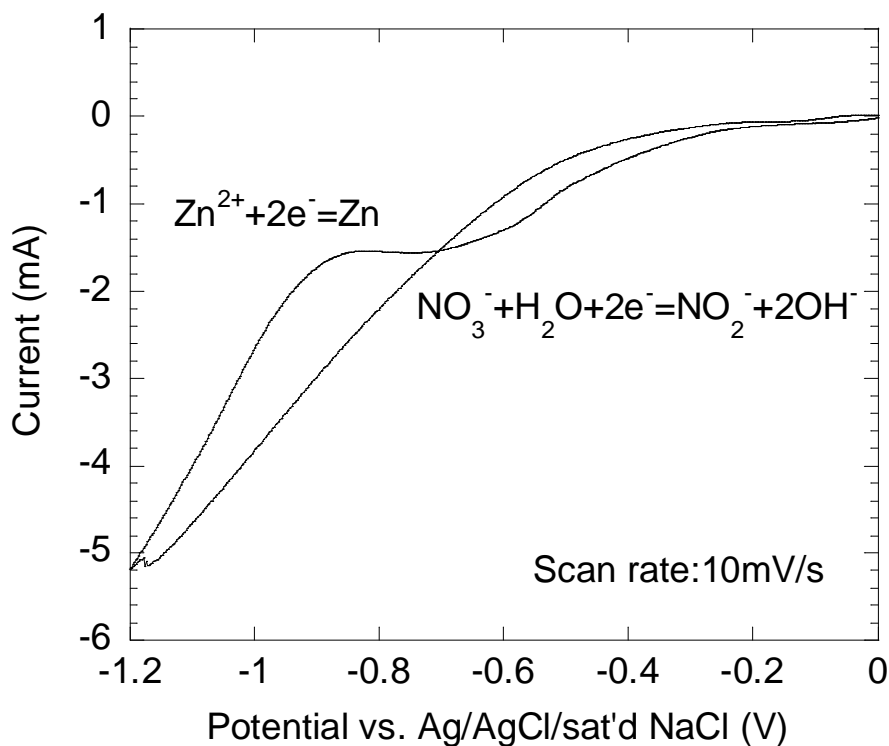
Figure 4.1 Cyclic voltammetry of a deposition solution containing 0.1 M $Zn(NO_3)_2$ and 0.02 mM $Al(NO_3)_3$. The solution temperature is 70°C and as-prepared solution pH 5. There are two reduction reactions, which lead to (1) OH⁻ ions and (2) metallic Zn. The reduction potential for OH⁻ ions is between -0.5 and -0.8 V.

Electrodeposition of ZnO was performed potentiostatically. The deposition solution contained 0.1 M $Zn(NO_3)_2$ and different $Al(NO_3)_3$ concentrations varying from 0.02 mM to 4 mM. $Al(NO_3)_3$ and $Zn(NO_3)_2$ not only worked as the Al and Zn precursor but also an OH⁻ precursor. Before deposition, cyclic voltammetry was performed in a solution containing 0.1 M $Zn(NO_3)_3$ and 0.02 mM $Al(NO_3)_3$ at 70 °C, which revealed two reduction reactions (Figure 4.1):

$$NO_3^- + H_2O + 2e^- \rightarrow NO_2^- + 2OH^- \tag{R1}$$

$$Zn^{2+} + 2e^- \rightarrow Zn \tag{R2}$$
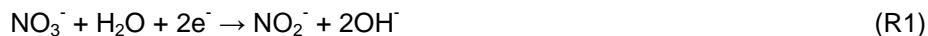
The potential for reaction R1 is between -0.5 and -0.8 V vs. the Ag/AgCl reference electrode (Figure 4.1). In this study, -0.6 V was chosen as the deposition potential applied to the working electrode. The produced OH^- ions react with Zn^{2+} ions in the solution to form ZnO:

$$Zn^{2+} + 2OH^- \rightarrow ZnO\downarrow + H_2O \tag{R3}$$

With the presence of Al^{3+} ions in the solution, OH^- ions also react with Al^{3+} ions to form Al_2O_3, which incorporates Al into ZnO and thus dopes the ZnO film:

$$2Al^{3+} + 6OH^- \rightarrow Al_2O_3\downarrow + 3H_2O \tag{R4}$$

Figure 4.2 shows the cyclic voltammetry measured in a deposition solution containing 0.1 M $Zn(NO_3)_2$ and 0.02 mM $Ga(NO_3)_3$. The solution temperature was 70 °C and the as-prepared solution had a pH of 5.5. Three reduction reactions are revealed in Figure 4.2:

$$NO_3^- + H_2O + 2e^- \rightarrow NO_2^- + 2OH^- \tag{R5}$$

$$Ga^{2+} + 2e^- \rightarrow Ga \tag{R6}$$

$$Zn^{2+} + 2e^- \rightarrow Zn \tag{R7}$$
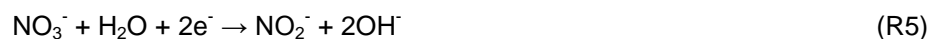
The potential for reaction R5 is between -0.2 and -0.45 V vs. the Ag/AgCl reference electrode, which is more positive than the potential for depositing Al-doped ZnO. Here, -0.3 V was chosen as the deposition potential applied to the working electrode. The produced OH^- ions react with Zn^{2+} ions in the solution to form ZnO (reaction R3). With the presence of Ga^{3+} ions in the solution, OH^- ions also react with Ga^{3+} ions to form Ga_2O_3, which incorporates Ga into ZnO, and thus dopes the ZnO film:

$$2Ga^{3+} + 6OH^- \rightarrow Ga_2O_3\downarrow + 3H_2O \tag{R8}$$

Therefore, the mechanism for depositing Ga-doped ZnO is quite similar to that for depositing Al-doped ZnO. However, the uniformity of Ga-doped ZnO is much better than that of Al-doped ZnO, presumably due to the larger and heavier Ga atoms over Al atoms.
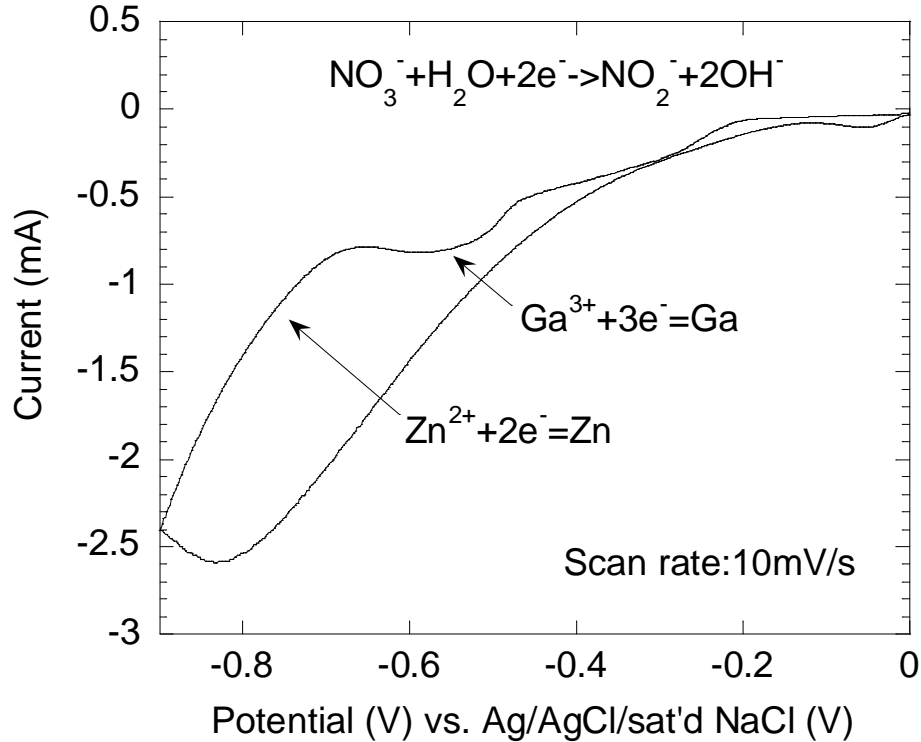
Figure 4.2 Cyclic voltammetry of a deposition solution containing 0.1 M $Zn(NO_3)_2$ and 0.02 mM $Ga(NO_3)_3$. The solution temperature was 70 °C and the as-prepared solution had a pH of 5.5. There are three reduction reactions on the electrode, which lead to (1) OH^- ions, (2) metallic Ga, and (3) metallic Zn. The reduction potential for OH^- ions is between -0.2 and -0.45 V.

<u>4.3 Structure and Electrical Properties of Al-Doped ZnO</u>

Several samples were prepared with different $Al(NO_3)_3$ concentrations in the deposition solution at 70 °C. The thickness of the Al-doped ZnO films was controlled to between 400 and 500 nm, measured with a profilometer. Post-deposition annealing was carried out at 200 °C for 3 hours in air, as the as-deposited films may have contained some zinc hydroxide. Four-point probe was used for measuring the sheet resistance of the Al-doped ZnO films on ITO substrate, i.e. the ZnO/ITO stack structure.

Figure 4.3 shows the measured sheet resistance of Al-doped ZnO on ITO as a function of Al^{3+}/Zn^{2+} ratio in the deposition solution. The sheet resistance of the stack structure initially decreases with increasing Al^{3+}/Zn^{2+} ratio, but then suddenly increases after the Al^{3+}/Zn^{2+} ratio

reaches 0.001. This may be attributed to the formation of Al_2O_3, which is known as a good insulator, in ZnO. The minimum sheet resistance at the Al^{3+}/Zn^{2+} ratio of 0.001 is 13.8 Ω/square. Assuming that the ZnO/ITO stack is a parallel circuit (Figure 4.4), and knowing that the sheet resistance of ITO is 37 Ω/square and the thickness of ITO is 150 nm, the minimum resistivity of the Al-doped ZnO is 8×10^{-4} Ω-cm.

EDS measurements were carried out to determine the Al atomic concentrations in the Al-doped ZnO films. Figure 4.5(a) shows the EDS spectrum of Al doped ZnO with different Al^{3+}/Zn^{2+} in the solution. The Al_{Ka} peak intensity increases with the increasing of Al^{3+} concentration in the solution. Figure 4.5(b) shows the relation between the Al/Zn atomic ratio in the film as a function of the Al^{3+}/Zn^{2+} atomic ratio in the deposition solution. The Al content in the film increases with increasing Al^{3+}/Zn^{2+} ratio in the solution, but in a nonlinear fashion. The Al/Zn atomic ratio corresponding to the minimum sheet resistance of 13.8 Ω/square is ~0.02.
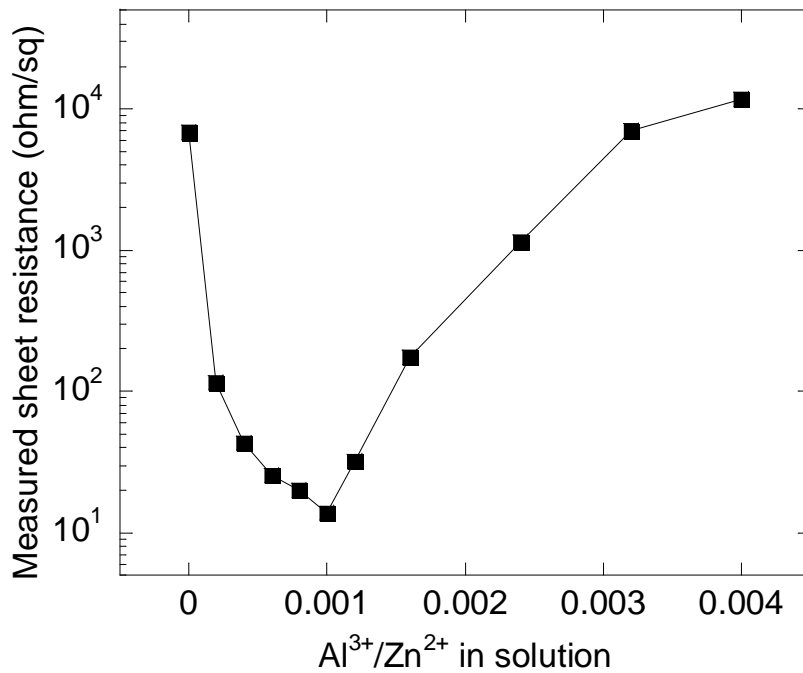
Figure 4.3 Measured sheet resistance of Al-doped ZnO on ITO as a function of the Al^{3+}/Zn^{2+} atomic ratio in the deposition solution. The as-deposited Al-doped ZnO films were annealed in air at 200 °C for 3 hours to eliminate $Zn(OH)_2$.
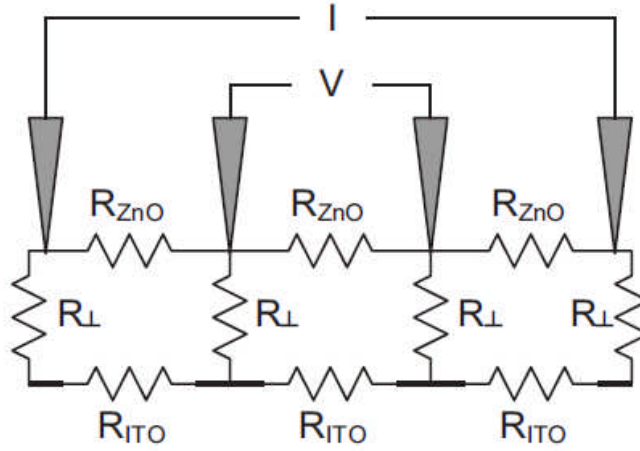
Figure 4.4 Circuit model for extracting the resistivity of Al-doped ZnO from the measured sheet resistance of the Al-doped ZnO on ITO stack by four-point probe. R_{ZnO} is the sheet resistance of Al-doped ZnO between two probes, R_{ITO} is the sheet resistance of ITO between two probes and $R_\perp$ is the vertical resistance due to the thickness of ZnO. Since the probe spacing is much larger than the thickness of ZnO, $R_\perp << R_{ZnO}$. $R_\perp$ can be neglected. The sheet resistance of the stack can be expressed as $1/R_{Stack} = 1/R_{ZnO} + 1/R_{ITO}$. The resistivity can be calculated from the sheet resistance.

Figure 4.6 shows the total transmittance and absorbance of ITO, undoped ZnO on ITO, and Al-doped ZnO on ITO. The absorbance was calculated from the transmittance and reflectance. ITO has the lowest absorbance and highest transmittance, undoped ZnO has the highest absorbance and lowest transmittance, and the transmittance and absorbance of Al-doped ZnO are between those two. The average transmittance of Al-doped ZnO is over 80% and the average absorbance of Al-doped ZnO is below 5%, which meet the requirement for TCOs. The band gap of Al-doped ZnO increases as compared to that of undoped ZnO, as indicated by the absorption edges in Figure 4.6. Since Al_2O_3 has a very large band gap of 6.6 eV, the band gap of Al-doped ZnO may exceeds that of ITO, i.e. ~4 eV. Therefore, the absorption edge for Al-doped ZnO in Figure 4.6 may correspond to the bang gap of ITO.

54
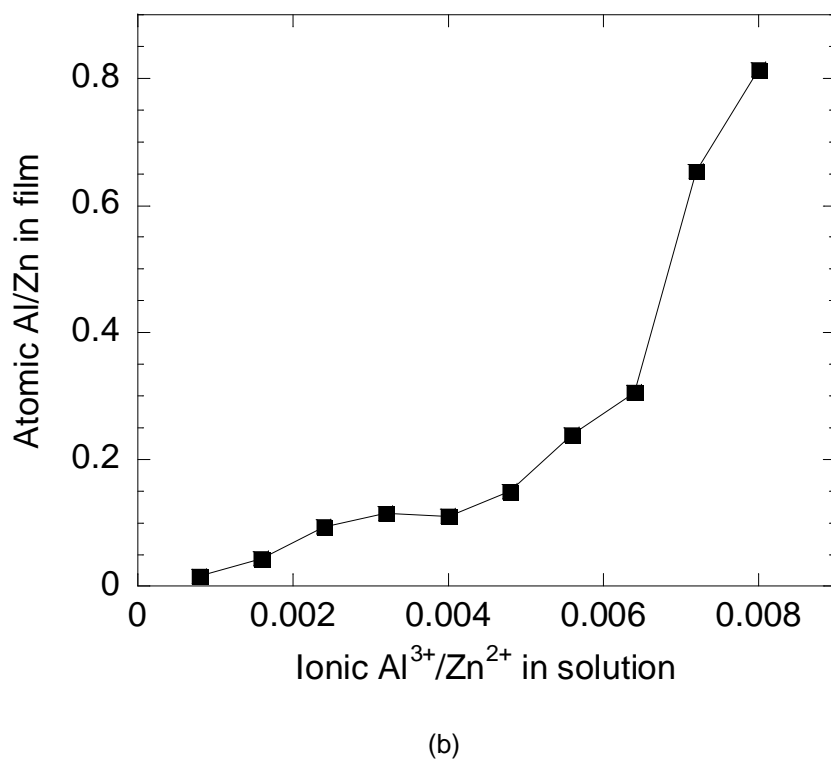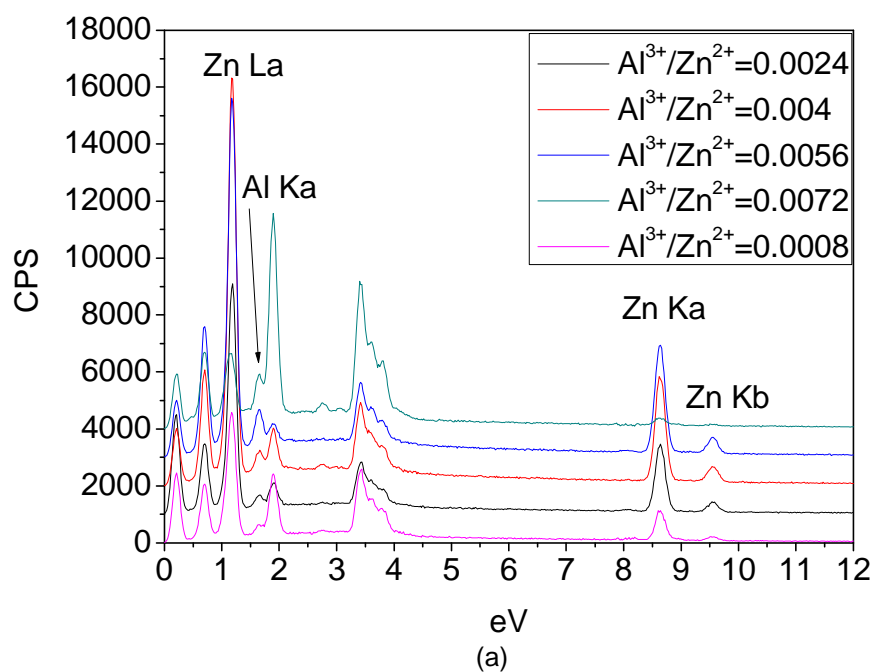
Figure 4.5 (a) EDS spectrum of Al doped ZnO films with different Al3+/Zn2+ in the solution and (b) the Al/Zn atomic ratio in the Al-doped ZnO films as a function of the Al^{3+}/Zn^{2+} atomic ratio in the deposition solution.

However, the concentration uniformity of the Al-doped ZnO samples by electrodeposition is poor. All the sheet resistance and Al concentration data were measured at the center of the samples. In fact, the samples have a large Al concentration gradient across them, resulting in large variations of sheet resistance at different locations. This problem may be caused by the different diffusion velocities of Al^{3+} and Zn^{2+} ions in the deposition solution due to their different ionic radii. This uniformity issue needs to be solved before electrodeposited Al-doped ZnO can be applied to commercial-size solar cells.
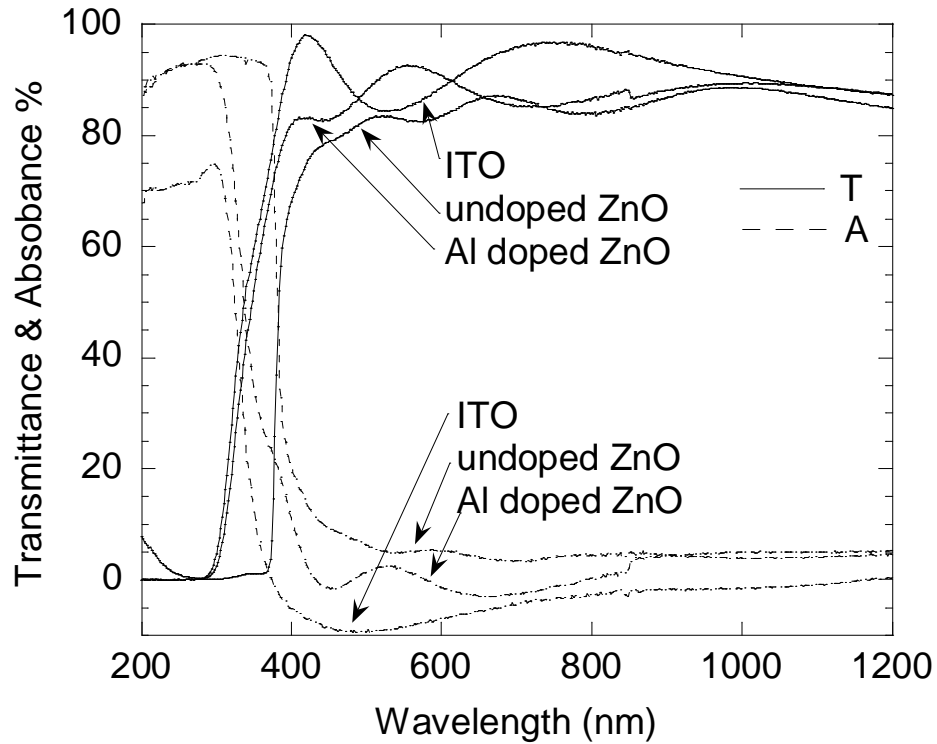
Figure 4.6 Total transmittance and absorbance of ITO, undoped ZnO on ITO, and Al-doped ZnO on ITO. All samples were deposited with an Al^{3+}/Zn^{2+} ratio of 0.001.
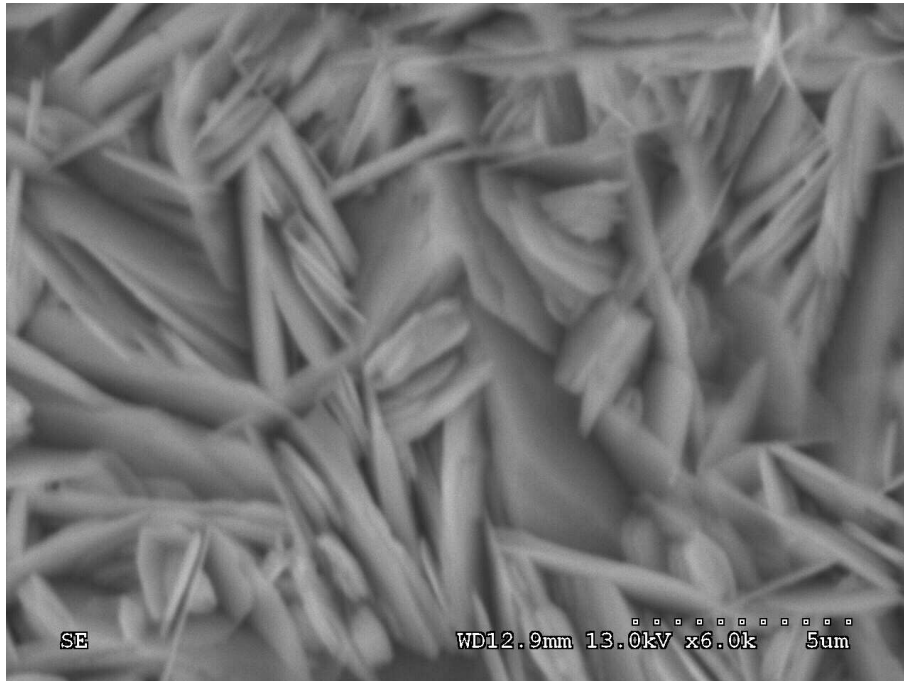
Figure 4.7 The scanning microscope image of Al doped ZnO deposited from Al^{3+}/Zn^{2+}=0.001

Figure 4.7 shows the SEM image of the Al doped ZnO sample. The sample was deposited from ionic ration Al^{3+}/Zn^{2+}=0.001 solution at bath temperature 70 °C and then post-deposition annealed at 200 °C for 3 hours in air. From this SEM image, it can be seen that the grain size of the ZnO is huge (about 1 um) and shape of the ZnO is like sheet. Most ZnO particles overlap together.
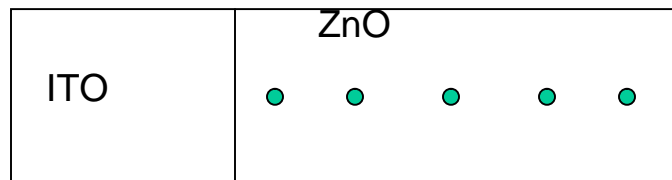
Figure 4.8 Five different locations on the Al doped ZnO thin film for EDS measurement.

The Al doped ZnO has big uniformity problem. Figure 4.8 shows 5 different locations on the Al doped ZnO thin film. The inter spacing between two points is 0.4 cm and points distance starts from the interface of ITO and ZnO.
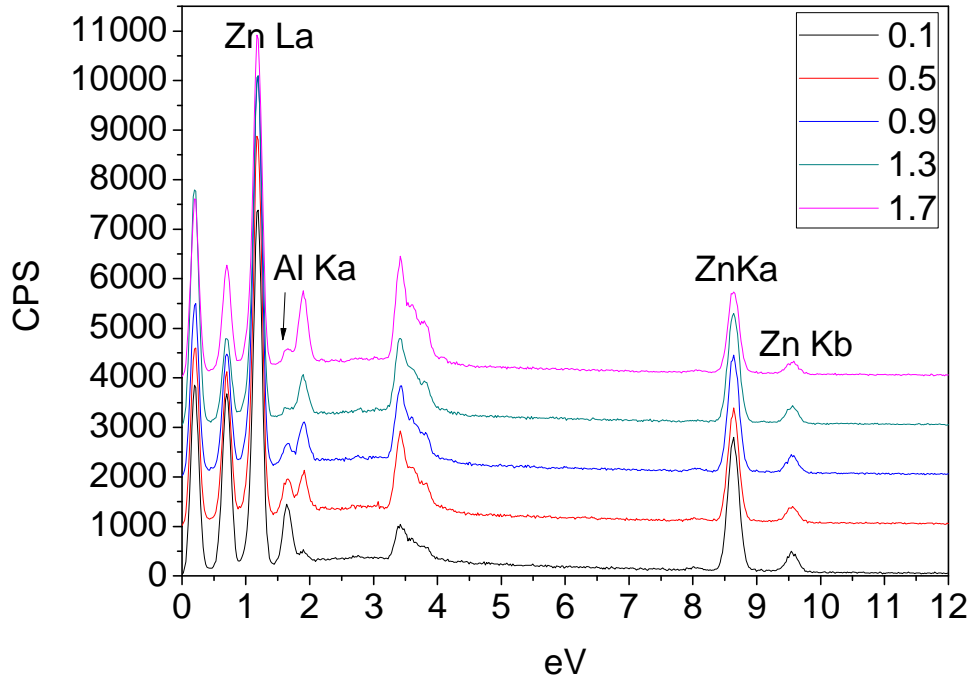
Figure 4.9 EDS spectrum of the five locations of ZnO film.

Figure 4.9 shows the EDS spectrum of the five different locations, while the intensity of Al peak decreases from the location near interface of ITO and ZnO to the edge of the glass co-responding to the positions in the Figure 4.8. A large Al concentration variation trend is shown in Figure 4.10. With such high Al concentration gradient, the electrical and optical properties are non-equal through the whole area which may result in non-reliable device performance.
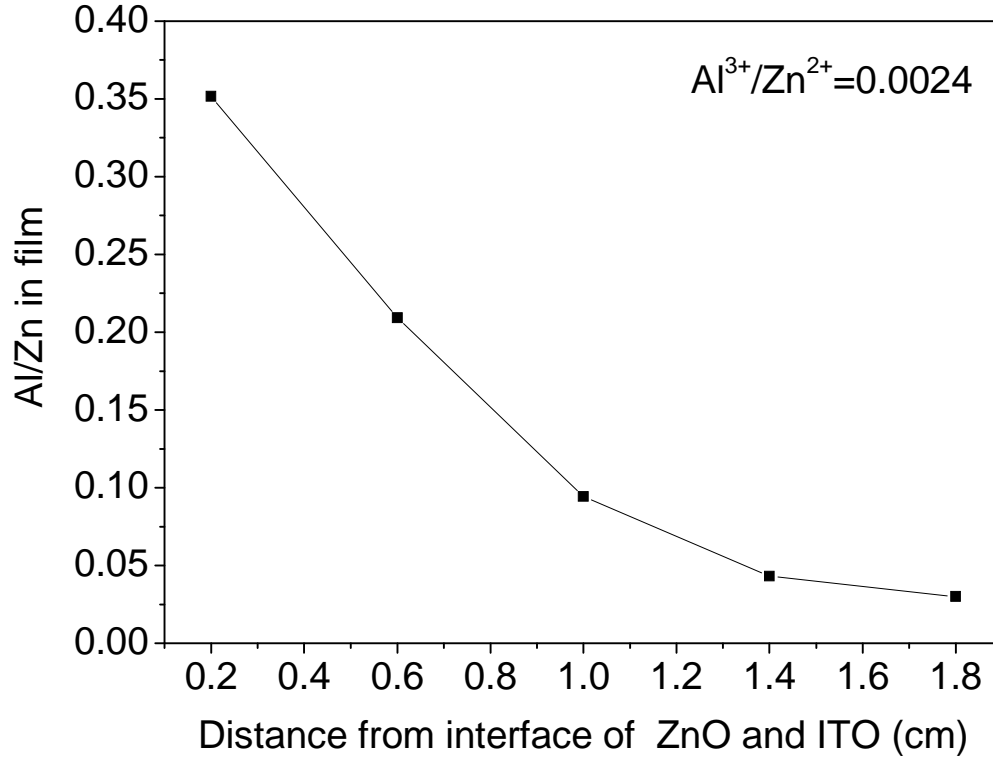
Figure 4.10 The Al/Zn atomic ratio at different position of the Al doped ZnO film.

4.4 Structure and Electrical Properties of Ga-Doped ZnO

Several samples were prepared from deposition solutions with different $Ga(NO_3)_3$ concentrations at 70 °C. The thickness of the films was controlled to between 400 and 500 nm and measured with a profilometer. Post-deposition annealing was carried out at 200 ºC for 3 hours in air, as the samples may have contained some $Zn(OH)_2$. After that, four-point probe was used for measuring the sheet resistance of the Ga-doped ZnO on ITO stack structure.
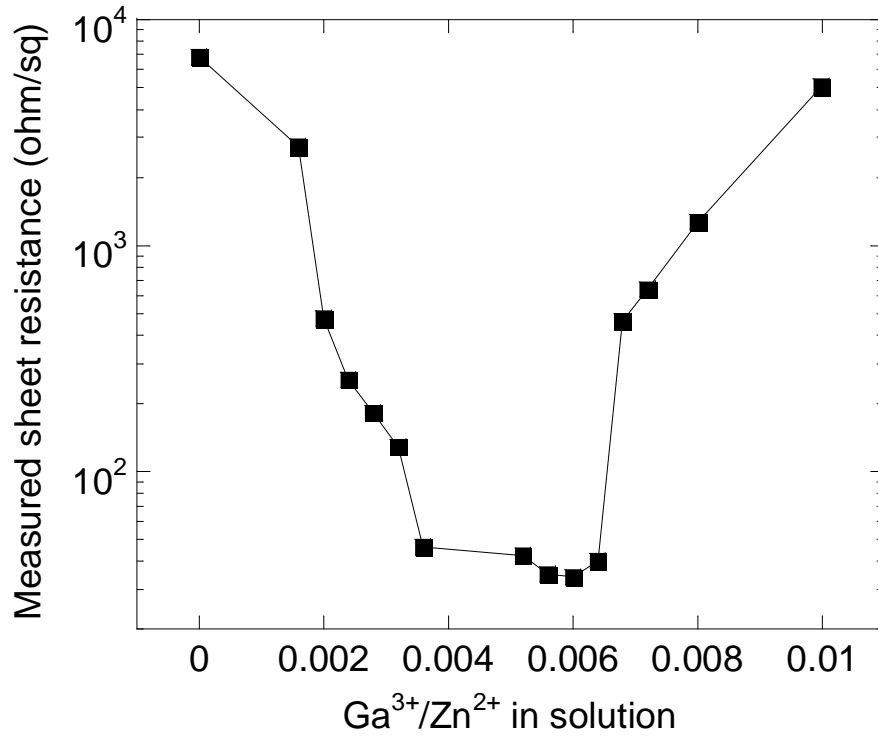
Figure 4.11 Measured sheet resistance of the Ga-doped ZnO on ITO stack as a function of the Ga^{3+}/Zn^{2+} ratio in the deposition solution. The as-deposited samples were annealed in air at 200 °C for 3 hours.

Figure 4.11 shows the measured sheet resistance of the Ga-doped ZnO on ITO stack structure as a function of the Ga^{3+}/Zn^{2+} ratio in the deposition solution. The measured sheet resistance initially decreases with increasing $Ga(NO_3)_3$ concentration, until it reaches the minimum point of 34 Ω/square. The corresponding Ga^{3+}/Zn^{2+} ratio is 0.006. This sheet resistance is a little lower than that of ITO, but the ZnO film is three times thicker than that of ITO. In this case, the resistivity of the Ga-doped ZnO film is ~2×10^{-2} Ω-cm, calculated by the same method for Al-doped ZnO shown in Figure 4.4. This resistivity is too high for a TCO.
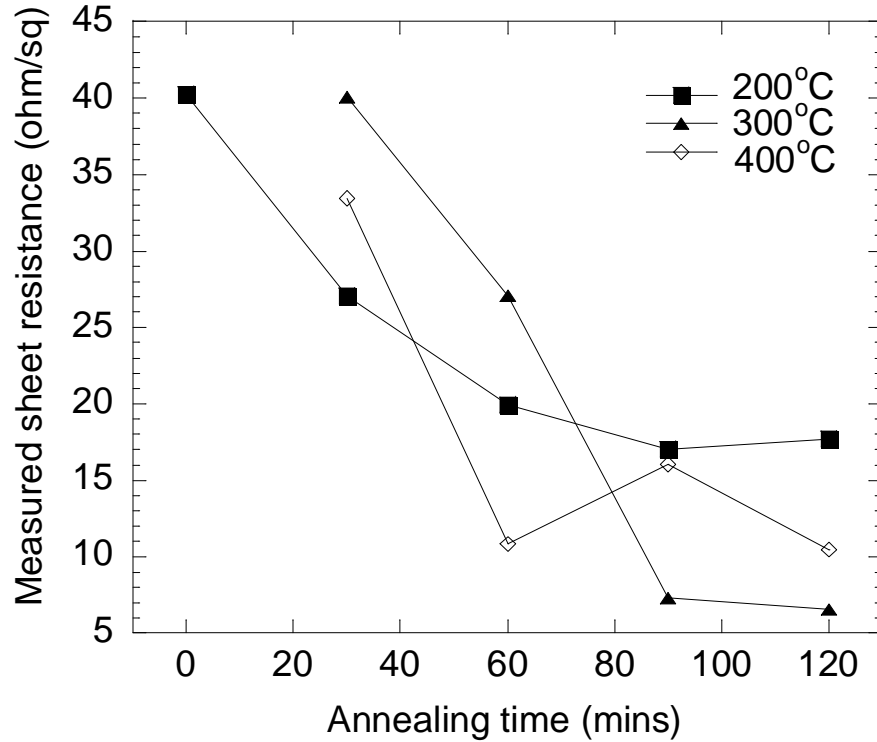
Figure 4.12 Measured sheet resistance of the Ga-doped ZnO on ITO stack as a function of annealing time and temperature. This annealing was performed in vacuum. The samples were deposited with a Ga^{3+}/Zn^{2+} ratio of 0.0064.

In order to further reduce the resistivity of Ga-doped ZnO to the low 10^{-4} Ω-cm range after the air annealing, vacuum annealing was performed on the Ga-doped ZnO films. In principle, annealing of ZnO in an oxygen-containing environment will change the chemical stoichiometry of ZnO due to the intake of O during annealing, which may affect its resistivity. For this reason, TCOs are often post-annealed in forming gas. Here, the Ga-doped ZnO films were annealed in vacuum below 1 µTorr to avoid O intake. Figure 4.12 shows the measured sheet resistance of the Ga-doped ZnO on ITO stack vacuum-annealed at different temperatures as a function of annealing time and temperature. These samples were deposited in a solution with the Ga^{3+}/Zn^{2+} ratio of 0.0064. The minimum sheet resistance of 7 Ω/square was obtained after

annealing at 300 °C for 2 hours in vacuum. The corresponding resistivity of this Ga-doped ZnO film was found to be 3.8×10^{-4} Ω-cm. This meets the resistivity requirement for TCOs.

(a)

(b)
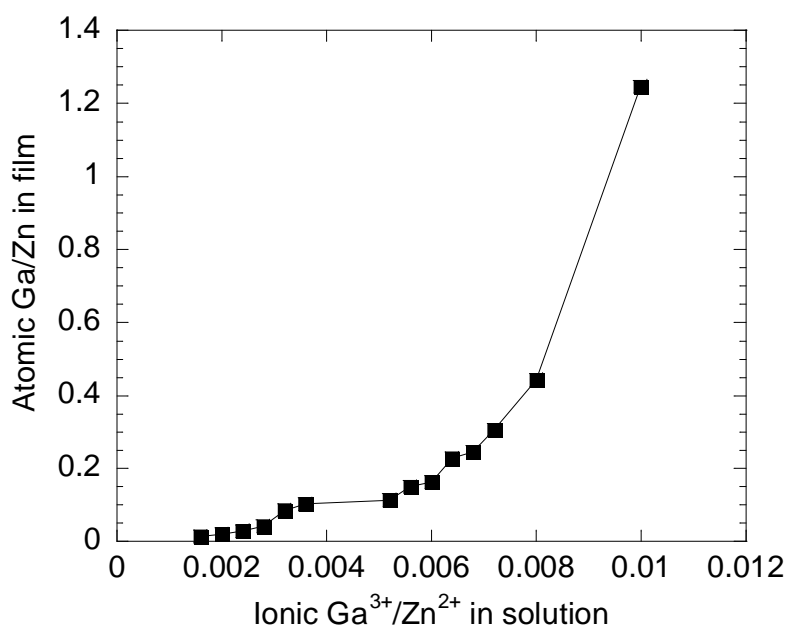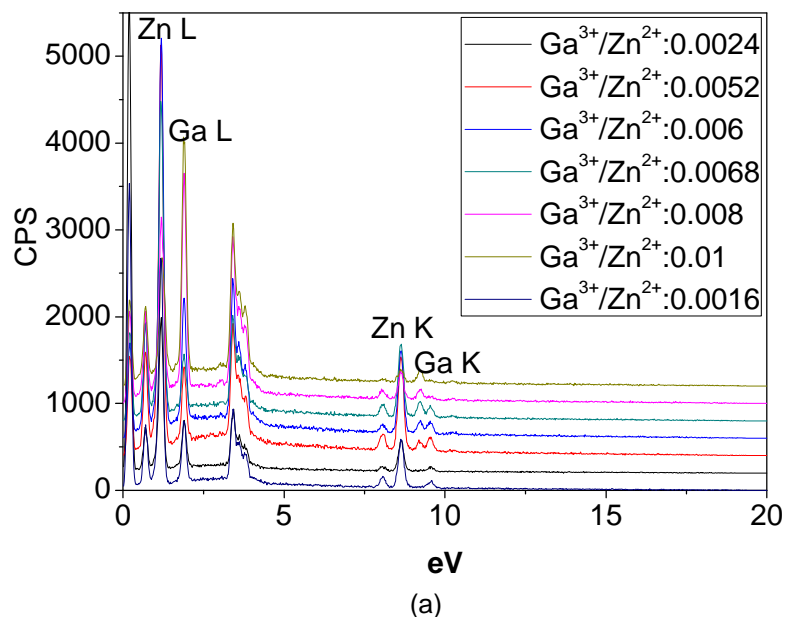
Figure 4.13 (a) EDS spectra of the Ga doped ZnO samples with different G^{3+}/Zn^{2+} and (b) the Ga/Zn atomic ratio in the Ga-doped ZnO films as a function of the Ga^{3+}/Zn^{2+} atomic ratio in the deposition solution.

The Ga concentration in the ZnO films was determined by EDS shown in Figure 4.13(a). Figure 4.13(b) shows the Ga/Zn atomic ratio in the Ga-doped ZnO films as a function of the Ga^{3+}/Zn^{2+} atomic ratio in the deposition solution. It clearly shows that the Ga concentration in the film increases with increasing Ga^{3+} concentration in the deposition solution co-responding to the increasing of the intensity of $Ga_{L\alpha}$ peak in Figure 4.13(a). The Ga/Zn atomic ratio corresponding to the minimum sheet resistance of 7 Ω/square is 0.23. This suggests that ZnO can tolerate a much higher Ga content than Al to achieve a much lower resistivity.
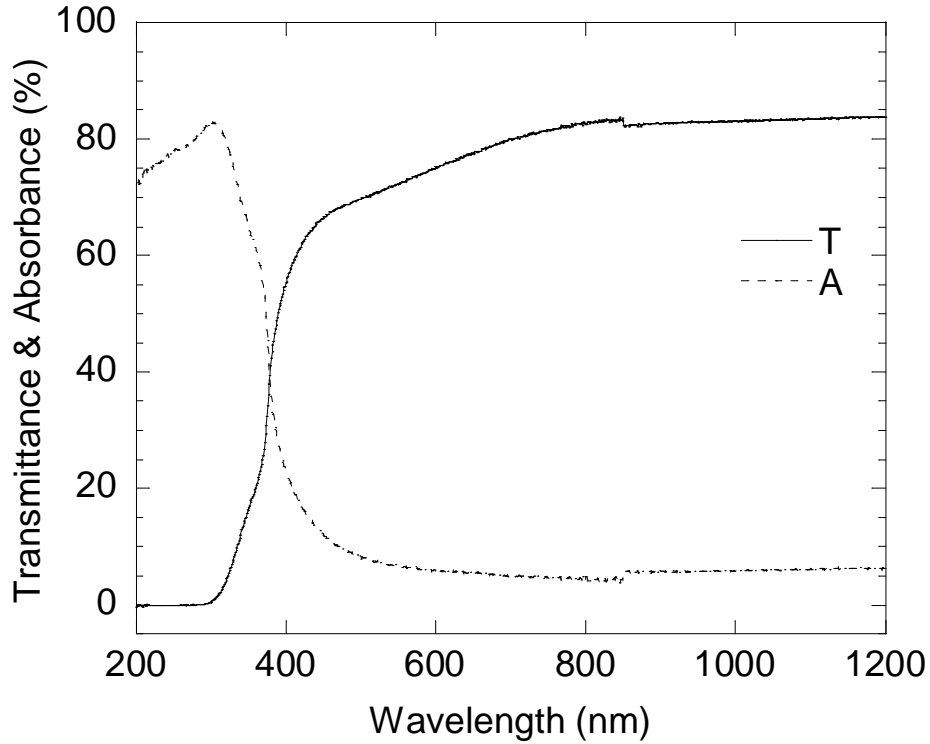
Figure 4.14 Total transmittance and absorbance of the Ga-doped ZnO on ITO stack. The sample was deposited with a Ga^{3+}/Zn^{2+} ratio of 0.0064.

Another important figure of merit for TCOs is high transmittance. Figure 4.14 shows the total transmittance of the Ga-doped ZnO on ITO stack and its absorbance calculated from the

transmittance and reflectance. Between 400 and 1,200 nm, the transmittance of Ga-doped ZnO is ~80%, while its absorbance is below 10%.

XRD measurements were performed to make sure that Ga-doped ZnO deposited under the conditions described above was actually ZnO. Figure 4.15 shows a XRD spectrum for a Ga-doped ZnO sample deposited at the Ga^{3+}/Zn^{2+} atomic ratio of 0.006 in the deposition solution. Two materials, ZnO and ITO, are clearly identified. No other crystals such as $Zn(OH)_2$ or Ga_2O_3 were detected. This proves that the deposition conditions described above produce ZnO. In_2O_3 was found to be the main component in the ITO film.
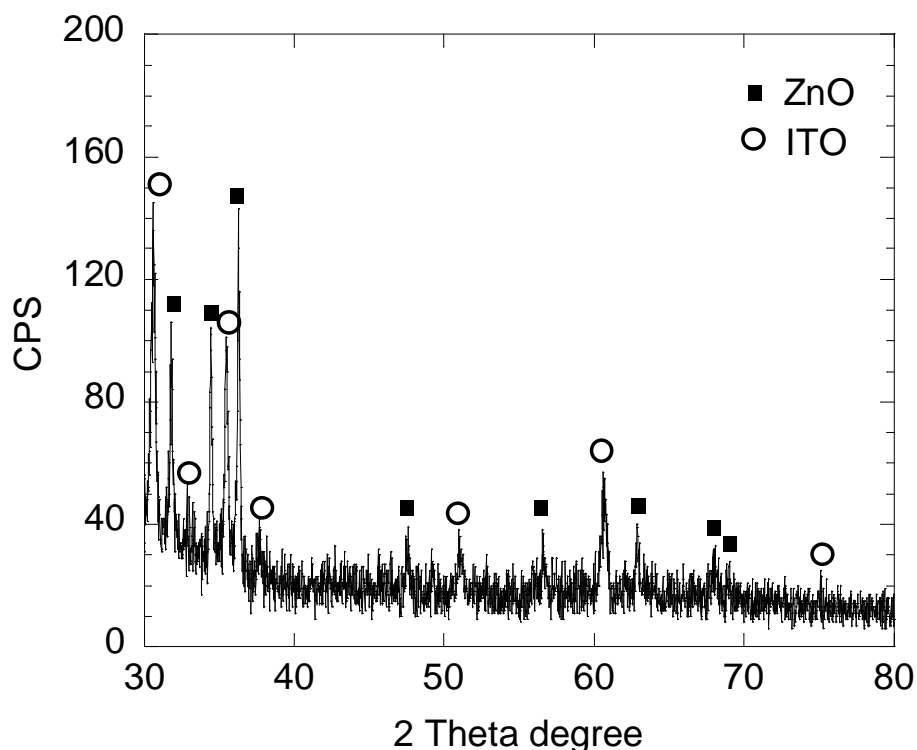
Figure 4.15 XRD spectrum of the Ga-doped ZnO on ITO stack. The sample was deposited in a deposition solution with the Ga^{3+}/Zn^{2+} atomic ratio of 0.006.

4.4 Summary

Al, Ga doped ZnO was electrodeposited on ITO substrate. A post annealing process was performed in air or vacuum to improve electrical property of those Al, Ga doped ZnO.

Finally, the Ga doped ZnO film with resistivity of 3.8×10^{-4} Ω-cm was obtained which is quite good for using as TCO layer. The SEM image shows the ZnO particle size is at um range. EDS determined the dopant concentration in the ZnO films. XRD result confirms the ZnO doesn't mix with ITO after annealing process. The high transmittance and low absorbance of those samples proved that this Al, Ga doped ZnO layer can be used on some solar cells which requires high transmittance and low resistivity TCO layer.

CHAPTER 5

ELECTRODEPOSITION AND CHARACTERIZATION OF Y DOPED ZnO

5.1 Introduction

Zinc oxide is an ideal material as a transparent conducting oxide (TCO) in a variety of optoelectronic devices, such as solar cells [81,82], flat-panel displays [83], and organic light-emitting diodes [84,85]. It is naturally n-type with a direct band gap of 3.3 eV. The natural abundance of the source materials, Zn and O, and the non-toxicity of ZnO make it particularly suitable for large-scale devices including solar cells and displays. It is believed that Zn is 30–40 times more abundant than tin in another popular TCO, tin oxide [86]. The two most important figures of merit for ZnO as a TCO are low resistance and high transmittance [87]. Undoped ZnO is highly resistive with carrier concentrations in the 10^{17} cm^{-3} range [88], and doping is needed to bring down the resistivity of ZnO to low 10^{-4} Ω-cm as required for TCOs in high-performance devices. The most common n-type dopant for ZnO is aluminum, where Group IIIA Al atoms substitute Group IIB Zn atoms in the lattice to provide excess electrons [89]. The lowest resistivity reported for Al-doped ZnO is in the mid to high 10^{-5} Ω-cm range by magnetron sputtering at room temperature [90] or pulsed laser deposition below 300 $^{\circ}$C [91], while the majority of the resistivity results by vacuum-based deposition is around 2×10^{-4} Ω-cm [59]. In the solar cell industry, the most common deposition method for Al-doped ZnO is sputtering for its relatively low cost and large area capability.

It is generally believed that solution-based deposition of ZnO has a lower cost than vacuum-based deposition. The problem with solution-deposited ZnO is that its resistivity is roughly 3 times higher than vacuum-deposited ZnO. The lowest resistivity reported for solution-prepared Al-doped ZnO is in the low 10^{-4} Ω-cm range by chemical bath deposition (hydrolysis) [92] or sol-gel process [93]. To reduce the resistivity of solution-prepared ZnO, other Group IIIA

66

elements have been tested, including gallium [94] and indium [95]. Electrochemical deposition of Ga-doped ZnO with the lowest resistivity of 3.8×10^{-4} Ω-cm has been reported [96]. The fundamental problem with Ga-doped ZnO for large-scale devices is that the annual global production of Ga is about 135 tons [86]. It is difficult to significantly increase Ga production, since Ga occurs in small concentrations (parts per million) in ores of other metals. A large quantity of those ores has to be processed to mine a little more Ga. Another Group IIIA element, In, suffers a similar problem. The reserve of In on this planet is about 16,000 tons [86], far short of the amount of material required for terawatt-scale solar cells.

<u>5.2 Experiment</u>

5.2.1. Sample Preparation

Electrochemical experiments were carried out using a Princeton Applied Research VERSTAT II potentiostat. Electrochemical deposition of Y-doped ZnO was performed by applying a constant potential between an indium tin oxide (ITO) coated glass substrate (working electrode) and a platinum foil (counter electrode). The deposition potential was -0.7 V versus a silver/silver chloride/saturated potassium chloride reference electrode. The ITO film was deposited on glass slides of 1×4 cm^2 in an AJA ATC ORION sputtering system and was 150 nm thick. After annealing in air at 400 °C, the sheet resistance of the ITO film reaches average 37 Ω/square, corresponding to a resistivity of ~5.5×10^{-4} Ω-cm. The Zn and Y precursors in the aqueous deposition solution were zinc nitrate ($Zn(NO_3)_2$) and yttrium nitrate ($Y(NO_3)_3$), respectively. The $Zn(NO_3)_2$ concentration was kept constant at 0.1 M for all the experiments, while the $Y(NO_3)_3$ concentration was varied to minimize the film resistivity. Deposition temperature was 70 °C, controlled by a Precision 280 water bath. The deposition time was 1 hour. After deposition, post-annealing was performed in an OTF-1200X tube furnace either under air or nitrogen. While annealing in N_2, the N_2 flowing pressure was 1 psi. The final sample image was shown is Figure 5.1. The Y doped ZnO was deposited on one side of the ITO coated glass, and on the other side ITO was still naked to air.
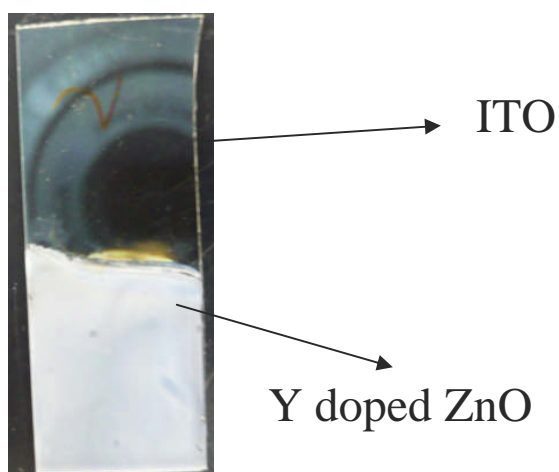
Figure 5.1 Y doped ZnO on ITO substrate sample image

The Y doped ZnO was also deposited on Ag coated stainless steel substrates with size also 1×4 cm^2. The stainless steel substrates were firstly polished by cotton polishing cloth. The final scratch size was reduced to be smaller than 1 um. The Ag film was electroplated on the stainless steel substrates after polishing. The electroplating solution contained 0.1 M Ag(NO$_3$) and 0.1 M NaCN. The electroplating was performed at room temperature and by constant potential -1.2 V. The whole area Ag electroplated was 1×4 cm^2. The total amount of charge passed through the electrochemical cell was controlled at 1.9 C. The co-responding thickness was 1 um calculated from Faraday equation. After electroplating, Ag coated stainless steel substrates were post-annealed in the vacuum (pressure<1 mTorr) at 200 °C for 30 minutes to improve the Ag film quality. After then, Y doped ZnO was electrodeposited on the Ag coated stainless steel substrates. The solution contained Y(NO$_3$)$_3$ and Zn(NO$_3$)$_2$ and the Y^{3+}/Zn^{2+} ionic ratio was 0.1. The solution temperature was 70 °C and the applied voltage was -0.8 V. Post-annealing was carried out after electrodeposition in the 1 ATM N$_2$ ambient with flowing pressure 1 psi at various temperatures for 1 hour in the OTF-1200X tube furnace. The final ZnO thickness was ~2.2 um.

5.2.2. Sample Characterization

The thickness of the ZnO films was ~400 nm, measured with a KLA-Tencor Alpha-Step IQ profilometer. The sheet resistance of the ZnO/ITO stack was measured with a Jandel four-point probe. The total transmittance and total reflectance of the ZnO/ITO/glass samples was measured by a UV/vis JASCO V570 spectrometer with an integrating sphere. Structural properties of the ZnO films were determined by a Siemens D-500 x-ray diffractometer using the copper Kα line. The morphology and composition of the Y-doped ZnO films were obtained with a Hitachi S-3000N scanning electron microscope equipped with an energy dispersive spectrometer.

5.2.3. Doping Mechanism

To help understand the doping mechanism involved in electrochemical deposition of Y-doped ZnO, cyclic voltammetry was performed in a deposition solution containing 0.1 M $Zn(NO_3)_2$ and 0.16 mM $Y(NO_3)_3$. The solution temperature was kept at 70 °C. As shown in Figure 5.2, there are two reduction reactions in the potential range of 0 and -1.2 V versus the Ag/AgCl reference electrode. One reduces nitrate ions (NO_3^-) to hydroxyl ions (OH^-):

$$H_2O + NO_3^- + 2e^- \rightarrow 2OH^- + NO_2^- \tag{R1}$$

which occurs around -0.65 V. The other reaction reduces Zn^{2+} ions to metallic Zn:

$$Zn^{2+} + 2e^- \rightarrow Zn \tag{R2}$$

which occurs below -0.8 V. When the applied potential is around -0.65 V, OH^- ions are produced in the deposition solution, which in turn react with Zn^{2+} ions in the solution to form ZnO:

$$Zn^{2+} + 2OH^- \rightarrow ZnO\downarrow + H_2O \tag{R3}$$

With the presence of Y^{3+} ions in the solution, the OH- ions also react with Y^{3+} ions to form yttrium oxide, which co-precipitates with ZnO, thus doping the ZnO film:

$$2Y^{3+} + 6OH^- \rightarrow Y_2O_3\downarrow + 3H_2O \tag{R4}$$

In this electrochemical deposition of Y-doped ZnO, the deposition potential selected was -0.7 V versus the Ag/AgCl reference electrode.

69

It is possible that hydroxides of Zn and Y ($Zn(OH)_2$ and $Y(OH)_3$), instead of oxides, are formed in the film under the conditions used. Since all the samples undergo post-deposition annealing as discussed later, reactions (R3) and (R4) represent the ultimate compounds in the film.
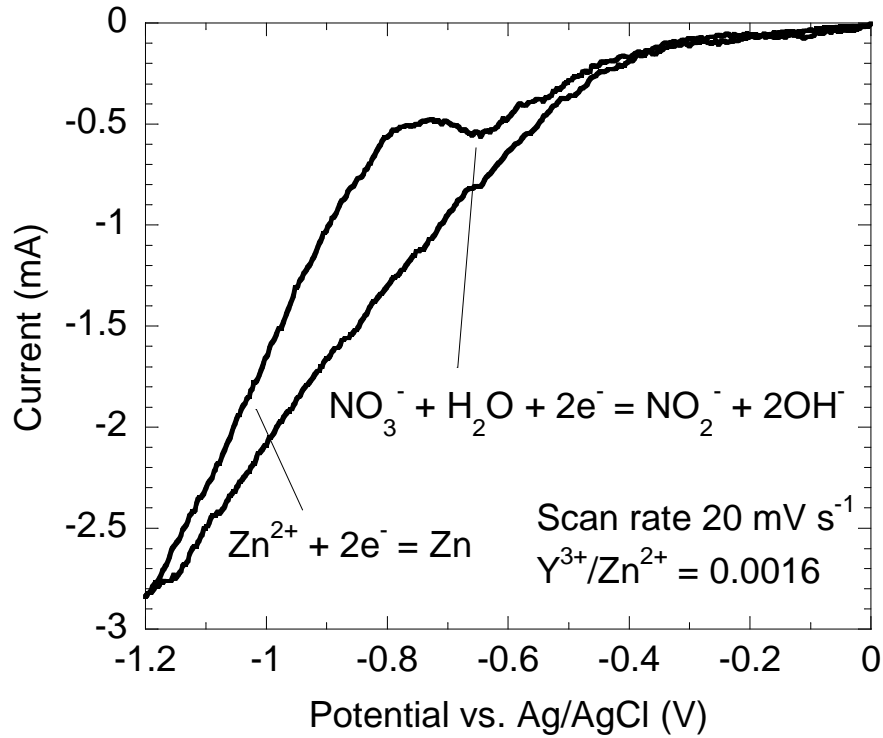
Figure 5.2 Cyclic voltammetry from a deposition solution containing 0.1 M $Zn(NO_3)_2$ and 0.16 mM $Y(NO_3)_3$. The solution temperature was 70 °C. The reduction reaction for producing OH- ions is around -0.65 V versus the Ag/AgCl reference electrode.

5.3 Electrical and Optical Properties of Y Doped ZnO

5.3.1. Electrical Properties

The main important parameter of ZnO working as a TCO layer is resistivity. Low resistivity can guarantee the TCO layer has good electrical property. The resistivity of ZnO can be calculated from the sheet resistance of ZnO. Four point probe system was used for the measurement.

(a)
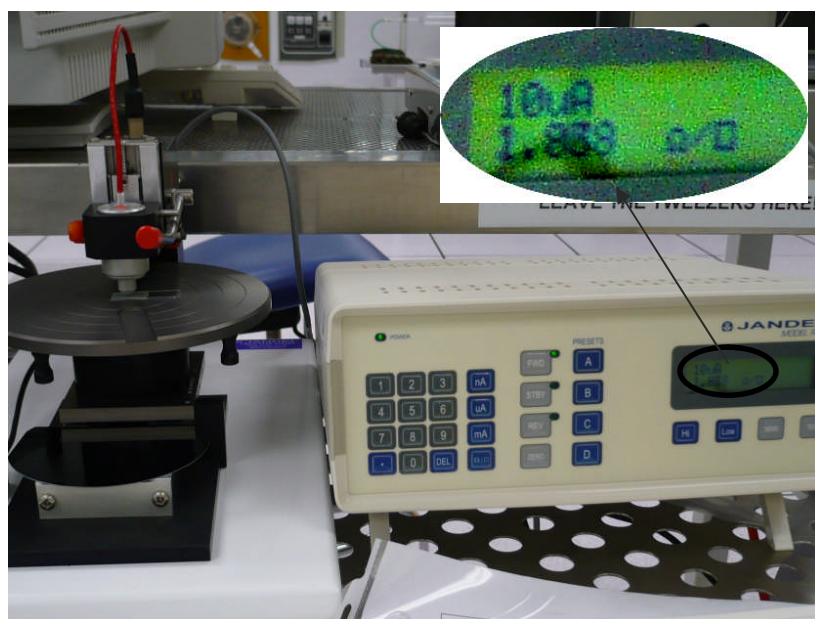
(b)

Figure 5.3 Image of measuring sheet resistance of (a) ITO and (b) ZnO+ITO stack structure by a four point probe system.

In order to measure the sheet resistance of ZnO, the sheet resistance of the ITO was measured, firstly. Figure 5.3(a) shows the sheet resistance of the ITO film which is 33.3 Ω/

square when the four point probe tips were placed on the ITO side. The sheet resistance of home-made ITO is in 30-40 Ω/square range and average ~37 Ω/square by measuring multi-times. And then the four point probe tips were put on the Y doped ZnO side and measured the sheet resistance of Y doped ZnO, ITO stack structure. The result is 1.838 Ω/square much lower than that of ITO.

The most important parameter which controls the doping level and resistivity of the ZnO film is the Y concentration in the deposition solution. The sheet resistance of undoped and Y-doped ZnO on ITO-coated glass substrate as a function of Y^{3+}/Zn^{2+} ratio in the deposition solution is shown in Figure 5.4(a). The $Zn(NO_3)_2$ concentration was fixed at 0.1 M and the solution temperature was controlled at 70 °C. The sheet resistance data was also measured by four-point probe. The as-deposited samples were annealed in air at 200 °C for 3 hours since they may have contained hydroxides of Zn and Y. The ZnO and ITO films were considered as a parallel circuit and the following equation was used to calculate the sheet resistance of the ZnO film:

$$\frac{1}{R_{ITO}} + \frac{1}{R_{ZnO}} = \frac{1}{R_{Stack}}$$

where R_{ITO} is the measured sheet resistance of the ITO film (37 Ω/square), R_{ZnO} is the sheet resistance of the ZnO film to be determined, and R_{Stack} is the measured sheet resistance of the ZnO/ITO stack. This equation fails when the ZnO film becomes highly resistive ($R_{ZnO} \gg R_{ITO}$). When this happened, the approximation that $R_{ZnO} \approx R_{Stack}$ was used. The resistivity of Y-doped ZnO was calculated from its sheet resistance and thickness:

$$\rho_{ZnO} = R_{ZnO} \times t_{ZnO}$$

where t_{ZnO} is the thickness of the ZnO film (~400 nm). The sheet resistance of the undoped ZnO film is 6.8 kΩ/square. No TCO with such a high sheet resistance can produce a high-performance device. However, with 2.8 mM $Y(NO_3)_3$ in the solution (Y^{3+}/Zn^{2+} ratio 0.028),

72

the sheet resistance of the ZnO/ITO stack is significantly reduced to the minimum, 4Ω/square, and the corresponding resistivity of the ZnO film is 1.8×10^{-4} Ω-cm.
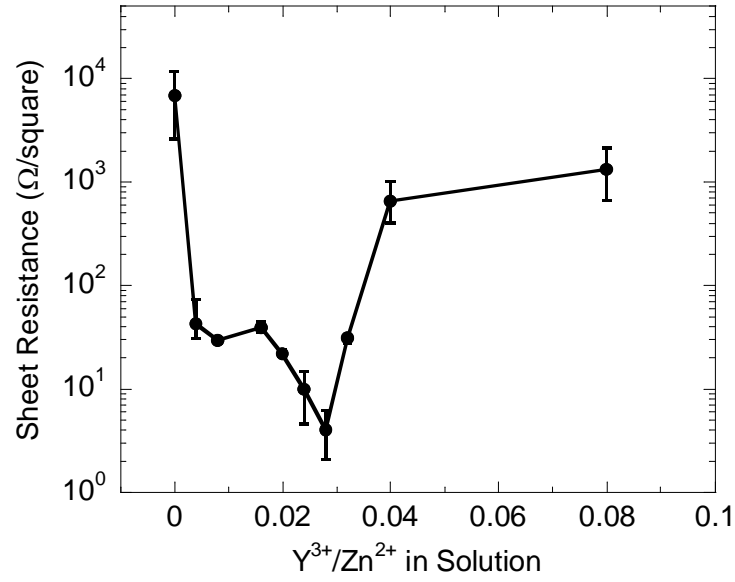
(a)
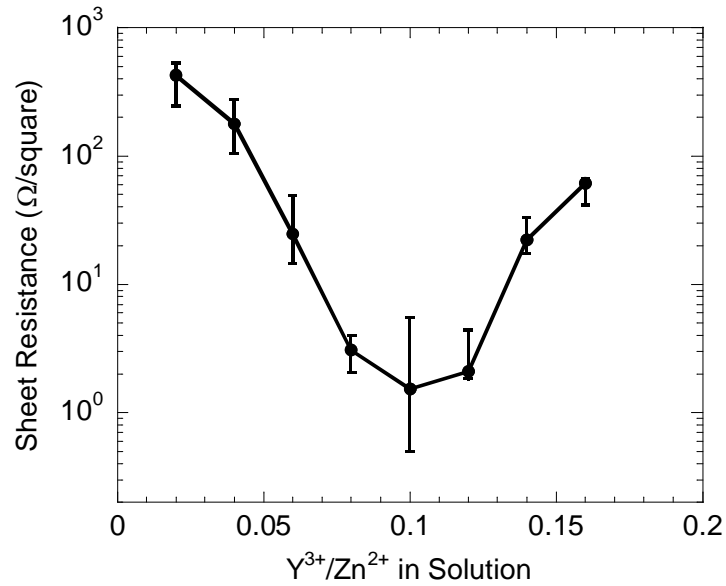
(b)

Figure 5.4 Measured sheet resistance of undoped and Y-doped ZnO films as a function of Y^{3+}/Zn^{2+} ratio in the deposition solution after post-deposition annealing (a) in air at 200 ºC for 3 hours and (b) in N_2 at 300 ºC for 3 hours.

When the $Y(NO_3)_3$ concentration exceeds 2.8 mM (Y^{3+}/Zn^{2+} ratio exceeds 0.028), the sheet resistance starts to increase. This is probably due to the precipitation of Y_2O_3 from the ZnO lattice, since Y_2O_3 has a large band gap than ZnO, 5.6 eV [97].

Figure 5.4(b) shows the sheet resistance of Y-doped ZnO as a function of Y^{3+}/Zn^{2+} ratio in the deposition solution, where the as-deposited samples were annealed in 1 atm N_2 at 300 ºC for 3 hours in a tube furnace. With the Y^{3+}/Zn^{2+} ratio of 0.1 in the solution ($Y(NO_3)_3$ concentration 10 mM), the ZnO film achieves the minimum sheet resistance of 1.5 Ω/square. It should be noted that for this particular set of samples, the minimum sheet resistance appears at the Y^{3+}/Zn^{2+} ratio of 0.1. Other sets of samples have shown minimum sheet resistance at the Y^{3+}/Zn^{2+} ratio of 0.08. 1.5 Ω/square sheet resistance corresponds to a resistivity of 6.3×10^{-5} Ω-cm for ZnO. Even with possible measurement errors considered, i.e. the ITO sheet resistance is 50% lower (24.7 instead of 37 Ω/square) and the ZnO film is 50% thicker (600 instead of 400 nm), the corresponding resistivity is only 1×10^{-4} Ω-cm. These are the lowest resistivities reported for any solution-prepared ZnO doped with an abundant element. They compare favorably to vacuum-prepared Al-doped ZnO [90,91].

5.3.2. Optical Properties

Transmittance and reflectance characterization was performed on Y-doped ZnO by UV/vis spectroscopy with an integrating sphere. Figure 5.5 shows the total transmittance and absorbance of a Y-doped ZnO sample deposited at the Y^{3+}/Zn^{2+} ratio of 0.08 and solution temperature of 70 °C. The sample was post-annealed at 300 °C for 2.5 hours in N_2. The absorbance was calculated from the following equation: $A = 1 - T - R$. The Y-doped ZnO sample shows high transmittance of ~80 % and low absorbance of ~10 % for a thickness of 400 nm.
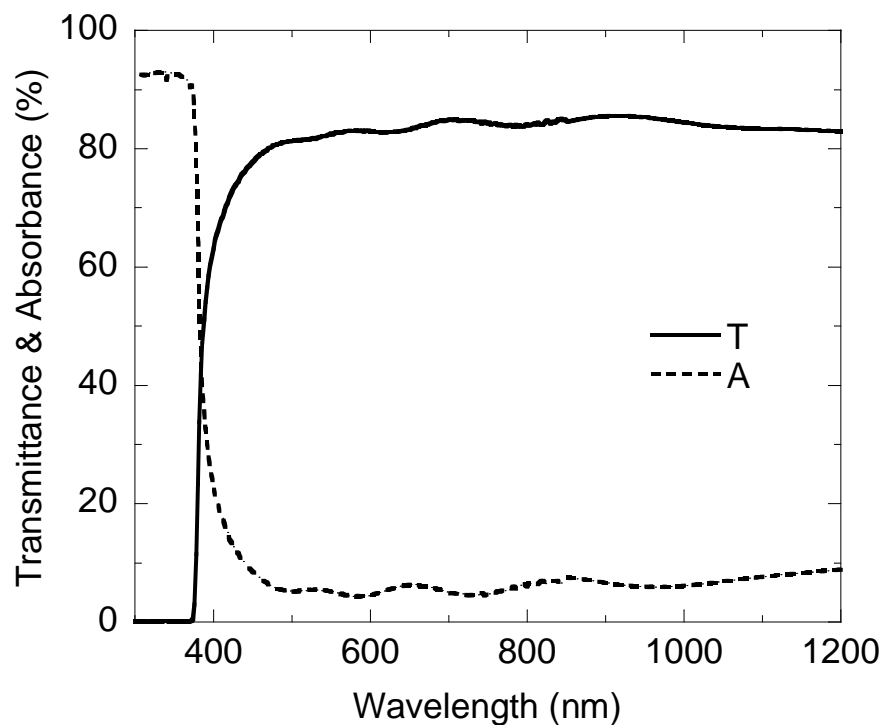
Figure 5.5 Total transmittance and absorbance of a Y-doped ZnO sample post-annealed in N_2 at 300 °C for 2.5 hours. The sample was deposited with the Y^{3+}/Zn^{2+} ratio of 0.08 and at solution temperature of 70 °C.

5.4 Morphology and composition of Y doped ZnO

5.4.1. Morphology

Figure 5.6(a) shows a scanning electron micrograph of the morphology of as-deposited Y-doped ZnO. The accelerate voltage was 20 KV and the saturate current was around 100 uA. The sample was deposited at the Y^{3+}/Zn^{2+} ratio of 0.08 and solution temperature of 70 °C. The micrograph shows a continuous but textured polycrystalline ZnO film. The grain size varies between 100 and 800 nm. Many grains have a hexagonal shape, suggesting preferential growth along the c-axis of ZnO. Some areas are bright and some areas are gray which this as-grown sample has large roughness.
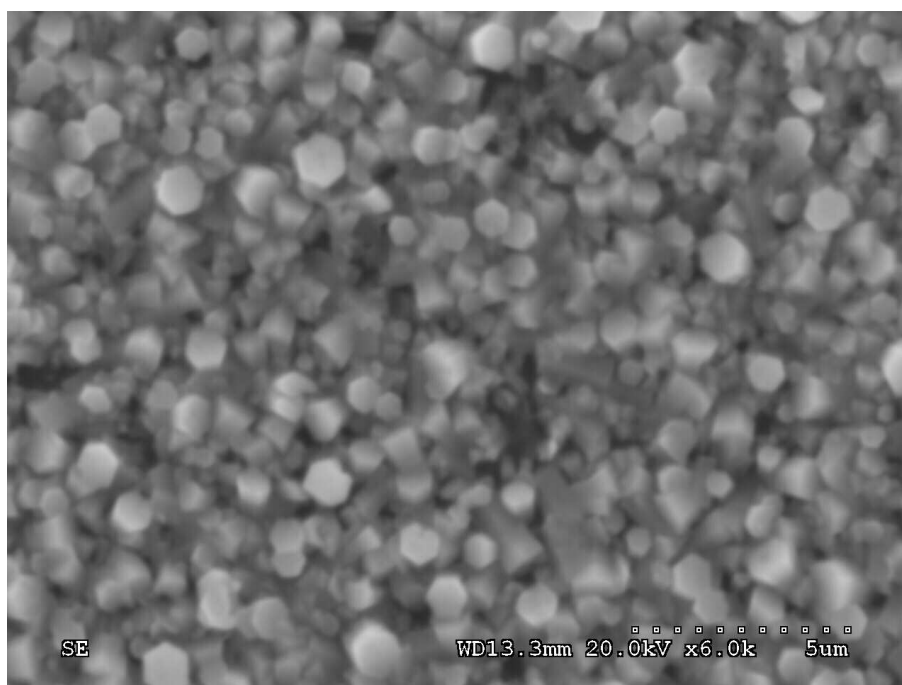
(a)
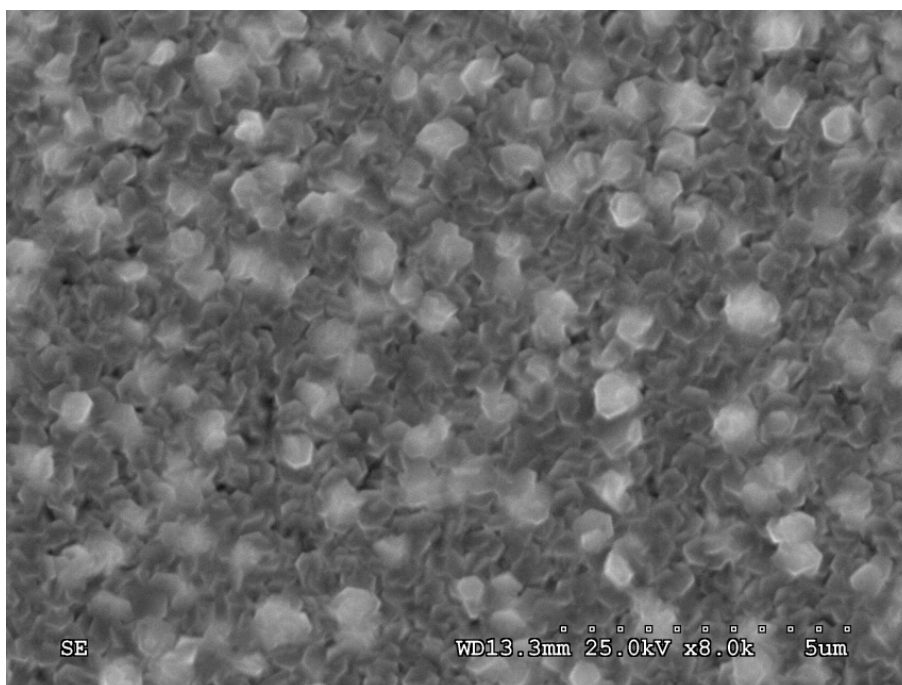
(b)

Figure 5.6 SEM micrograph of a Y-doped ZnO sample (a) as-deposited and (b) after post-annealed in N_2 at 300 °C for 2.5 hours. The sample was deposited at the Y^{3+}/Zn^{2+} ratio of 0.08 and at solution temperature of 70 °C.
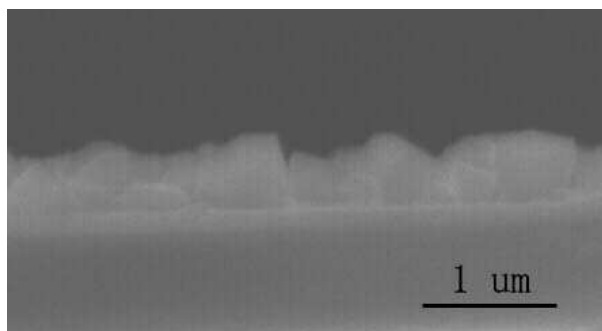
Figure 5.7 SEM cross-section micrograph of a Y-doped ZnO sample after post-annealed in N_2 at 300 °C for 2.5 hours. The sample was deposited at the Y^{3+}/Zn^{2+} ratio of 0.08 and at solution temperature of 70 °C.

The morphology between the as-grown Y doped ZnO sample and the sample after post- annealed has a big difference. Figure 5.6(b) shows the SEM image of the Y doped ZnO sample after post-annealed in N_2 at 300 °C for 2.5 hours. Compared to Figure 5.6(a), the crystal of Y doped ZnO after post-annealing looks more like amorphous. The main reason is during N_2 annealing the crystal starting to recover and the grain boundary of the crystal becomes fuzzy. And also it is in agreement with the electrical properties improvement after annealing.

Figure 5.7 shows the SEM cross-section micrograph of a Y-doped ZnO sample after post-annealed in N_2 at 300 °C for 2.5 hours. The sample was deposited at the Y^{3+}/Zn^{2+} ratio of 0.08 and at solution temperature of 70 °C. From this image, it can be clearly seen three layers which are glass substrate, ITO and ZnO. The thickness of the ITO is ~150 nm and ZnO is ~400 nm which can be estimated from this cross-section SEM image.

5.4.2. Composition

X-ray diffraction measurements were performed to confirm the presence of crystalline ZnO. Figure 5.8 shows the diffraction pattern of a Y-doped ZnO sample deposited at the Y^{3+}/Zn^{2+} ratio of 0.08 and solution temperature of 70 °C. The sample was post-annealed in N_2 at 300 ºC for 2.5 hours. The 34.4°, 36.2°, 47.6°, and 62.9° peaks marked with solid dots correspond to ZnO (002), (101), (102), and (103), respectively. The remaining peaks are indium oxide (222), (400), and (622), which are marked with open dots. Only ZnO and In_2O_3 peaks

77

exist, and metallic Zn and $Zn(OH)_2$ peaks are below the detection limits (~1%). The ZnO peaks are clearly separated from the ITO peaks, indicating no intermixing of ZnO with ITO by the post-deposition annealing. It is suggested that the low resistivity of Y-doped ZnO is not due to the effect of the ITO film underneath. The ZnO peaks are stronger than the ITO peaks, since the ITO film is 150 nm thick as compared to the 400 nm ZnO film.
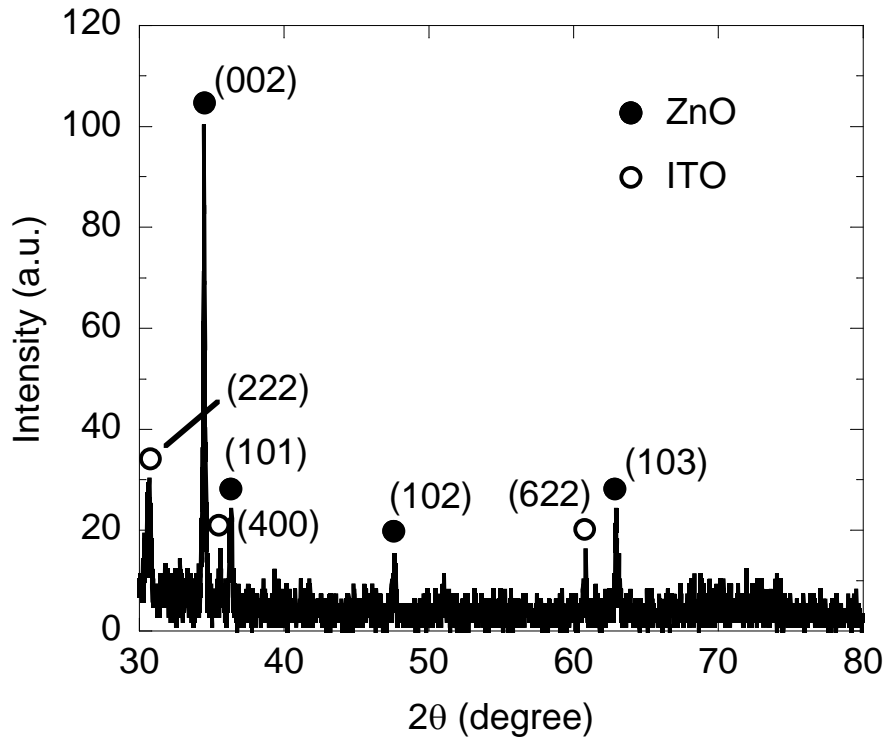
Figure 5.8 XRD pattern of a Y-doped ZnO sample post-annealed in N_2 at 300 °C for 2.5 hours. The sample was deposited with the Y^{3+}/Zn^{2+} ratio of 0.08 and at solution temperature of 70 °C.

Figure 5.9 shows energy dispersive spectroscopy measurements of the Y concentration (in the form of Y/Zn ratio) in as-deposited samples as a function of Y^{3+}/Zn^{2+} ratio in the deposition solution. The Y concentration in the ZnO film increases with an increasing Y concentration in the solution, but in a nonlinear fashion. As shown in Figure 5.9, the Y^{3+}/Zn^{2+} ratio in the solution corresponding to the minimum sheet resistance in Y-doped ZnO is 0.1.

Figure 5.9 reveals that the Y/Zn ratio in the film corresponding to the Y^{3+}/Zn^{2+} ratio of 0.1 in the solution is 0.08, or the Y concentration in the record-resistivity ZnO film is 3.7 atomic %.
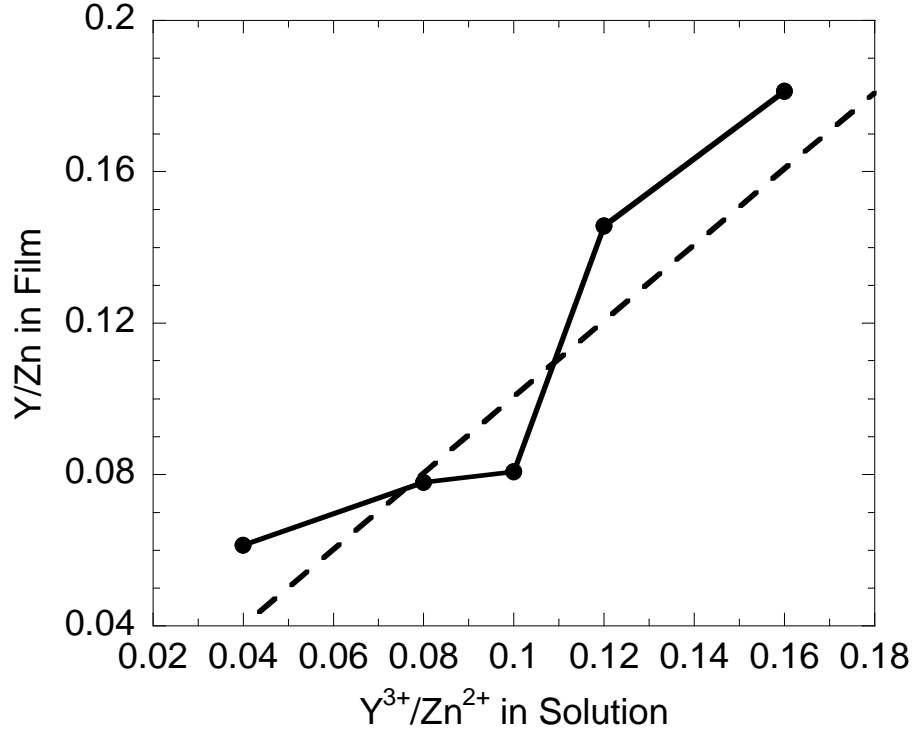
Figure 5.9 Measured Y/Zn ratio in Y-doped ZnO films by EDS as a function of Y^{3+}/Zn^{2+} ratio in the deposition solution. The dashed line indicates where Y/Zn ratio in film is equal to Y^{3+}/Zn^{2+} ratio in solution.

5.4.3. Uniformity

The sheet resistance measurement shows the uniformity of the Y doped ZnO is not so good. In some areas, the sheet resistance data can not be obtained from the four point probe due to contact problem. In order to measure the roughness, Atomic Force Microscopy (AFM) was used to observe 3 dimensional image of the Y doped ZnO sample before and after annealing process. Figure 5.10(a) shows the AFM 3 dimensional image of as-grown Y doped ZnO on ITO sample. The Y doped ZnO sample was deposited from solution $Y^{3+}/Zn^{2+}=0.1$ and temperature 70 °C. This image shows clear hexagonal shape of ZnO particles. The average

79

roughness measured from this AFM image is 89.5 nm. Compared to the thickness of the ZnO, the roughness is high.
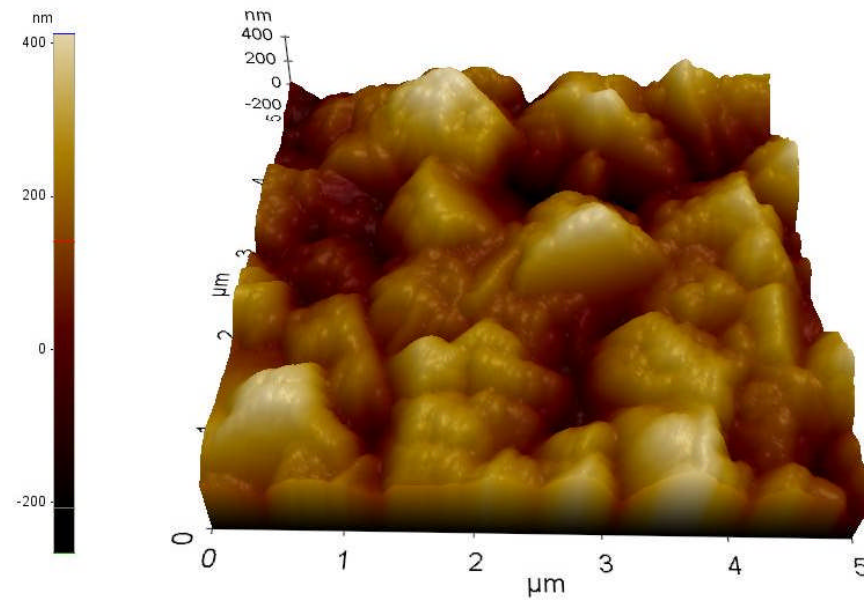
(a)
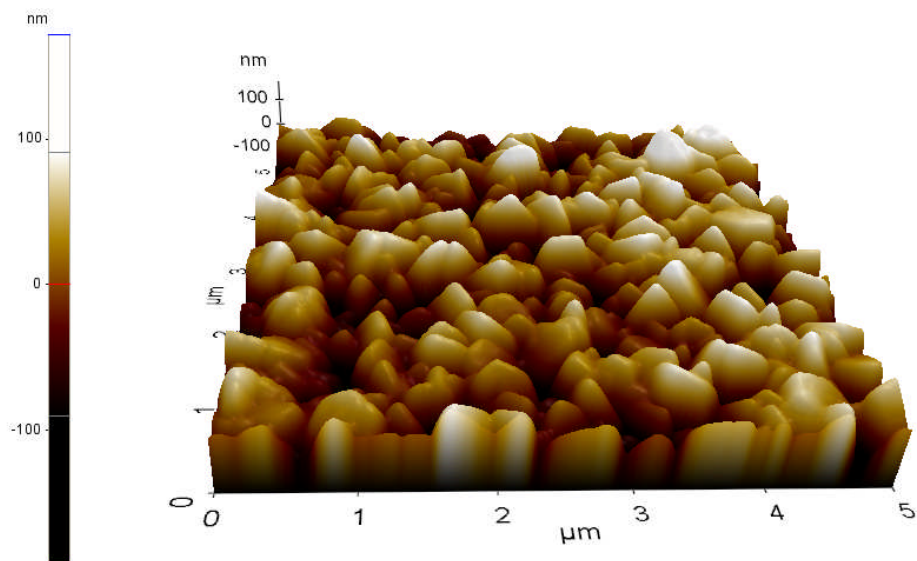
(b)

Figure 5.10 Atomic Force Microscope 3 dimensional images of Y doped ZnO on ITO substrate sample (a) before annealing and (b) after annealing.

Figure 5.10(b) shows the Atomic Force Microscopy (AFM) 3 dimensional image of Y doped ZnO on ITO substrate sample after post-annealing. This sample was placed in the tube furnace under 1 atm N_2 for annealing 3 hours at 300 °C. It seems morphology has been changed after annealing and the roughness of this Y doped ZnO was also reduced to 36.6 nm. There is more than half of the reducing in roughness of as-grown sample.

5.5 Effects of Post-Deposition Annealing

Figure 5.11(a) shows the sheet resistance of Y-doped ZnO as a function of annealing time and temperature in 1 ATM N_2. The samples were deposited at the Y^{3+}/Zn^{2+} ratio of 0.08 and solution temperature of 70 °C. At both 200 and 300 °C, the sheet resistance of the ZnO/ITO stack is reduced from ~100 Ω/square to a few Ω/square after 3 hours of annealing. The minimum sheet resistance in this experiment is obtained at 300 °C, 2.43 Ω/square, corresponding to a resistivity of 1.0×10^{-4} Ω-cm for the ZnO film. Post-deposition annealing affects primarily the crystallization of the polycrystalline ZnO films. Higher temperatures and longer times help crystallization and driving more Y atoms into the ZnO lattice, leading to more effective dopant activation.

Figure 5.11(b) shows the effect of vacuum annealing on sheet resistance of Y-doped ZnO. The Y-doped ZnO samples were deposited at the Y^{3+}/Zn^{2+} ratio of 0.08 and solution temperature of 70 °C. The vacuum annealing was performed at 1×10^{-6} Torr. At 300 °C and for 2 hours, the sheet resistance of Y-doped ZnO is reduced to a minimum of 8.29 Ω/square, corresponding to a resistivity of 4.3×10^{-4} Ω-cm for the ZnO film. In principle, annealing ZnO in vacuum is likely to change the chemical stoichiometry, and thus the native point defects, of ZnO due to the loss of O during annealing. A comparison of Figures 6.11(a) and (b) reveals the importance of annealing ambient on the final resistivity of Y-doped ZnO.
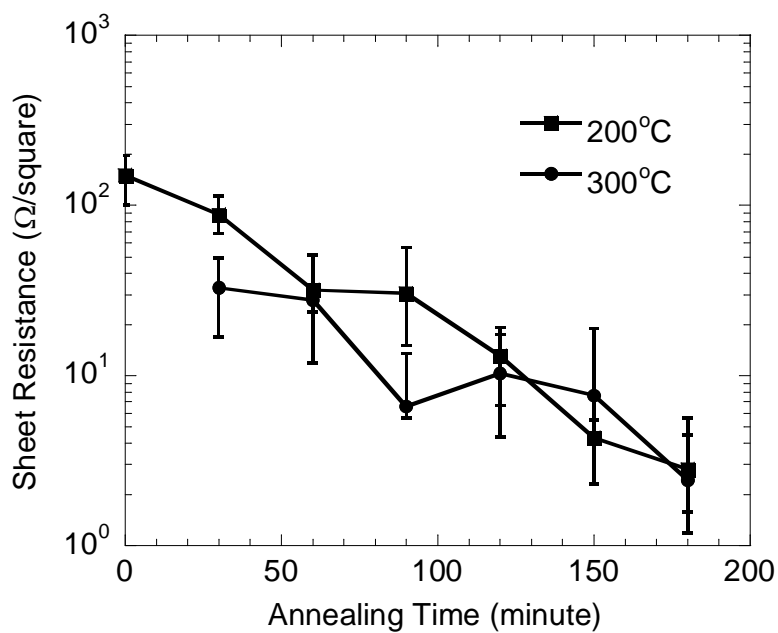
(a)
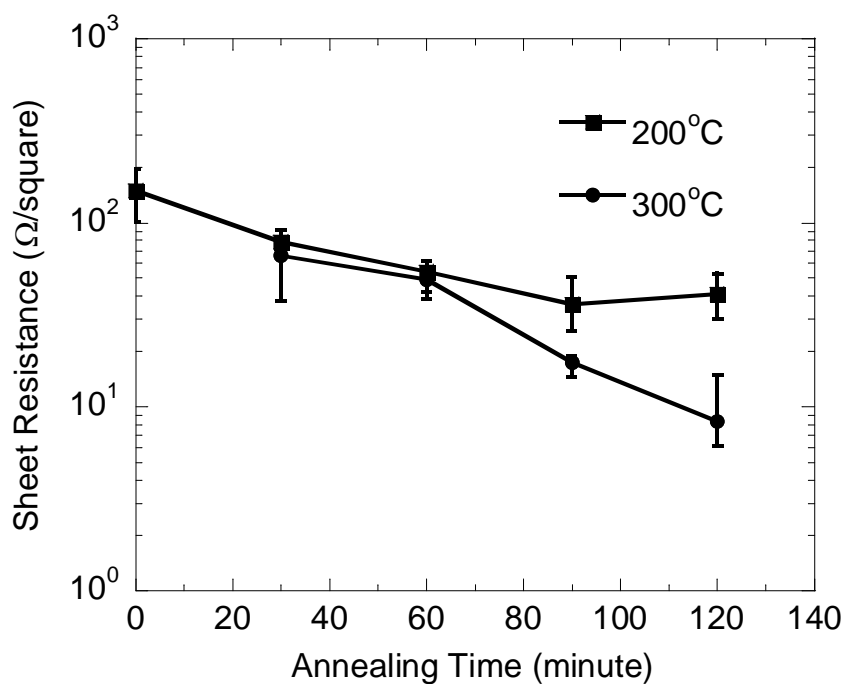
(b)

Figure 5.11 Measured sheet resistance of Y-doped ZnO films as a function of annealing time and temperature (a) in N_2 and (b) in vacuum. The samples were deposited with the Y^{3+}/Zn^{2+} ratio of 0.08 and at solution temperature of 70 °C.

<u>5.6 Statistics of the Resistivity of Y-Doped ZnO</u>

The reproducibility of low resistivity Y-doped ZnO has been examined. Figure 5.12 shows the resistivity results from ten Y-doped ZnO samples. These samples were prepared under the same conditions as the sample with the minimum sheet resistance in Figure 5.4, i.e. Y^{3+}/Zn^{2+} ratio 0.1, deposition temperature 70 °C, post-annealing temperature 300 °C, annealing time 3 hours, and annealing ambient N_2. Six out of the ten samples have resistivity at or below 2×10^{-4} Ω-cm, while three samples are above 8×10^{-4} Ω-cm. The lowest resistivity for this set of samples is 7×10^{-5} Ω-cm. The fluctuation in resistivity is likely due to the non-uniform ZnO films as shown in Figure 5.6, as well as fluctuations in Y concentration in the ZnO films due to growth kinetics.
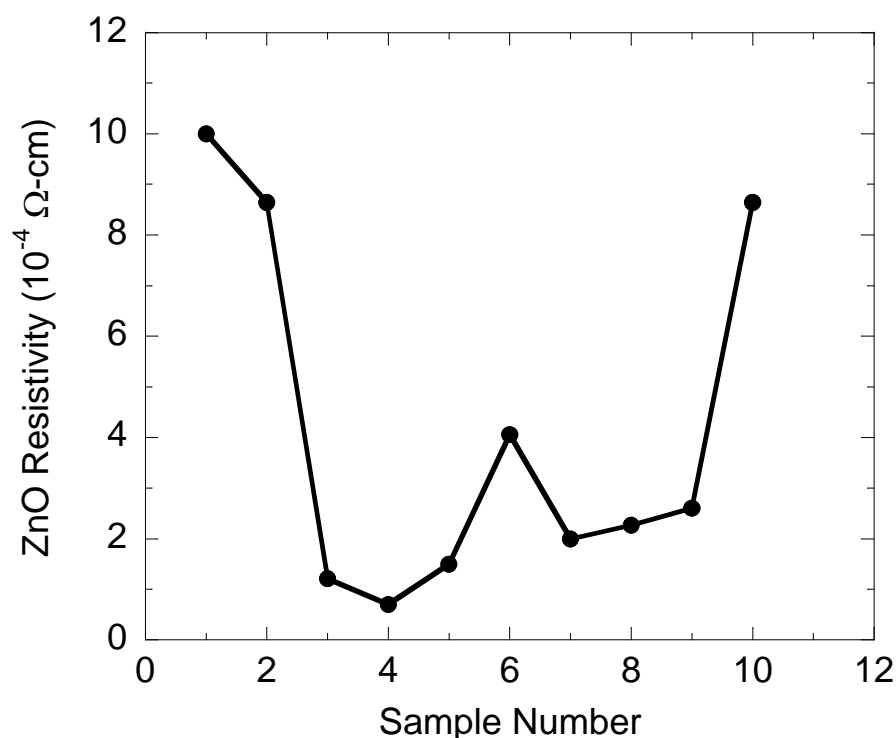
Figure 5.12 Statistics of the resistivity results for ten Y-doped ZnO samples prepared and annealed under the same conditions: Y^{3+}/Zn^{2+} ratio 0.1, solution temperature 70 °C, annealing temperature 300 °C, annealing time 3 hours, and annealing ambient N_2.

5.7 Thermal Stability Test

5.7.1. Deposition of n-Type Doped ZnO as Back Reflector

ZnO can be not only the top transparent contact but also the back reflector on the substrate; both applications need low resistivity. Figure 5.13 shows the typical structure of amorphous Si solar cell [104]. This back reflector ZnO layer on metal substrate is usually 1-2 um thick. It works as the barrier between silicon and the metal. The reason is that the metal may diffuse into the silicon layer under a high process temperature without an inert barrier. In this case, this ZnO barrier should be also high conductive and low light absorbance like TCO.

Y doped ZnO films can be used to enhance the back reflection in p-i-n solar cells. The achievement of a high conversion efficiency in an a-Si:H alloy solar cell requires efficient light trapping in the intrinsic (i) layer. The light trapping (mainly wavelength > 600 nm) may be achieved by the deposition of a suitable back-reflector material onto the n/metal interface. The short-circuit current density (Jsc) can be significantly enhanced by using the low resistivity of ZnO such as Y doped ZnO. The metal substrate can be stainless steel which has enough hardness and conductivity. The back-reflector film must possess two essential properties: (i) high optical reflectance, especially in the longer-wavelength region and (ii) optimum surface texture for light scattering [104]. Y doped ZnO has high transmittance, low absorbance and low resistivity. If it can be uniformly electrodeposited on the metal substrate, it can largely enhance the performance of the thin film solar cells. More over silver coated stainless steel or aluminum coated stainless steel can be used instead of stainless steel as the substrate to increase the reflectivity.
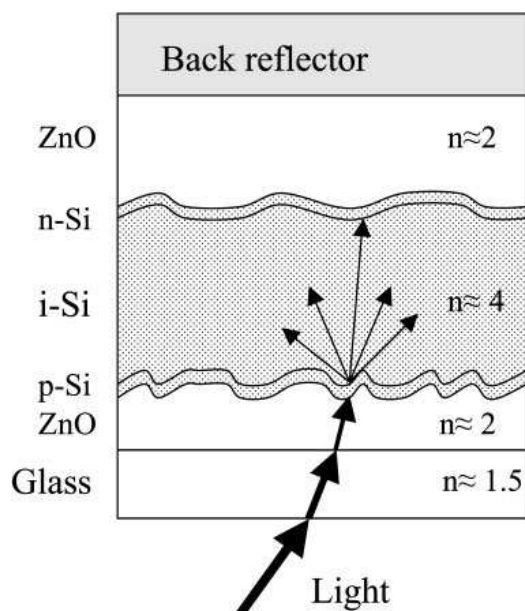
Figure 5.13 Schematic sketch of a typical p–i–n thin-film silicon solar cell, as used both for a-Si:H and for mc-Si:H. The values for n indicated here give approximate values of the optical index of refraction, an important parameter for light trapping considerations. A glass substrate is assumed here; this corresponds to the so-called superstrate configuration.

5.7.2. Electrical Properties after Thermal Stability Test

Amorphous Si films are usually deposited by PECVD at ~300 ºC. To work as a back reflector in amorphous Si solar cells, the Y doped ZnO must remain low resistance and high transmittance at a temperature similar to 300 ºC. Y-doped ZnO was electrochemically deposited on Ag-coated stainless steel substrate at the Y^{3+}/Zn^{2+} ratio of 0.1. The Ag coating was electroplated onto the stainless steel substrate at room temperature and post-annealed in the vacuum (pressure<1 mTorr). The Ag electroplating solution contains 0.1 M $AgNO_3$ and 0.1 M NaCN. The Ag post-annealing temperature was 300 °C and the temperature was 30 minutes. The Y doped ZnO electrodeposition solution contained 0.1 M $Zn(NO_3)_2$ and 0.01 M $Y(NO_3)_3$ and the solution temperature was controlled at 70 °C. The final structure is shown in Figure 5.14.

Post-deposition annealing of Y-doped ZnO on Ag-coated stainless steel was performed at temperature 400 °C and 500 °C in 1 ATM N_2 ambient for 1 hour to examine its thermal reliability. N_2 gas flowing pressure was 1 psi. For resistivity measurements, Al dots with an area

of 3.6×10^{-4} cm^2 were deposited by thermal evaporation on Y-doped ZnO through a shadow mask. Current-voltage characterization was performed between the Al dots as the top electrodes and the Ag coated stainless steel substrate as the bottom electrode which is shown in Figure 5.14. Figure 5.15 shows that the I-V relation for the Y-doped ZnO film is linear after 400 °C and 500 °C annealing. However, annealing temperature over 500 °C was also tested, but the I-V curve became non-linear and the current was much smaller than the sample annealed at 500 °C. This may be attributed to oxidation of the Ag film resulting in high resistivity.
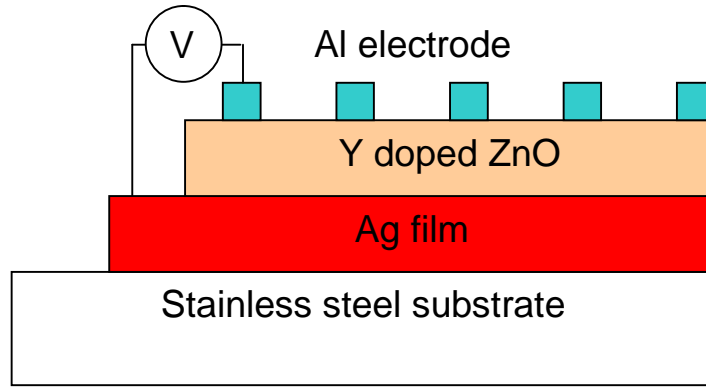
Figure 5.14 Schematic of the Al/Y-doped ZnO/Ag/stainless steel structure for current-voltage characterization.

From the slope of the I-V relation, the resistance of the Y-doped ZnO film was determined. With the thickness measured by profilometer, which is 2.2 µm, the resistivity of the ZnO film was calculated according to:

$$\rho = \frac{V \times A}{L \times I}$$

where ρ is the resistivity of the ZnO film, A is the area of the Al dot, L is the thickness of the ZnO film, V is the applied voltage, and I is the measured current. The resistivity of Y-doped ZnO after post-annealing at both 400 °C and 500 °C was estimated to vary between 6.5×10^{-4} and 6.5×10^{-3} Ω-cm, since the voltage fluctuation is quite significant in such a low voltage range.
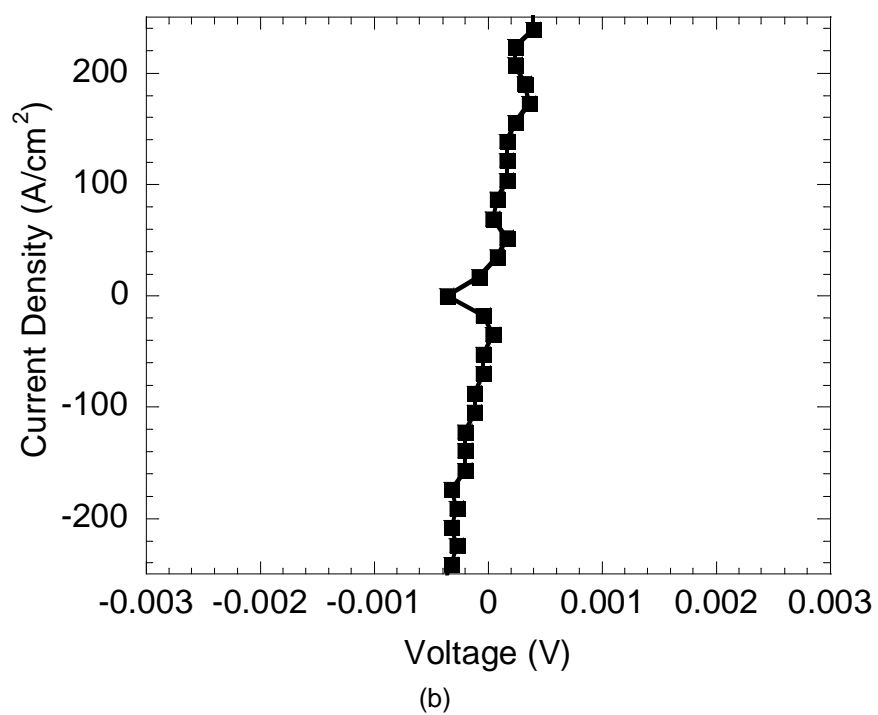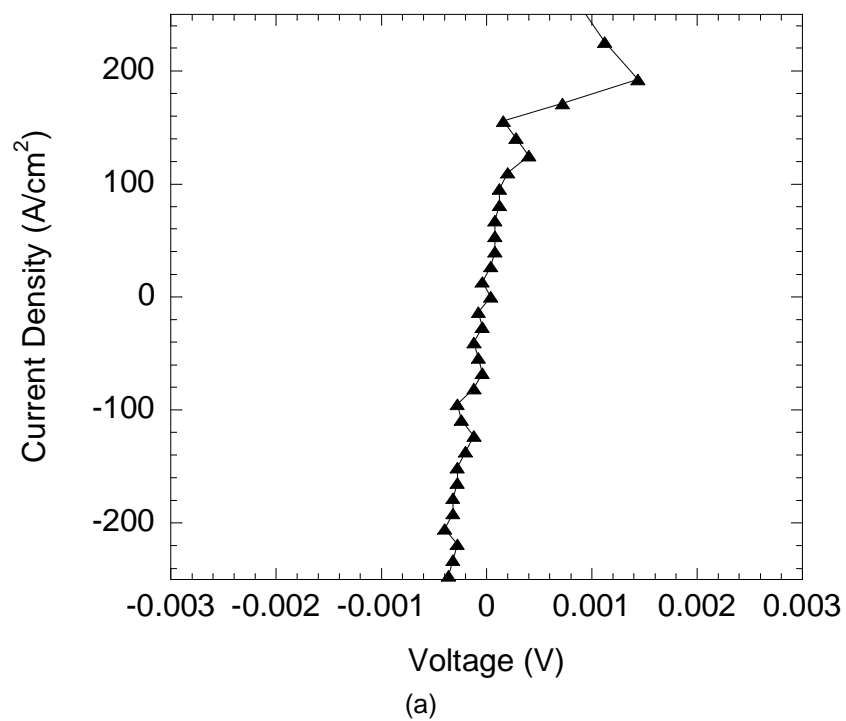
Figure 5.15 Current-voltage relation of Y-doped ZnO on Ag-coated stainless steel substrate after post-annealing at (a) 400 °C and (b) 500 °C in 1 ATM N_2 ambient for 1 hour.

5.7.3. Optical Properties

Figure 5.16 shows the total reflection of different kinds of metal. Ag, Al, Cr and Ni thin films were deposited on glass by e-beam evaporator. The thickness of the metal films was controlled at ~400 nm. The thickness of the stainless steel sheet is 0.5 mm. This stainless steel sheet was mechanical polished. From this figure, it can be seen that silver has highest reflection among these metals with average reflection around 98%. That's why silver is used as reflection material in mirror. The second high reflection metal is Al which has average reflection of 97%. The average reflection of Cr, Ni and stainless steel is low (below 70%). The stainless steel was polished by different kinds of sand paper, and the final roughness is smaller than 300 nm. From this figure, it can be seen that Al is the ideal material as the back reflector in solar cell, since Ag is an expensive material due to low world reservation. Since Al can not be electrodeposited, Ag is the alternative choice for back reflector coating on the stainless steel. Figure 5.17 shows the total reflection of stainless steel, Ag coated stainless steel and ZnO coated Ag/stainless steel. The Ag coated stainless steel was post-annealed in vacuum ambient at 300 °C for 0.5 hour. The Y doped ZnO was electrochemically deposited on Ag/stainless steel substrate. The deposition solution contains $Y^{3+}/Zn^{2+}=1$, the deposition temperature is 70 °C and the applied voltage is -0.9 V. The Ag coated stainless steel has around 97% total reflection. After ZnO deposited on the Ag coated stainless steel, the total reflectance reduces to around 80% and at 400 to 600 nm range there is sharp reflectance drop probably due to the oxidation of Ag.

After Y doped ZnO deposited on the Ag coated stainless steel, post-annealing in N_2 ambient with different temperature was carried out to examine the thermal stability of the samples. The annealing temperature was 400 and 500 °C, the N_2 pressure was 1 ATM and the annealing time was 1 hour. Total reflectance was performed by UV-vis photo spectrometer later on. Figure 5.18(a) shows the total reflectance of ZnO/Ag/Stainless steel. This sample was post-annealed at 400 °C with the average reflectance is around 60%. Figure 5.18(b) shows the total

reflectance of ZnO/Ag/Stainless steel post-annealed at 500 °C which is also around 60%. Compared to 400 °C, the average reflectance of sample annealed in 500 °C is a little lower.
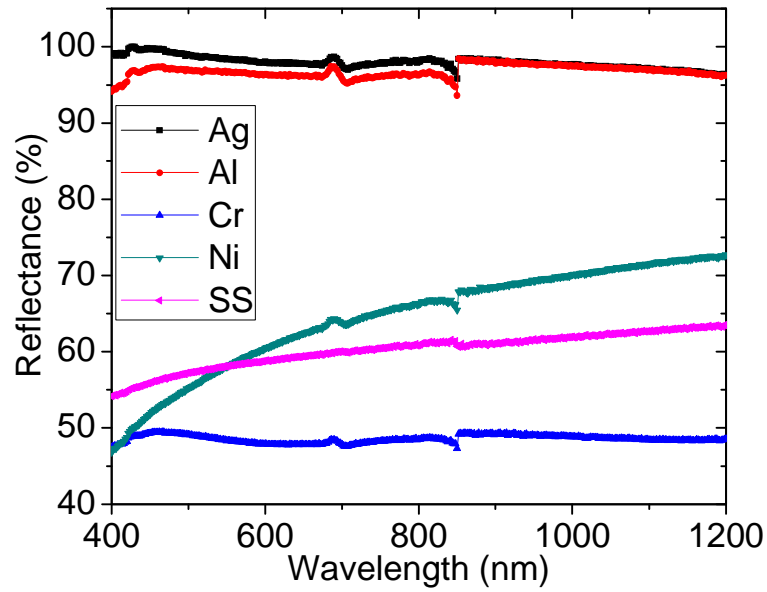
Figure 5.16 The total reflection of different metals.
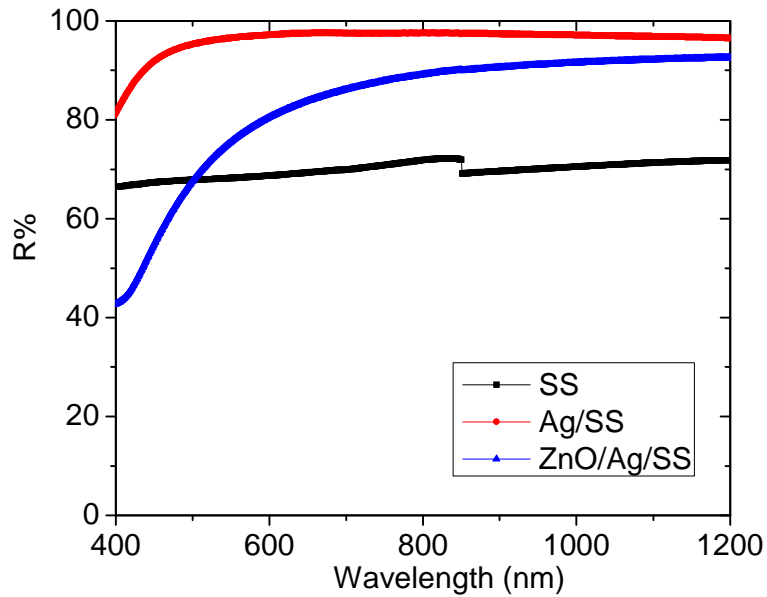
Figure 5.17 The total reflection of stainless steel, Ag coated stainless steel and ZnO coated Ag/stainless steel.

(a)

(b)
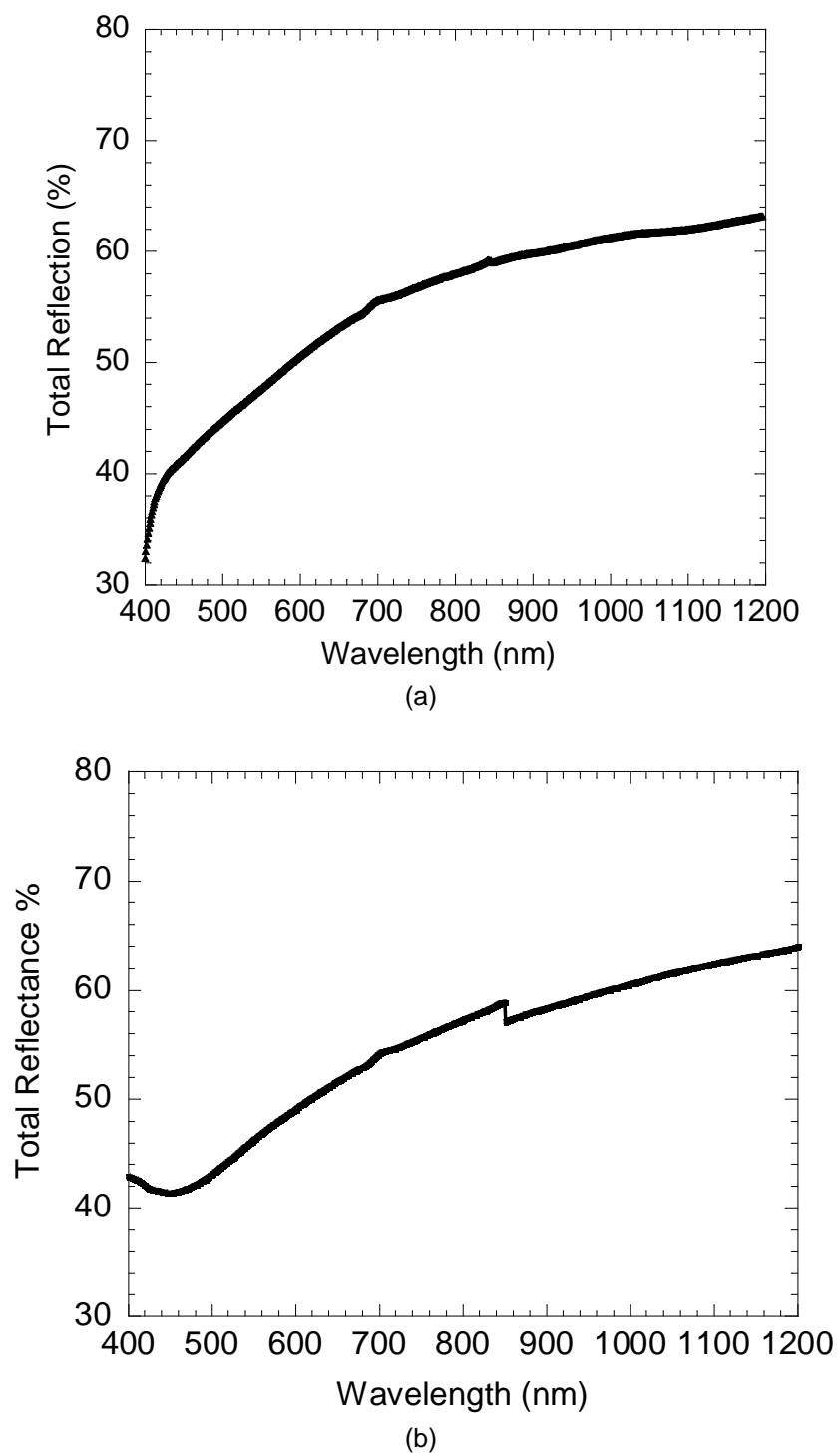
Figure 5.18 Reflectance of a Y-doped ZnO sample on Ag-coated stainless steel substrate after post-annealing in N_2 at (a) 400 °C and (b) 500 °C for 1 hour.

5.7.4. Composition
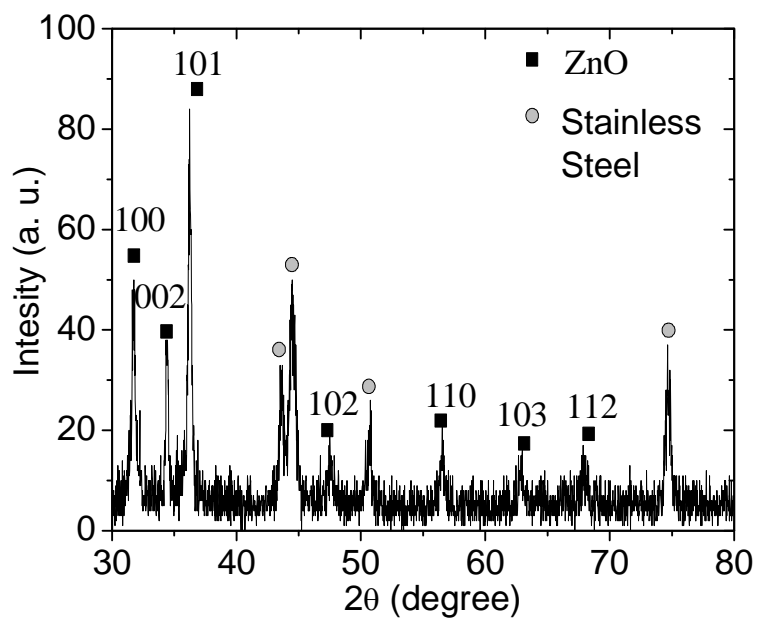
(a)
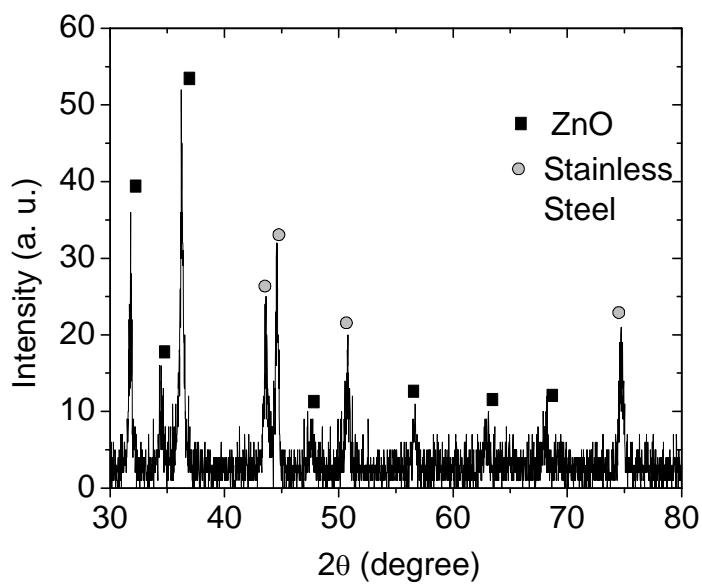
(b)

Figure 5.19 XRD profiles of Y doped ZnO on stainless steel (a) before annealing and (b) after annealing in N_2 at 500 °C for 1 hour.

Figure 5.19(a) shows the XRD curve of the as-grown Y doped ZnO on stainless steel substrate sample. The Y doped ZnO electrodeposition condition was Y^{3+}/Zn^{2+} solution ionic rate 0.1 and temperature 70 °C. From the Figure, two kinds of peaks were observed where the peaks with square mark are belonged to ZnO and the peaks marked by circle are belonged to stainless steel. Before annealing, ZnO and stainless steel peaked can be clearly identified which means ZnO didn't mix with stainless steel during the deposition process.

Figure 5.19(b) shows the XRD curve of Y doped ZnO on the stainless steel substrate after annealing. This sample was post-annealed in the N_2 ambient at 500 °C for 1 hour. The XRD profile also shows two kinds of peaks, ZnO and stainless steel. After the post-annealing, the ZnO still didn't mix with stainless steel which means this Y doped ZnO is enough stable under 500 °C thermal annealing.

5.8 Reliability

The resistivity of both home-made ITO and Y doped ZnO thin film has large degradation over time. Table 6.1 shows the sheet resistance of home-made ITO and Y doped ZnO stack structure measured after post-annealing, after 1 week and after 2 weeks exposing in air. It is clearly seen that the resistance of both ITO and Y doped ZnO stack structure increases largely after several days. The reason causing this problem is still unknown.

Table 5.1 Sheet Resistance of Home-Made ITO and Y Doped ZnO Stack Structure Over Time

	After post-annealing	After 1 week	After 2 weeks
ITO	30-50 Ω/□	80-120 Ω/□	200-300 Ω/□
Stack (ITO+ZnO)	0.8-14.3 Ω/□	28.7-72.0 Ω/□	200.2-250.73 Ω/□

5.9 Summary

Electrochemical deposition of Y-doped ZnO on ITO-coated glass substrate is demonstrated from an aqueous solution. By adjusting Y concentration in the deposition solution and post-deposition annealing conditions such as temperature, ambient, and time, the resistivity

of Y-doped ZnO is reduced to as low as 6.3×10^{-5} Ω-cm. XRD reveals no intermixing of the ZnO film with the ITO film underneath, suggesting little effect from the ITO film under ZnO. UV-vis spectroscopy indicates high transmittance of ~80 % and low absorbance of ~10 % for a 400 nm Y-doped ZnO film. EDS reveals that the Y concentration in the ZnO film with the record-low resistivity is 3.7 atomic %. The roughness of the Y doped ZnO sample was measured by AFM. By annealing in the N_2 at 500 °C, the roughness of Y doped ZnO sample was reduced.

CHAPTER 6

CONCLUSIONS AND FUTURE WORK

6.1 Conclusions

In this dissertation, solution based n-type doping in two metal oxides, Cu_2O and ZnO, was discussed. N-type doping was realized by one solution based deposition, electrochemical co-deposition of two metal compounds. Electrodeposition has the advantages of low cost, low process temperature and large scale capability and is an ideal method to fabricate TW scale solar cell. There are a lot papers reporting electrodeposition of metal oxide but few are reporting electrochemical doping in metal oxides. The electrochemical doping mechanism is discussed in this dissertation. During co-deposition, one metal oxide precipitates together with a kind of metal halogenide or a different kind of metal oxide. By controlling amount of dopant precursor in the solution, the halogen or metal behaving as dopant may go into the main metal oxide structure.

Firstly, a study on the effects of chlorine doping on electrical properties of Cl-doped Cu_2O by electrodeposition is presented. The resistivity of Cl-doped Cu_2O is affected by doping conditions, including Cu concentrations, complex agent concentrations, Cl concentrations, deposition temperatures and pH value. The lowest resistivity obtained so far is 7 Ω-cm measured by I-V relation curve, suitable for solar cell applications. Photocurrent-potential and photocurrent-time measurements verify the n-type conductivity of Cl-doped Cu_2O. SEM indicates a small grain size of ~100 nm in Cl-doped Cu_2O. XRD confirms the films as pure Cu_2O on the Cu and Au coated glass substrates. This n-type doping method enables much more efficient Cu_2O solar cells and is particularly suitable for low-cost, large-area, and high-throughput fabrication of solar cells.

Secondly, Al and Ga-doped ZnO with high transmittance and low resistance have been successfully electrodeposited on ITO substrates. Post-deposition annealing was performed in

air or in vacuum to improve the electrical properties of the Al or Ga-doped ZnO. The lowest resistivity of Al doped ZnO is 8×10^{-4} Ω-cm which is still high for using as TCO in solar cells. Besides, the non-uniform Al doped ZnO film is not suitable for large area fabrication. With vacuum annealing at 300 °C for 2 hours, a resistivity of 3.8×10^{-4} Ω-cm was obtained in Ga-doped ZnO, which meets the resistivity requirement for TCOs. The high transmittance of ~80% and low absorbance below 10% in Ga-doped ZnO of ~450 nm thick allow it to be used as a TCO in solar cells. But Ga has low annual production problem and it is not good for large scale production.

Thirdly, electrochemical deposition of Y-doped ZnO on ITO-coated glass substrate and Ag coated stainless steel substrate is demonstrated from an aqueous solution. By adjusting Y concentration in the deposition solution and post-deposition annealing conditions such as temperature, ambient, and time, the resistivity of Y-doped ZnO is reduced to as low as 6.3×10^{-5} Ω-cm. XRD reveals no intermixing of the ZnO film with the ITO film underneath, suggesting little effect from the ITO film under ZnO. UV-vis spectroscopy indicates high transmittance of ~80 % and low absorbance of ~10 % for a 400-nm Y-doped ZnO film. EDS reveals that the Y concentration in the ZnO film with the record-low resistivity is 3.7 atomic %. The average roughness of the Y doped ZnO sample was measured by AFM which is around 89.5 nm before annealing and 36.6 nm after annealing. By annealing in the N_2 at 300 °C, the roughness was reduced. But the uniformity of film is not very well and the there is a large degradation of the resistivity of Y doped ZnO.

Cu_2O is an ideal absorption material and ZnO is an ideal TCO window material for solar cell, as they are non toxic, abundant and low cost. The problem with Cu_2O and ZnO is the high resistivity of intrinsic Cu_2O and ZnO, so the electrical properties improvement of Cu_2O and ZnO by n-type doping is demonstrated here.

6.2 Future work

6.2.1 p-Type Doping in Cu_2O

Homojuction is basic structure for Cu_2O solar cell. However both p-type and n-type doping with low resistivity must be achieved in the homojuction structure. To realize p-type doping in Cu_2O, the selection of dopant is critically important. Table 6.1 shows the potential elements can behave as p-type dopant in Cu_2O. Based on the valence in Cu_2O, group V can substitute O and behave as p-type dopant. Other methods like ion implantation, thermal diffusion, sputtering etc. is used for p-type doping and achieved low resistivity of Cu_2O [69] but such kind of the vacuum deposition has high cost. However in solution deposition, N usually combines with O or C forming N-O or N-C bond which is too strong to be broken.

Table 6.1 Potential p-Type Dopants for Cu_2O

Cu_2O	
Cu site	O site
Li, Na	N, P, As

Other group V elements, like P and As, can also behave as p-type dopant in Cu_2O structure. Several metal phosphorus alloy films prepared by electrodeposition have been reported, such as CoWP [98, 99], NiPB [100] and CoFeP [101] etc. These reports revealed single phase phosphorus can be electrochemically co-deposited with metal in acidic solution. But Cu_2O is not stable in acid while it will react with hydrogen ion and dissolve in the solution. In this case, how to co-deposit P with Cu at near neutral or alkaline solution should be firstly solved. Another problem with this method is how P can be bonded with Cu to form Cu_3P, as well as Cu_3P co-precipitates together with Cu_2O. Electrodeposition of GaAs thin films from aqueous solution was reported by C. Gheorghies [102] which gives a hope to the p-type doping in Cu_2O. But how to deposit As with Cu to form Cu_3As is not known yet.

To substitute the Cu cites in Cu_2O structure, the charge valence of the elements should be zero while there is no group zero in deed. So if using group I elements which electro-negativity is less than Cu like Li, Na etc can also perform p-type dopant in Cu_2O structure.

96

Almost all the Na or Li oxides can react with water to form soluble NaOH or LiOH which makes Na or Li as p-type dopant impossible.

6.2.2 Large Area Uniform Y doped ZnO Deposition

The sample size of Y doped ZnO is 1×2 cm^2 while typical size of lab solar cell is around 1×1 inch and the size of the commercial solar cell is even larger. The sample size is limited by the film deposition method, electrodeposition which has uniformity problem in large area. If the Y doped ZnO can not cover the whole large area of the solar cell, not all the electrons will be collected as well as the efficiency will be reduced. There are several ways to improve the uniformity of the Y doped ZnO such as deposition condition, electrochemical cell design and so on.
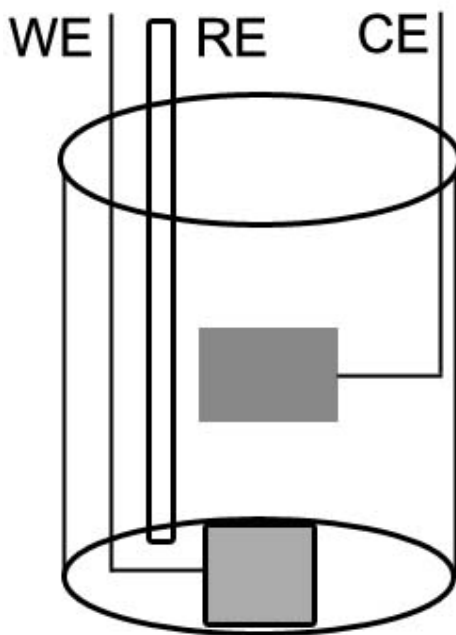
Figure 6.1 Schematic of horizontal three electrode electrochemical cell.

First, the Y doped ZnO under the certain condition discussed in chapter 6 is crystalline hexagonal particles with sub-micron size. The typical thickness for ZnO as anti-reflection coating is around 200 nm and as back-reflector is around 1 um. Low thickness with large grain

size will result in poor film coverage and non-uniform while reducing the grain size of Y doped can get more uniform film. Usually higher solution temperature can get larger grain size and ZnO can be electrodeposited with nitric acid bath at solution temperature between 40 °C to 80 °C [89, 90]. In chapter 7, the solution temperature is controlled at 70 °C in order to get a reasonable deposition rate. If reducing solution temperature, the Y doped ZnO particle size will also be reduced and possibly morphology will be amorphous. At some point, uniform Y doped ZnO film can be got with reasonable deposition rate.

Second, the three electrode electrochemical cell design is not preferred for large scale deposition because current flows from the top of the electrode to the bottom of the electrode resulting in a voltage drop on the electrode when this electrode vertically inserts into the solution. Immerse the working electrode horizontally into the deposition solution may solve this problem. Figure 6.1 shows the horizontal setting of electrodes in the electrochemical cell. Both working electrode and counter electrode are placed in parallel and the wire can be sealed by wax. This design can get better uniformity than the previous cell design. But if the substrate is too large, there is still a voltage drop between the edge and the center.

Third, the reason of degradation of the resistivity of the Y doped ZnO is complex. It is possibly due the precipitation of the Y_2O_3 or $Y(OH)_3$. Probably by second annealing it can be recovered.

REFERENCES

1. U.S. Department of Energy, Energy Information Administration, http://www.eia.doe.gov.

2. Source: IEA Energy Statistics.

3. M.I. Hoffert, K. Caldeira, A.K. Jain, E.F. Haites, L.D. Danny Harveyk, S.D. Potter, M.E. Schlesinger, S.H. Schneider, R.G. Watts, T. L. Wigley and D.J. Wuebbles, *Nature*, **395**, 881 (1998).

4. Lewis, http://nsl.caltech.edu/files/energy6.pdf.

5. M. J. Keevers and M. A. Green, *J. Appl. Phys.*, **75** (8) 1994.

6. J. Zhao, A. Wang and M. A. Green, *Prog. Photovolt: Res. Appl.*, **7,** 471 (1999).

7. A. Goetzberger, C. Heblinga and H.W. Schock, *Mater. Sci. and Eng.*, R, **40**, 1-46 (2003).

8. P. E. de Jongh, D. Vanmaekelbergh, and J. J. Kelly, *Chem. Mater.*, **11** (12), 3512 (1999).

9. R.P. Wijesundera, M. Hidaka, K. Koga, M. Sakai and W. Siripala, *Thin Solid Films*, **500** (1-2), 241-246 (2006).

10. J. Zhang, J. Liu, Q. Peng, X. Wang, and Y. Li, *Chem. Mater.*, **18** (4), 867–871 (2006).

11. G. Zhou and J. C. Yang, *Appl. Surf. Sci.*, **210** (3-4), 165-170 (2003).

12. L. Papadimitriou, N.A. Economou and D. Trivich, *Sol. Cells*, **3**, 73 (1981)

13. J. Katayama, K. Ito, M. Matsuoka and J. Tamaki, *J. Appl. Electrochem.*, **34**, 687 (2004)

14. A. Mittiga, E. Salza, F. Sarto, M. Tucci and R. Vasanthi, *Appl. Phys. Lett.*, **88**, 163502

15. H. Tanaka, T. Shimakawa, T. Miyata, H. Sato and T. Minami, *Appl. Surf. Sci.*, **244**, 568 (2005).

16. A. Mittiga, E. Salza, F. Sarto, M. Tucci, and R. Vasanthi, *Appl. Phys. Lett.*, **88**, 163502 (2006).

17. L. C. Olsen, F. W. Addis, and W. Miller, *Sol. Cells*, **7**, 247 (1982).

18. W. Siripala and J. R. P. Jayakody, *Sol. Energy Mater.*, **14**, 23 (1986).

19. L. Wang and M. Tao, *Electrochem. Solid-State Lett.*, **10**, H248 (2007).

20. K. Han and M. Tao, *Sol. Ener. Mater. Sol. Cells*, **93,** 153(2009).

21. N. Mehan, V. Gupta, K. Sreenivas, and A. Mansingh, *J. Appl. Phys.*, **96**, 3134 (2004).

22. D. Kang, H. Lim, C. Kim, I. Song, J. Park, Y. Park, and J. Chung, *Appl. Phys. Lett.*, **90**, 192101 (2007).

23. A. P. Chatterjee, P. Mitra and A. K. Mukhopadhyay, *J. Mater. Sci.*, **34**, 4225-4231 (1999)

24. J. Hu and R.G. Gordon, *J. Appl. Phys.*, **71**, 880 (1992)

25. Z. M. Jarzebski, *Phys. Status Solidi A*, **71**, 13 (1982).

26. J. Nelson, The Physics of Solar Cells, (London, 2003).

27. K.H. Kim, K.C. Park and D.Y. Ma, *J. Appl. Phys.*, **81**, 7764 (1997).

28. J.S. Kim, H.A. Marzouk, P.J. Reucroft and C.E. Hamrin Jr, *Thin Solid Films*, **217** (1-2), 133-137 (1992)

29. D. C. Look, D. C. Reynolds, C. W. Litton, R. L. Jones, D. B. Eason, and G. Cantwell, *Appl. Phys. Lett.*, **81**, 1830 (2002)

30. Y. Chen, D. M. Bagnall, Z. Zhu, T. Sekiuchi, K. Park, K. Hiraga, T. Yao, S. Koyama, M. Y. Shen and T. Goto, *J. Cryst. Growth*, **181** (1-2), 165-169(1997)

31. Z. Ben Ayadi, L. El Mir, K. Djessas, and S. Alaya, *Mater. Sci. Eng. C*, **28**, 613 (2008).

32. H. Agura, A. Suzuki, T. Matsushita, T. Aoki, and M. Okuda, *Thin Solid Films*, **445**, 263 (2003)

33. K. Ellmer, *J. Phys. D: Appl. Phys.*, **34**, 3097 (2001)

34. M. Ritala and M. Leskela, Handbook of thin film materials, (Finland, 2001).

35. M. Wu, *Appl. Phys. Lett.*, **87** (15), 153102 (2005).

36. A.J. Varkey and A.F. Fort, *Sol. Ener. Mater. Sol. Cells*, **29** (3), 253-259 (1993).

37. M. Aguilar-Frutis, M. Garcia and C. Falcony, *Appl. Phys. Lett.*, **72** (14), 1700 (1998).

38. S. Peulon and D. Lincot, *J. Electrochem. Soc.*, **145** (3), 864-874 (1998).

39. X. Han, R. Liu, Z. Xu, W. Chen and Y. Zheng, *Electrochem. Commun.*, **7** (12), 1195-1198 (2005).

40. X. Han, R. Liu, Z. Xu and W. Chen, *Thin Solid Films*, **516** (12), 4025-4029 (2008)

41. D. Tench, L.F. Warren, *J. Electrochem. Soc.*, **130**, 869 (1983).

42. S. Peulon and D. Lincot. *Adv. Mater.*, **8**, 166–170 (1996).

43. S. Peulon and D. Lincot., *J. Electrochem. Soc.*, **145**, 864–874 (1998).

44. M. Izaki and T. Omi., *J. Electrochem. Soc.*, **143**, L53 (1996).

45. M. Izaki and T. Omi., *Appl. Phys. Lett.*, **68**, 2439–2440 (1996).

46. M. Izaki and T. Omi., *J. Electrochem. Soc.*, **144**, 1949 (1997).

47. D. Lincot, B. Canava and S. Quenet, Proceedings of the 14th European Photovoltaic Solar Energy Conference, S.H. Stephens and Associates (1998).

48. H. Konno, M. Tokita, R. Furuichi, *J. Electrochem. Soc.*, **137**, 362 (1990).

49. Y. Matsumoto, J. Hombo, *J. Electroanal. Chem.*, **348**, 441 (1993).

50. T. Mercer, P.A.J. de Groot, P.N. Barlett, *J. Appl. Electrochem.*, **28**, 455 (1998).

51. X. Han, R. Liu and Z. Xu, *Thin Solid Films*, **517**, 5653–5657 (2009).

52. A.O. Musa, T. Akomolafe and M.J. Carter, *Sol. Ener. Mater. Sol. Cells,* **51**, 305-316 (1998).

53. L.C. Olsen, F.W. Addis and W. Miller, *Sol. Cells*, **7**, 247-279 (1982-1983).

54. S. N. Kale, S. B. Ogale, S. R. Shinde, M. Sahasrabuddhe, V. N. Kulkarni, R. L. Greene and T. Venkatesan, *Appl. Phys. Lett.*, **82** (13), 2010 (2003).

55. S. Ishizuka, S. Kato, T. Maruyama and K. Akimoto, *Jpn. J. Appl. Phys.*, **40**, 2765–2768 (2001).

56. H. Kim, A. Pique, J.S. Horwitz, H. Murata, Z.H. Kafafi, C.M. Gilmore and D.B. Chrisey, *Thin Solid Films*,**377-378**,798-802 (2000).

57. K.H. Kim, K.C. Park and D.Y. Ma, *J. Appl. Phys.*, **81** (12), 7764 (1997).

58. M. J. Alam and D. C. Cameron, *J. Vac. Sci. Technol. A*, **19** (4), 1642 (2001)

59. K. Ellmer, *J. Phys. D: Appl. Phys.*, **34**, 3097 (2001)

60. C. Bundesmann, N. Ashkenov, M. Schubert, D. Spemann, T. Butz, E. M. Kaidashev, M. Lorenz and M. Grundmann, *Appl. Phys. Lett.*, **83**, 1974 (2003)

61. S. Major, A. Banerjee and K.L. Chopra, Thin Solid Films, **108** (3), 333-340 (1983).

62. J. Hu and R.G. Gordon, Sol. Cells, **30**, 437 (1991).

63. E. Chikoidze, M. Nolan, M. Modreanu, V. Sallet and P. Galtier, *Thin Solid Films*, **516**, 8146–8149, (2008)

64. C.H. Park, S.B. Zhang and S.H. Wei, *Phys. Rev. B*, **66**, 073202 (2002)

65. A. E. Rakhshani, *Solid-State Electron.*, **29**, 7 (2006).

66. D. Trivich, E. Y. Wang, R. J. Komp, and F. Ho, in Conference Records of 12th IEEE Photovoltaic Specialists Conference, IEEE, New York, 1976, p. 875.

67. P.E. de Jongh, D. Vanmaekelbergh and J.J. Kelly, *Chem. Mater.*, **11**, 3512-3517 (1999)

68. K. Akimoto, S. Ishizuka, M. Yanagita, Y. Nawa, G.. K. Paul, and T. Sakurai, *Sol. Energy*, **80**, 715 (2006).

69. S. Ishizuka, S. Kato, T. Maruyama and K. Akimoto, *Jpn. J. Appl. Phys.*, **40**, 2765 (2001).

70. P. E. de Jongh, D. Vanmaekelbergh, and J. J. Kelly, *J. Electrochem. Soc.*, **147**, 486 (2000).

71. D. R. Lide, in Handbook of Chemistry and Physics 84th Ed. (CRC Press, Boca Raton, 2004).

72. A. E. Rakhshani and J. Varghese, *J. Mater. Sci.*, **23**, 3847 (1988).

73. M.A. Contreras, B. Egaas, K. Ramanathan, J. Hiltner, A. Swartzlander, F. Hasoon and R. Noufi, *Prog. Photovoltaics: Res. Appl.*, **7**, 4, 311 – 316 (1999).

74. A. Gupta and A.D. Compaan, *Appl. Phys. Lett.,* **85**, 684 (2004).

75. K. Nomura, H. Ohta, A. Takagi, T. Kamiya, M. Hirano and H. Hosono, *Nature*, **432**, 488-492 (2004).

76. L.R. Pederson, P. Singh and X.-D. Zhou, *Vac.*, **80**, 10, 1066-1083 (2006).

77. K. L. Chopra, P. D. Paulson and V. Dutta, *Prog. Photovoltaics: Res. Appl.*, **12**, 2-3, 69 – 92, (2004).

78. T. Pauport and D. Lincot, *Electrochimica Acta*, **45**, 20, 3345-3353 (2000).

79. J. Li, R. Kykyneshi, J. Tate and A.W. Sleight, *Solid State Sci.*, **9**, 7, 613-618 (2007).

80. J.S. Wellings, A.P. Samantilleke, P. Warren, S.N. Heavens and I.M. Dharmadasa, *Semicond. Sci. Technol.*, **23**, 125003 (2008).

81. E. Fortunato, D. Ginley, H. Hosono, and D.C. Paine, MRS Bull., 32, 242 (2007).

82. M. Berginski, J. Hüpkes, M. Schulte, G. Schöpe, H. Stiebig, B. Rech, and M. Wuttig, *J. Appl. Phys.*, **101**, 74903 (2007).

83. T. Minami, *Thin Solid Films*, **516**, 5822 (2008).

84. H. Kim, J.S. Horwitz, W.H. Kim, A.J. Makinen, Z.H. Kafafi, and D.B. Chrisey, *Thin Solid Films*, **539**, 420-421 (2002).

85. G. Gu, P.E. Burrows, S. Venkatesh, S.R. Forrest, and M.E. Thompson, *Opt. Lett.*, **22**, 172 (1997).

86. U.S. Geological Survey, in Mineral Commodity Summaries 2008, United States Government Printing Office, Washington (2008).

87. R.G. Gordon, *MRS Bull.*, **25**, 52 (2000).

88. H.J. Ko, Y.F. Chen, S.K. Hong, H. Wenisch, T. Yao, and D.C. Look, *Appl. Phys. Lett.*, **77**, 3761 (2000).

89. S. Otani, J. Katayama, H. Umemoto and M. Matsuoka, *J. Electrochem. Soc.*,**153** (8), C551-C556 (2006).

90. Z. Ben Ayadi, L. El Mir, K. Djessas, and S. Alaya, *Mater. Sci. Eng. C,* **28**, 613 (2008).

91. H. Agura, A. Suzuki, T. Matsushita, T. Aoki, and M. Okuda, *Thin Solid Films*, **445**, 263 (2003).

92. D. Raviendra and J.K. Sharma, *J. Appl. Phys.*, **58**, 838 (1985).

93. M.J. Alam and D.C. Cameron, *J. Vac. Sci. Techn. A*, **19**, 1642 (2001).

94. S.-M. Park; T. Ikegami, and K. Ebihara, *Thin Solid Films*, **513**, 90 (2006).

95. S.S. Shinde, P.S. Shinde, C.H. Bhosale, and K.Y. Rajpure, *J. Phys. D: Appl. Phys.*, **41**, 105109 (2008).

96. X. Han, K. Han, and M. Tao, *ECS Trans.*, **5** (15), 93-102 (2009).

97. S. Zhang and R. Xiao, *J. Appl. Phys.*, **83**, 3842 (1998).

98. S.M.S.I. Dulal, C.B. Shin, J.Y. Sung and C.K. Kim, *Electrochimica. Acta*, **53**, 934–943 (2007).

99. S.M.S.I. Dulal, C.B. Shin, J.Y. Sung and C.K. Kim, *J. Appl. Electrochem.*, **38**,83–91 (2008)

100. D.J. Kim, M.J. Kim, J.S. Kim, H.P. Kim, *Surf. Coatings Tech.*, **202**, 2519–2526 (2008).

101. E.E. Kalu, *J. Solid State Electrochem.*, **11**, 1145–1156 (2007).

102. C. Gheorghies, L. Gheorghies and G. Fetecau, *J. Optoelectron. Adv. Mater.*, **9** (9), 2795-2798 (2007).

103. M. Pourbaix, in Atlas of Electrochemical Equilibria in Aqueous Solutions (Pergamon, New York, 1966), p. 386.

104. A. V. Shah,y, H. Schade,M. Vanecek, J. Meier, E. Vallat-Sauvain, N.Wyrsch, U. Kroll, C. Droz and J. Bailat, *Prog. Photovolt: Res. Appl.*, **12**, 113–142 (2004)

BIOGRAPHICAL INFORMATION

Mr. Xiaofei Han was born in 1981. He earned a Bachelor of Science degree majored in Chemistry from Zhejiang University, Hangzhou, P. R. China in 2004 and later a Master of Science degree in same major from Zhejiang University, Hangzhou, P. R. China in 2006. He registered as a graduate student in Materials Science and Engineering at the University of Texas at Arlington in 2007 and earned a Doctor of Philosophy degree in Materials science and Engineering at the University of Texas at Arlington in May 2011.